CHEMICAL REVIEWS

Review

Cite This: *Chem. Rev.* 2018, 118, 2718−2768

pubs.acs.org/CR

Iron and Copper Active Sites in Zeolites and Their Correlation to Metalloenzymes

Benjamin E. R. Snyder,[†] Max L. Bols,[‡] Robert A. Schoonheydt,*[,‡] Bert F. Sels,*[,‡] and Edward I. Solomon*[,†,§]

[†]Department of Chemistry, Stanford University, Stanford, California 94305, United States

[‡]Department of Microbial and Molecular Systems, Centre for Surface Chemistry and Catalysis, KU Leuven—University of Leuven, Celestijnenlaan 200F, B-3001 Leuven, Belgium

[§]Photon Science, SLAC National Accelerator Laboratory, 2575 Sand Hill Road, Menlo Park, California 94025, United States

ABSTRACT: Metal-exchanged zeolites are a class of heterogeneous catalysts that perform important functions ranging from selective hydrocarbon oxidation to remediation of NO_x pollutants. Among these, copper and iron zeolites are remarkably reactive, hydroxylating methane and benzene selectively at low temperature to form methanol and phenol, respectively. In these systems, reactivity occurs at well-defined molecular transition metal active sites, and in this review we discuss recent advances in the spectroscopic characterization of these active sites and their reactive intermediates. Site-selective spectroscopy continues to play a key role, making it possible to focus on active sites that exist within a distribution of inactive spectator metal centers. The definition of the geometric and electronic structures of metallozeolites has advanced to the level of bioinorganic chemistry, enabling direct comparison of metallozeolite active sites to functionally analogous Fe and Cu sites in biology. We identify significant parallels and differences in the strategies used by each to achieve high reactivity, highlighting potentially interesting mechanisms to tune the performance of synthetic catalysts.

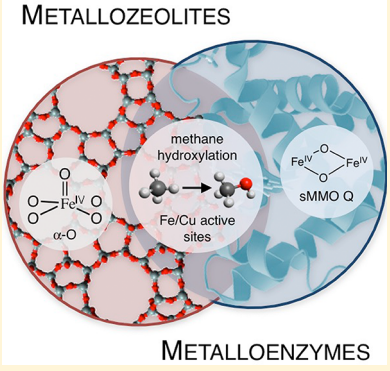

CONTENTS

Special Issue: Oxygen Reduction and Activation in Catalysis

Received: June 14, 2017
Published: December 19, 2017

DOI: 10.1021/acs.chemrev.7b00344
Chem. Rev. 2018, 118, 2718−2768

1. INTRODUCTION

Based on promising applications in the remediation of noxious NO_x and N_2O from combustion engines and the mild partial oxidation of unreactive hydrocarbons, research into redox catalysis for selective partial oxidation using copper and iron exchanged zeolites has moved forward at an appreciable pace. The general challenge associated with the latter application is the formation of highly reactive oxygen species, combined with the selectivity toward partial oxidation products over thermodynamically favored full oxidation into CO_2 and H_2O. In addition, the catalysts should preferably contain earth-abundant transition metals (Fe, Cu, Co, Ni, ...) and make use of oxidants (e.g., O_2, N_2O, NO, ...) which are cheap and benign, or which can be recovered from waste streams. The activation of the strong (104 kcal/mol) methane C−H bond under mild conditions can be seen as a model reaction requiring such reactive oxygen species. The performance in the partial oxidation of methane under mild conditions will function as a benchmark for defining the zeolitic Cu/O and Fe/O species as active sites in this review. Another industrially relevant conversion, the partial oxidation of benzene to phenol, faces similar challenges and will also be treated.

Over the past years, previously reported active sites in Cu and Fe exchanged zeolites have been characterized in detail and, simultaneously, new observations have opened up novel tracks of research. Combinations of spectroscopic techniques and the use of site-selective spectroscopy complementing bulk techniques and reactivity studies as well as computational models have had a significant hand in this progress. Focus is put on the formation, stability, and characterization of Cu/O and Fe/O reactive species in zeolites and on the relation between their structural properties and their exceptional reactivity for inert hydrocarbon oxidation. In section 2, a general introduction on zeolites is given and transition metal ions (TMI) in zeolites are discussed.

Parallels can be drawn between these zeolitic systems and metalloenzymes which catalyze similar reactions, both on the level of catalytic function and on the level of characterization. Characterization techniques which will be discussed in this review (section 3), including resonance Raman spectroscopy, variable-temperature variable-field magnetic circular dichroism, and nuclear resonance vibrational spectroscopy, have recently crossed over from the bioinorganic world to the field of heterogeneous catalysis. In sections 4 and 5, these techniques are applied to reactive copper and iron active sites for methane activation. Spectroscopic data are coupled to electronic structure calculations, showing how the unique geometric and electronic structures of metallozeolite active sites lead to high reactivity. Finally, a comparative study of oxidation chemistry by metalloenzymes and metallozeolites is presented in section 6. Structure−function relationships are well-established for iron and copper active sites in biology, and here we extend concepts from bioinorganic chemistry to metallozeolite catalysis.

1.1. Challenges of Industrial Selective Partial Oxidation

The partial oxidation of inert hydrocarbons, such as methane and benzene, presents inherent challenges for catalysis. High selectivity toward partially oxygenated products of inert hydrocarbons is hampered by their decreased C−H bond strengths. This causes a preference for the formation of overoxidized products through consecutive oxygenation reactions, and imposes an upper limit to the achievable selectivity. Due to the high activation barriers common for these reactions, attaining high yields tends to require an extended contact time with the oxidation catalyst. This leads to a trade-off between conversion, requiring long contact times, and selectivity, requiring short contact times. Workarounds to this issue involve the synthesis of stable, partially oxidized intermediates, which are converted to the desired products in subsequent steps. These intermediates include syngas and strongly adsorbed (coordinated) reactive species on the heterogeneous (homogeneous) catalyst surface (active site).

1.1.1. Conversion of Methane to Methanol. To valorize methane for chemical synthesis, the notoriously inert CH_4 molecule must first be functionalized. The difficulty of methane functionalization stems from the molecule's electronic structure, shown in Figure 1. Due to the high strength of the methane C−H bond, the occupied bonding levels ($1a_1$, $1t_2$) are significantly stabilized (Figure 1A). This is evident from the high ionization potential of methane (12.61 eV).[1] The high symmetry of methane also results in bonding molecular orbitals that are delocalized over many atoms ($1a_1$ and $1t_2$ in Figure 1B). These are resistant to electrophilic attack due to poor energy match and overlap with molecular orbitals of incoming electrophiles. The unoccupied antibonding levels ($2a_1$, $2t_2$ in Figure 1) are significantly destabilized and delocalized, and this makes methane similarly resistant to nucleophilic attack. Finally, methane is resistant to deprotonation ($pK_a = 48$) due to the high covalency of its C−H bonds.[2]

Several strategies have been developed to tackle the problem of selective methane activation under mild conditions, and these can be divided into four classes shown in Figure 2.[3] In oxidative addition (Figure 2i), a low-valent metal reductively cleaves the C−H bond by donating two electrons into the C−H σ* antibonding orbital. In electrophilic activation (e.g., Shilov chemistry, Figure 2ii), a C−H bonding orbital donates into a vacant metal d orbital, and this weakens and polarizes the C−H bond so that methane can be deprotonated. In σ bond metathesis (Figure 2iii), binding to the M−X fragment plays a similar role in activating the C−H bond. Finally, reactive metal−oxygen species (Figure 2iv) are highly electrophilic, with

DOI: 10.1021/acs.chemrev.7b00344
Chem. Rev. 2018, 118, 2718−2768

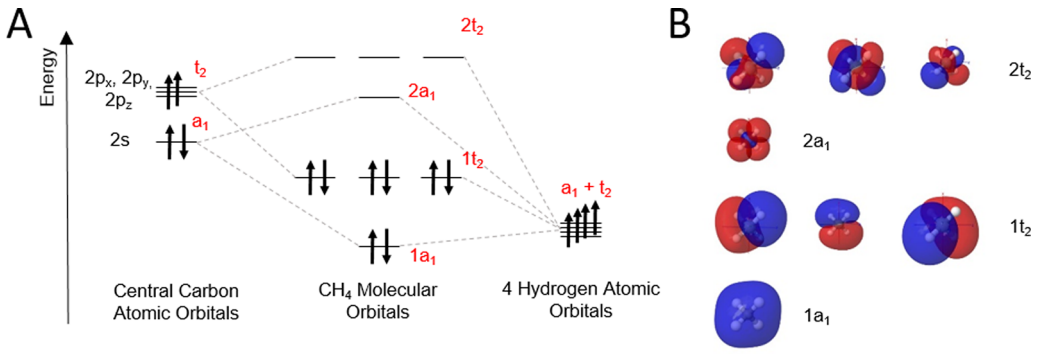

Figure 1. (A) Molecular orbital diagram for methane derived from symmetry adapted linear combinations of carbon and hydrogen valence atomic orbitals. (B) Molecular orbitals of methane, showing bonding ($1a_1$, $1t_2$) and antibonding levels ($2a_1$, $2t_2$).

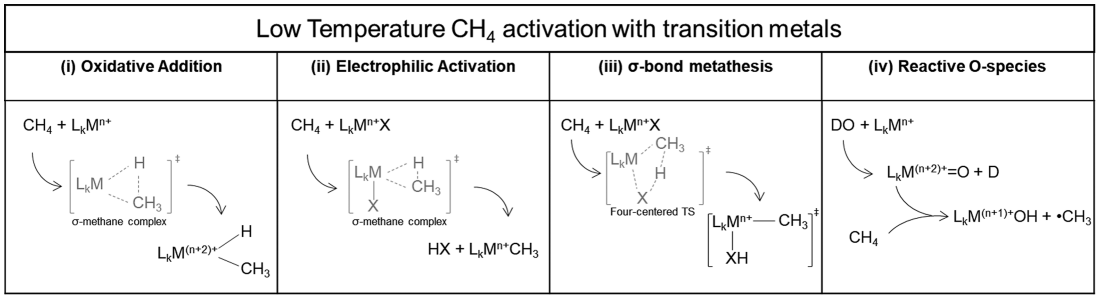

Figure 2. Four main mechanisms for C−H bond activation in methane: (i) oxidative addition, (ii) electrophilic activation, (iii) σ-bond metathesis, and (iv) oxidation with a reactive oxygen species.

low-lying unoccupied molecular orbitals that are localized on a metal−oxygen fragment. These are activated as acceptor orbitals for H-atom abstraction (HAA), even from the stable C−H bonding levels of methane shown in Figure 1. This is the strategy employed by nature and metallozeolites to activate strong aliphatic C−H bonds. (Activation of aromatic C−H bonds proceeds through a different mechanism, discussed below.)

Specific catalytic systems have been developed to selectively oxygenate methane while avoiding excessive oxidation to thermodynamically favored products (e.g., formate, CO_2). Shilov systems operate through the electrophilic activation of the C−H bond by a Pt^{II} complex.[4,5] Stronger C−H bonds have higher electron density than weaker C−H bonds, and are therefore more susceptible to electrophilic activation, suppressing overoxidation. Oxidation with soft electrophiles, such as sulfur, is also proposed.[6] All have their limitations, however, for which we refer the reader to specific literature on the topic.[4,7−9] The use of a reactive oxygen center for the C−H bond activation shifts the challenge from the C−H cleavage to the formation of isolated, highly reactive oxygen species. This requires the activation of an oxidant—ideally O_2. Binding dioxygen to a reduced metal center results in activation at the oxy, superoxy, or peroxy level. With the participation of more than one reduced metal, the O−O bond can be cleaved resulting in activated metal−oxo species. The reaction of triplet O_2 (oxy) species with singlet organic substrates is spin-forbidden and therefore slow. Superoxy, peroxy, and oxo species do not suffer from this limitation, however; thus reductive activation of O_2 can overcome the spin-forbiddenness of its reaction with organic substrates. Reactive metal−oxygen species can also be generated in zeolites using nitrous oxide or hydrogen peroxide. This is particularly important in the chemistry of Fe-zeolites, where methane-reactive sites cannot be formed with O_2. (Although we note copper zeolites are activated equivalently by both N_2O and O_2.) For N_2O, there is an entropic driving force associated with irreversible N_2 release during O-atom transfer, and this can be used to drive the generation of unstable (and therefore reactive) metal−oxo sites. However, the use of N_2O as the final oxidant for methane activation inevitably implies a bottleneck for future upscaling to an industrially relevant scale. Industrially available side streams of N_2O are currently dwarfed by the intended scale of methane upgrading.[10] Alternatively, other oxidants can be used (O_3, *tert*-butyl hydroperoxide, HNO_3, H_2SO_4, NaClO, $NaClO_2$, H_2O_2, ...), but these cannot compete with freely available atmospheric O_2. A strongly related challenge in catalysis is therefore the activation of molecular oxygen, either to form intermediary oxidants, or to directly perform the desired oxidation reaction in the next step.

One candidate platform chemical obtained from methane is methanol. Methanol is subsequently converted to a broad range of petrochemical products such as formaldehyde, dimethyl ether, and propylene, among others. Moreover, methanol is an easily transported liquid at room temperature. Methane transport, on the other hand, requires extensive infrastructure (liquefied natural gas (LNG) terminals, LNG carriers, and natural gas pipeline systems) with a high risk of leakages contributing to the greenhouse effect.[11] Currently implemented methane to methanol processes all pass over syngas as an intermediate, requiring large scale plants which operate at high pressures and temperatures (ICI process—Figure 3, top).[12] For syngas production, three well-established, heterogeneously catalyzed processes exist: (1) steam reforming over nickel catalysts, (2) autothermal reforming over nickel supported on magnesium aluminum spinel, and (3) dry reforming over nickel or noble metal catalysts (pilot stage).[12] The syngas is then converted to methanol using copper and zinc oxides on alumina as the

DOI: 10.1021/acs.chemrev.7b00344
Chem. Rev. 2018, 118, 2718−2768

INDIRECT SYNGAS PATHWAY

1) Steam Reforming:

$CH_4(g) + H_2O(g) \rightarrow CO(g) + 3H_2(g)$ $\Delta H°_r = 206$ kJ/mol

2) Methanol Formation:

$CO + 2H_2 \rightarrow CH_3OH$ $\Delta H°_r = -90.7$ kJ/mol

DIRECT PARTIAL OXIDATION PATHWAY

$CH_4(g) + ½\ O_2(g) \rightarrow CH_3OH\ (g)$ $\Delta H°_r = -126.43$ kJ/mol, $\Delta S°_r = -49.3$ J/mol/K

Figure 3. Thermodynamics of methane-to-methanol conversion using the syngas route (top) and direct partial oxidation (bottom).

catalyst. Although very efficient, and operating at high yields with high selectivity, the current technology is unsuitable for valorizing small scale methane sources. Given that an estimated 30−60% of sources are designated as "stranded natural gas" under current economic conditions,[13,14] this is an important issue. Technology to address the valorization of oil-associated gas, biogas, and natural gas from remote wells is therefore highly desirable from economic and environmental points of view. Ideally, the oxidation of methane to methanol would be achieved in a single step at mild conditions, using oxygen as the ultimate electron acceptor (Figure 3, bottom). With all products and reagents in the gas phase, the net conversion is exothermic, with $\Delta H°_r = -30.22$ kcal/mol and $\Delta S°_r = -11.8$ cal/mol K. Due to the negative reaction entropy, this process is favored at low temperatures (and feasible below 2500 K). This is in contrast to the steam reforming of methane syngas (Figure 3, top), which is only thermodynamically possible above 1000 K.

1.1.2. Conversion of Benzene to Phenol. Phenol is an important precursor molecule for chemical synthesis due to its high reactivity toward electrophilic aromatic substitution. Downstream uses of phenol include production of bisphenol A, ketone−alcohol oil (KA oil) for nylon-66, and various polymers and pharmaceuticals. About 90% of phenol is currently produced from benzene using the cumene process.[15] First, benzene undergoes a Friedel−Crafts alkylation with propylene (sometimes catalyzed using acidic zeolites). The resulting cumene is oxidized with molecular oxygen to form cumene hydroperoxide, which subsequently decomposes to a 1:1 mixture of acetone and phenol.[16] Cumene hydroperoxide functions as a stable, partially oxidized intermediate, preventing overoxidation. Drawbacks of the cumene process include the simultaneous production of acetone, which must be separated and for which a market must be found, as well as safety and environmental concerns regarding the intermediates (e.g., hydroperoxide) and solvents. As with the methane-to-methanol conversion, many of these issues can be addressed using a direct partial oxidation route, in which benzene is hydroxylated directly to form phenol.

The challenges associated with direct partial oxidation of benzene parallel those associated with the methane-to-methanol conversion. Like methane, benzene has an electronic structure that is chemically inert. The frontier molecular orbitals of benzene are shown in Figure 4. The highest occupied molecular orbitals (e_g) are π bonding levels formed from linear combinations of the out-of-plane carbon 2p orbitals. These orbitals are highly stable and delocalized due to aromatic π bonding in the benzene ring. They are therefore resistant to electrophilic attack. The unoccupied antibonding orbitals (e_u in Figure 4) are significantly destabilized and also delocalized, and this

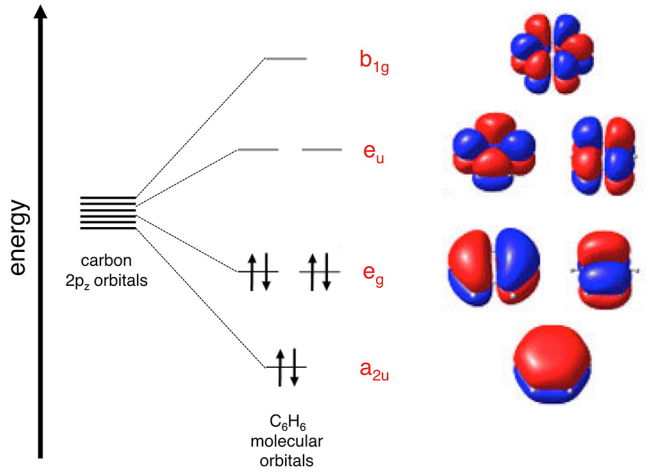

Figure 4. π frontier molecular orbitals of benzene derived from out-of-plane carbon 2p orbitals.

makes benzene resistant to nucleophilic attack. The C−H bonds of benzene are even stronger than methane C−H bonds (113 kcal/mol versus 104 kcal/mol for CH_4), and as a result they are not susceptible to direct electrophilic attack through H-atom abstraction. (On the other hand, the C−H bonds of benzene are more susceptible to oxidative addition at low-valent metals than the C−H bonds of methane due to the participation of aromatic π orbitals in bonding to the metal.[17]) As with methane, metalloenzymes and metallozeolites overcome the chemical inertness of benzene using electrophilic reactive oxygen species.[18,19] (Oxidative addition of aromatic C−H bond is most facile at low-valent second- and third-row transition metals; however, these are scarce in biology and difficult to stabilize using protein-derived ligands). A key difference here is that these intermediates attack the π bonding electrons of benzene (e_g in Figure 4) through an electrophilic aromatic substitution mechanism, and they do not interact directly with the C−H bonds (in contrast to H-atom abstraction from methane). A common mechanistic proposal for benzene hydroxylation by electrophilic metal−oxo species, not yet evaluated in the context of metallozeolite catalysis, involves initial formation of a so-called σ-complex. This intermediate is characterized by a single bond between the active oxygen and ipso carbon of the aromatic ring, which becomes sp^3 hybridized. The formation of the new C−O bond is coupled to the one- or two-electron oxidation of the aromatic ring resulting in radical or cationic σ-complexes, respectively. Decay of the σ-complex to phenol may proceed through an inter- or intramolecular mechanism. Notable among these is the "NIH" shift,[20] first defined for biological aromatic oxidations, in which the ipso proton of the σ-complex is transferred to the ortho carbon, forming 1,4-cyclohexadienone that subsequently tautomerizes to phenol.

1.2. Enzymes as Industrial Oxidation Catalysts

In biology, enzymes exist that carry out selective hydrocarbon oxidation rapidly under ambient conditions. Methanotrophs have evolved iron and copper methane monooxygenases (particulate methane monooxygenase, Cu; soluble methane monooxygenase, Fe) to catalyze the hydroxylation of methane to methanol using atmospheric O_2.[21] In all organisms, a range of iron and copper enzymes exist that perform aromatic hydroxylation with atmospheric O_2, including cytochrome P450, phenylalanine hydroxylase, and tyrosinase.[18,19] Comparison of

DOI: 10.1021/acs.chemrev.7b00344
Chem. Rev. 2018, 118, 2718−2768

current industrial oxidation catalysts to these enzymes demonstrates the considerable shortcomings of commercial synthetic systems. In terms of the catalytic activity per active site, measured by single site turnover frequencies, enzymatic systems are dramatically more efficient than catalysts used in today's industrial reactors. Typical turnover frequencies for enzymes range between 10^3 and 10^7 s^{-1} versus 10^{-2}–10^2 s^{-1} for synthetic catalysts.[22] Moreover, enzymes showcase impressive product and reagent selectivity, often near 100%, carefully tailored by evolution to exactly meet their host organism's needs. On the reagent side, this implies a reliance on readily available chemicals already present as, or synthesized from, ambient chemical compounds. On the product side, this implies largely innocuous side products, if any. Bioreactors, using whole enzymes as catalysts, exploit these advantages, enabling certain processes, mainly relevant to the food industry, but also in the polymer industry, waste treatment industry, biomass conversion, and others, to run at mild conditions and attain high selectivity.

On the downside, enzymes suffer from a limited stability range with respect to numerous environmental parameters that are important in industrial oxidation chemistry. Having evolved to specifically support life at typically ambient conditions, enzymes lack the temperature, pressure, and solvent tolerance required in most industrial processes. Especially environmental and energy related oxidation catalysis is often performed at elevated temperature and/or pressure and/or in the presence of highly concentrated contaminants not usually encountered in nature. This places prohibitive constraints on the use of enzymes in such applications. Additionally, precursors and products are generally not the same for industrial synthesis and biosynthesis, requesting some modifications of enzymatic processes at the catalyst level. Moreover, biocatalysts operate within the complex synergy provided by the host cell, often requiring specific cofactors such as ATP/ADP and $NAD(P)^+$/NAD(P)H. It is unfeasible to introduce such complexity in a reliable, large scale industrial reactor. Product separation from the multicomponent aqueous mixture in the bioreactor presents another complication. A review of alkane biohydroxylation covering the current status and prospects was published by Soussan et al. in 2016.[23]

To overcome these challenges, while retaining the benefits of high activity and selectivity, a biomimetic approach has been followed in the past decades leading to interesting results with homogeneous complexes,[24] synthetic enzymes,[25] metal–organic frameworks,[26,27] and encapsulated complexes in inorganic matrices,[28–31] mimicking the ligand environment provided by the functional residues in the active pockets of enzymes. These systems, along with the study of enzymes themselves, have provided essential insight into the inner workings of enzymes, and in the methodology of the field. They still, however, lack the stability and simplicity required for supporting commercially viable, large scale applications in industry.

1.3. TMI Zeolites as Industrial Oxidation Catalysts

Zeolites offer many of the advantages associated with enzyme catalysis, including reactivity at well-defined transition metal active sites that can cycle through a range of oxidation states. Unlike enzymes, however, these inorganic materials are highly robust and can accommodate harsh reaction conditions. Zeolites have established a strong track record as industrial catalysts with initial applications as large scale acid catalysts for the petrochemical industry in the 1960s. Incorporating extraframework transition metal ions into their inner pore structure (section 2) introduces these materials as highly stable oxidation catalysts, with properties reminiscent of those displayed by transition metal containing metalloenzymes (section 6). With this in mind, enzyme-inspired TMI-zeolite catalysts are promising materials to support the next generation of industrial oxidation processes. Here, we move from an enzyme mimicking approach toward one driven by concepts that have evolved from metalloenzyme chemistry.

The first TMI zeolite active in the selective oxidation of methane to methanol was discovered by Panov et al. in 1990.[32] They discovered the formation of an active Fe/O species on the ZSM-5 zeolite upon oxidation with N_2O. The reactive intermediate, named α-O, has a remarkable activity toward the activation of methane. A bound intermediate is formed which can be extracted with water to yield methanol. Follow-up studies by the same group revealed the reactivity of α-O toward other hydrocarbons, including benzene.[33] In contrast to methanol, no steam is required to release the phenol product, which desorbs spontaneously from the catalyst at 673 K. The methane to methanol conversion over α-O continues to be burdened by practical limitations; the conversion is stoichiometric, requiring an additional steaming step for product desorption, and the requirement of N_2O as oxidant limits the catalysts' applicability. Meanwhile, the catalytic conversion of benzene to phenol has been translated into a pilot scale reactor by Solutia (now Ascend) in the AlphOx process;[34] however, the project was discontinued due to excessive deactivation of the catalyst by coking and a mismatch in recyclable N_2O versus required amounts. Despite this, the practical potential of the catalyst is demonstrated by the AlphOx process, and new developments in research on the Fe-zeolites may well provide answers to the catalysts' current limitations including limited turnover numbers and low tolerance for trace impurities. Recently, for example, the geometric and electronic structure of α-O was defined by Snyder et al.[35] (see section 5): an essential step in enabling further application-directed engineering of the material.

Copper-containing zeolites show similar reactivity toward methane and benzene.[36] While they are less reactive compared to the Fe-zeolites, Cu-zeolites have the distinct advantage of using O_2 as oxidant. The reactive intermediate in selective hydrocarbon oxidation over O_2-activated Cu-zeolites was first identified in 2005 by Groothaert et al.,[36] and its geometric and electronic structure was elucidated by Woertink et al. in 2009.[37] As with the Fe-zeolites, issues related to product trapping and catalyst deactivation have presented barriers to commercialization. Emerging insight into Cu active sites in zeolites, discussed in section 4, will play an important role in resolving these issues.

For both iron and copper zeolites, parallels have been drawn to metalloenzyme chemistry with respect to function, but also with respect to active site geometric and electronic structure. Reliable experimental data on metallozeolite active sites that would enable this type of comparison are limited, however. Perhaps the most significant barrier with respect to experimental characterization of these materials is the presence of inactive spectator metals, which in some cases make up the majority of the extra-framework metal content in TMI zeolites. As a result, data from bulk techniques such as X-ray absorption spectroscopy and magnetic susceptibility are not reliable. Despite this, bulk data have been interpreted extensively in the literature, resulting in a range of contradictory assignments for active sites in zeolites. In this review, we focus on recent

DOI: 10.1021/acs.chemrev.7b00344
Chem. Rev. 2018, 118, 2718–2768

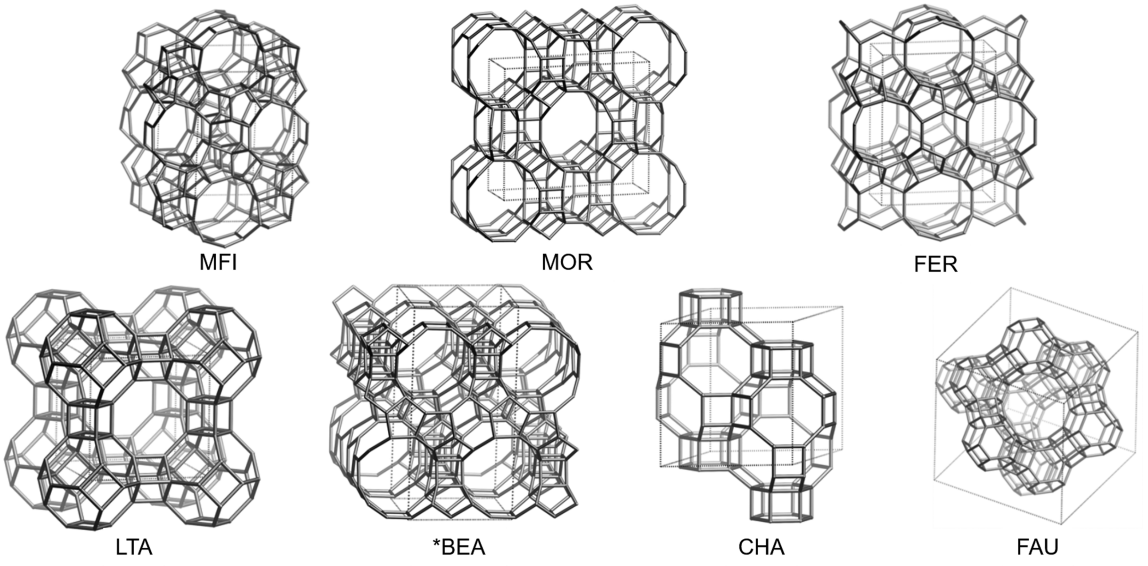

Figure 5. Framework structures of the MFI (includes ZSM-5), MOR, FER, LTA (includes zeolite A), *BEA, CHA (includes SSZ-13), and FAU (includes zeolites X and Y) zeolite topologies. Adapted with permission from ref 38. Copyright 2017 International Zeolite Association.

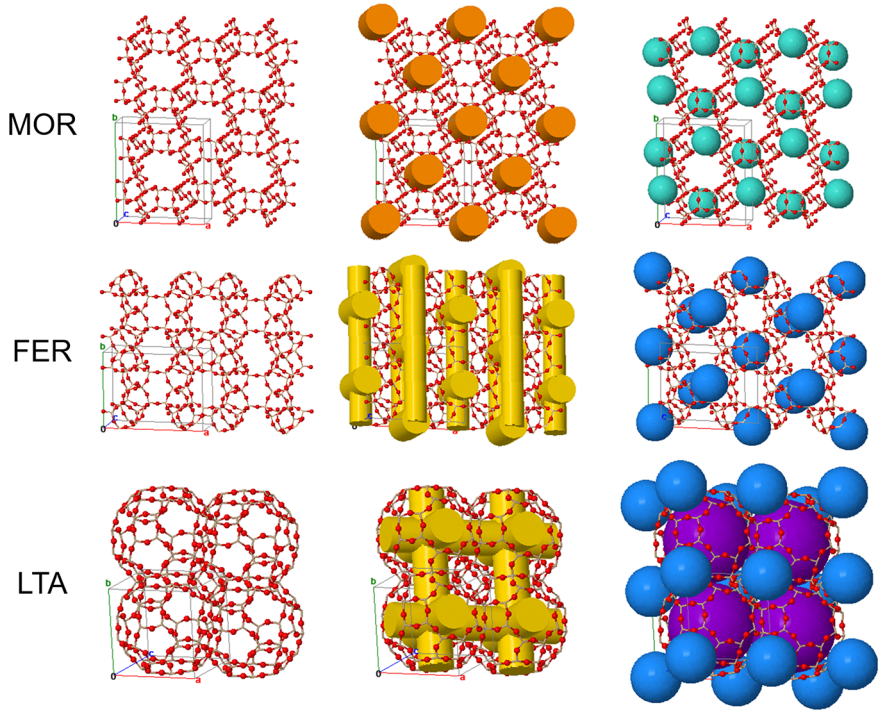

Figure 6. (left) Frameworks of the MOR, FER, and LTA topologies; (middle) channels forming the pore systems of the MOR (one-dimensional), FER (two-dimensional), and LTA (three-dimensional) topologies; and (right) their cages. For MOR the side pockets are indicated (top right structure).[39]

advances enabled by site-selective spectroscopy, which limits interference from spectator metals. Insights into reactivity based on rigorous spectroscopy coupled to electronic structure calculations are presented, along with a critical comparison to iron and copper active sites in biology.

2. COPPER AND IRON ZEOLITES

2.1. Zeolite Structure and Properties

Zeolites are crystalline microporous silicates belonging to the group of the tectosilicates. The Web site of the International Zeolite Association (IZA) lists over 200 frameworks whose structures have been solved and recognized by IZA. The majority of these structures are synthesized, but some can be found in nature. The structures are labeled with a framework type code of three capital letters. The structures that are relevant to this review are shown in Figure 5 together with their corresponding three-letter codes.[38] The *BEA topology generally occurs as a disordered structure, consisting of an intergrowth of three polymorphs A, B, and C, and is therefore given an asterisk prefix.

A defining property of zeolites is the presence of channels and cages with free diameters of less than 2 nm. These pores give the zeolites their characteristic microporosity. Channels

DOI: 10.1021/acs.chemrev.7b00344
Chem. Rev. 2018, 118, 2718−2768

may run in one, two, or three directions, forming respectively one-, two-, or three-dimensional pore systems, and the channels may or may not intersect. Access to the cages is dependent on passage through windows of O atoms, connecting the cages to the channels of the pore system. Channels and windows are characterized by the number of O atoms that form them, since this determines their free diameter. The pore systems of MOR (one-dimensional pore system), FER (two-dimensional pore system), and LTA (three-dimensional pore system) are shown in Figure 6.[39] The rings are symbolized with the notation *n*MR with *n* the number of O atoms and MR abbreviating "membered ring". Figure 7 shows 6-, 8-, 10-, and 12MRs and

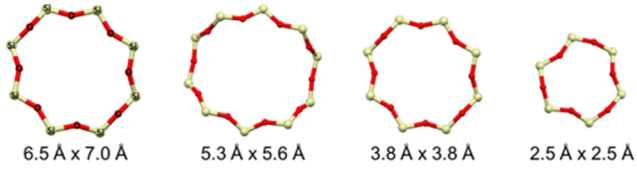

Figure 7. Typical rings and their free diameters (12MR, 10MR, 8MR, 6MR).

their corresponding free diameters. The latter differ somewhat depending on the Si:Al ratio of the zeolite lattice and on the structure type of the zeolite (vide infra). Thus, a 6MR is composed of six $(Si,Al)O_4$ tetrahedra or T-sites. For 8-, 10-, and 12MRs, the number of tetrahedra forming the ring or window is 8, 10, and 12, respectively. A molecule can only pass through a ring when the ring's free diameter equals or exceeds the dimensions of the molecule. This imposes steric constraints on the diffusion of molecules into the microporous network of the zeolite crystals toward the interior of the crystal, where the adsorption or catalytic sites are. Zeolites are therefore described as molecular sieves. An additional feature of zeolites is the isomorphous substitution of Si^{4+} by Al^{3+} in the lattice. This has two consequences: First, Al^{3+} is tetrahedrally coordinated to four lattice oxygen atoms and, because Al−O bonds are longer than Si−O bonds (typically 0.187 nm vs 0.163 nm), this locally distorts the lattice and influences the shape and free diameter of the above-mentioned rings. Second, as Al^{3+} carries one positive charge less than Si^{4+}, the lattice becomes locally negatively charged. One formal negative charge is introduced per Al^{3+} substitution in the lattice. By Loewenstein's rule, Al^{3+} tetrahedra may never be in directly neighboring positions in the framework, so that no Al−O−Al linkages are allowed. The upper limit of isomorphous substitution of Si^{4+} by Al^{3+} therefore yields a maximum Si/Al ratio = 1. Furthermore, the Takaishi and Kato rule dictates that only one Al^{3+} substitution is allowed in one 5MR and Dempsey's rule states that Al^{3+} substitution strives to an even distribution over the lattice. For synthetic zeolites, however, kinetic parameters can cause deviations from the latter rule in zeolite crystallization. For selected zeolites, experimental studies have indicated that Al^{3+} substitutions are inclined to be in closer proximity than expected for a random distribution, but Loewenstein's rule remains valid.[40] An illustration of the four possible aluminum configurations for the 6MR with 5 > Si/Al > 1 in the *BEA topology is given in Figure 8.

The negative lattice charge is compensated by exchangeable cations, giving rise to a cation exchange capacity (CEC) in agreement with the lattice Si/Al ratio. In principle, any cation can be exchanged provided its size is smaller than the free diameter of the channels and cages of the zeolite concerned. When protons are exchanged, Brønsted acid sites (BAS) are introduced as bridging [Al−OH−Si] hydroxyls between neighboring Si^{4+} and Al^{3+}.

The verification of Al distribution in the framework of silicon-rich zeolites is an experimental challenge, and is the subject of a 2012 review by Dědeček et al.[40,41] They identify four types of Al substitution, based on the number of Si atoms (*n*) separating two nearest Al substitutions: (1) $(Al{-}O{-}(Si{-}O)_{n=1}{-}Al)$ sequences, which are quantified with ^{29}Si NMR; (2) $(Al{-}O{-}(Si{-}O)_{2\leq n\leq 3}{-}Al)$ sequences in a single ring, which

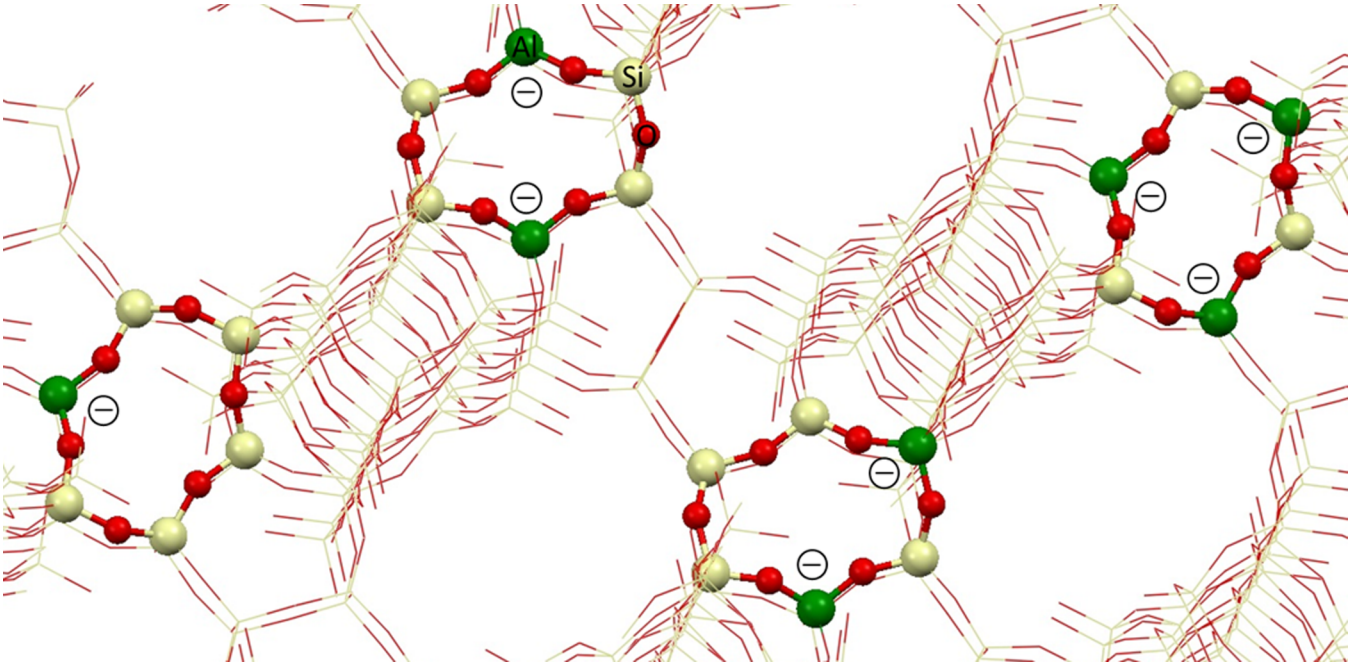

Figure 8. Examples of allowed Al distributions in *β*-6MR sites, where qualitative rules on Al distributions in zeolites allow for one, two, or three Al T-sites.

DOI: 10.1021/acs.chemrev.7b00344
Chem. Rev. 2018, 118, 2718−2768

Table 1. Number of Al−O−Si−O−Si−O−Al Sequences for Selected Zeolites[40]

zeolite	Si:Al	unit cell composition[a]	no. Al−O−Si−O−Si−O−Al per unit cell
ZSM5	12	$[M_{7.38}]^{7.38+}[Al_{7.38}Si_{88.62}O_{192}]^{7.38-}$	3.10
ZSM5	30	$[M_{3.10}]^{3.10+}[Al_{3.10}Si_{92.90}O_{192}]^{3.10-}$	0.93
FER	10	$[M_{3.27}]^{3.27+}[Al_{3.27}Si_{32.73}O_{72}]^{3.27-}$	1.08
*BEA	15	$[M_{4.00}]^{4.00+}[Al_{4.00}Si_{60.00}O_{128}]^{4.00-}$	1.30

[a]The variable cations are indicated by M, where each M stands for a singly positively charged cation equivalent.

are quantified by NIR−UV−vis spectroscopic quantification of Co^{2+} after subtraction of type 1; (3) $(Al-O-(Si-O)_{n\geq 2}-Al)$ sequences not in a single ring, but within close distance, which are quantified by $Co(H_2O)_6^{2+}$ titration with subtraction of type 2; (4) $(Al-O-(Si-O)_{n\geq 2}-Al)$ sequences not in a single ring and with the Al substitutions too separate to accommodate $Co(H_2O)_6^{2+}$, which make up the balance of total lattice Al. Note that the distinction between these four types is dependent on the assumption that Co^{2+} coordination only occurs at $(Al-O-(Si-O)_{n\leq 3}-Al)$ sequences in a single ring, which the authors based on a periodic DFT study on Zn^{2+} in MOR. Additionally, the distinction between types 3 and 4 is arbitrarily defined based on $Co(H_2O)_6^{2+}$ exchange, and not directly on Al positioning.

Also for the exchange of TMI other than cobalt, $(Al-O-(Si-O)_{n\leq 3}-Al)$ in a single ring, and $(Al-O-(Si-O)_2-Al)$ sequences in 6MRs in particular, are of importance. These are particularly apt to accommodate divalent TMI. The occurrence of $(Al-O-(Si-O)_2-Al)$ sequences has been quantified for selected zeolite synthesis conditions by the method described in the previous paragraph, and is dependent on the Si:Al ratio, as illustrated in Table 1.

Di Iorio et al. recently suggested a strategy for influencing the relative position of Al^{3+} substitution in CHA based on a steric/electrostatic effect.[42] Balancing the localized lattice charges in the growing crystallites with bulky *N,N,N*-trimethyl-1-adamantylammonium ($TMAda^+$) cations would obstruct the approach of other $TMDA^+$ cations and prohibit a second nearby lattice charge to be incorporated. Consequently, Al^{3+} substitutions are forced into a more separated configuration. Inclusion of smaller cations, such as Na^+, on the other hand, allows the balancing of two charges in a single 8MR, thus allowing a nearly statistical distribution of Al^{3+} substitution (Figure 9). The hypothesis was

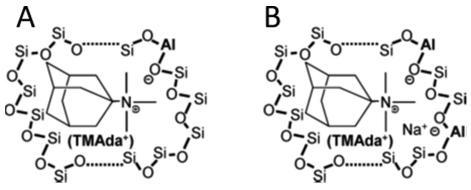

Figure 9. (A) Isolated Al^{3+} substitution in CHA synthesis in the absence of small cations (Na^+). (B) Nearby Al^{3+} substitution in CHA synthesis in the presence of small cations (Na^+). Reproduced from ref 42. Copyright 2016 American Chemical Society.

tested using the $Co(H_2O)_6^{2+}$ titration method mentioned earlier, and is subject to the same assumptions.

The crystallographic position of Al^{3+} substitution in the zeolite framework determines the siting of extraframework cations in the pore system. While through refinement of X-ray and neutron diffractograms the positioning of T-sites is known for most zeolite topologies,[38] it remains a challenge to distinguish between Al and Si T-atoms with these methods. Zegenhagen et al.[43] succeeded in determining the Al^{3+} substitution in a scolecite zeolite using X-ray standing waves with a synchrotron source, but they did so on a highly perfect single crystal. For powder spectra, Rietveld refinement,[44,45] although seldom straightforward on zeolites due to intergrowth of different crystallographic phases and often large, complex unit cells, remains the best method to solve the structure. An indirect approach is to look at the crystallographic positioning of exchanged cations. Similarly, these can be located through X-ray diffraction (XRD) refinement methods such as Rietveld refinement and the maximum entropy method.[46,47] Possible exchange sites, regardless of Al^{3+} position, have been identified and tabulated for most common zeolites.[48,49] However, fractional occupancy of exchange sites, high diversity of exchange sites, and the small number of extraframework cations compared to atoms in the lattice prohibit a full account of the cations.[48] Especially challenging are materials with high Si/Al and multivalent cationic species. High energy synchrotron sources alleviate these problems in part, but remain largely insufficient. Short-range experimental techniques such as solid-state NMR, EXAFS, XANES, XPS, EPR, infrared spectroscopy, Raman, DR-UV−vis−NIR, and the use of probe molecules have assisted the interpretation of long-range powder XRD data.[40,47,50,51] Lastly, theoretical work with Monte Carlo optimizations and periodic DFT models are used to further complement experiment.[40,52]

2.2. TMI Exchange

The most frequently applied method of loading TMI in zeolites is aqueous ion exchange of soluble TMI complexes. In dilute aqueous solution, TMI ions are fully hydrated (e.g., $[M(H_2O)_6]^{2+}$) and can pass through the 8MR, 10MR, and 12MR windows and channels but cannot pass through the 6MR windows. Aqueous ion exchange must be performed in strictly controlled pH conditions to avoid unwanted side reactions. At high pH, silanol groups (point of zero charge = 6.0) on the zeolite surface and defects are deprotonated and participate in the exchange. Besides this, TMI may precipitate at elevated pH, and oligomeric TMI complexes formed in the solution are exchanged. These two phenomena lead to nonstoichiometric or over-exchanged zeolites. Stoichiometric exchange means that the positive charge of the TMI exchanged into the material exactly balances the negative charge of the lattice. For a divalent TMI, this implies that the molar ratio TMI:Al = 0.5. Upon over-exchange, this ratio exceeds 0.5, and the excess charge is balanced by other negative charges, not related to framework aluminum. At exceedingly low pH, exchange is hampered by competitive exchange of H^+ and TMI. As a result, mixed (H^+,TMI)-zeolite is obtained.

Cu^{2+} precipitates at pH >7.0. The recommended pH for aqueous Cu^{2+} ion exchange is $4.0 < pH < 6.0$, which is a feasible range for material preparation. For Fe^{3+}, however, aqueous

DOI: 10.1021/acs.chemrev.7b00344
Chem. Rev. 2018, 118, 2718−2768

exchange of $[Fe(H_2O)_6]^{3+}$ is inevitably accompanied by unwanted side reactions because Fe^{3+} precipitates at pH ≥2.2.

To avoid side reactions, three other strategies have been explored: (1) The first is exchange of Cu^+ and Fe^{2+}, which is a cumbersome procedure because these exchanges have to be performed in the strict absence of O_2. (2) The second strategy is solid state ion exchange or heating a mechanical mixture of—preferably—a H-zeolite and a salt of the TMI with a relatively low melting point. The exchange reactions can be written as

$$CuCl_2 + \text{H-zeolite} \rightarrow \text{Cu-zeolite} + 2HCl(g)$$

$$FeCl_3 + \text{H-zeolite} \rightarrow \text{Fe-zeolite} + 3HCl(g)$$

Water must be avoided, as it leads to an acidic solution in the channels and cavities that may attack the lattice resulting in local lattice breakdown. (3) The third technique is impregnation of a TMI complex dissolved in an organic solvent into the zeolite. The ligands of the complex have to be removed by calcination. Impregnation of $Fe(acac)_3$ (acac = acetylacetonate) in toluene, for example, was employed to prepare the α-Fe sites discussed in section 5.1.1. Upon calcination, the acac ligands are decomposed to CO_2 and H_2O, and three H^+ of the zeolite are consumed in this process:

$$Fe(acac)_3/\text{H-zeolite} + 17.5O_2 \rightarrow Fe^{3+}\text{-zeolite} + 15CO_2 + 11H_2O$$

At high Fe loadings, where the zeolite charge is insufficient to host the impregnated TMI, Fe_2O_3 and Fe_3O_4 nanoparticles are formed.

Regardless of the strategy to load TMI into the zeolite, the TMI complexes have to diffuse through channels and cavities to ensure a homogeneous distribution of the TMI in the zeolitic crystals.

2.3. Activation and Autoreduction

Activation is a high temperature treatment aimed at removing all volatile inorganic and organic molecules adsorbed in the microporous system of zeolites. As ion exchange is usually performed in water, activation results in most cases in the removal of adsorbed water as well.

Organic molecules originating from ion exchange with organic salts and organic templates from zeolite synthesis are desorbed and/or decomposed. In the latter case the decomposition products are desorbed. When the ligands are removed by calcination/activation, the naked TMI coordinate to lattice oxygen atoms in the vicinity of the negative lattice charges, i.e., the Al tetrahedral (vide supra). Common TMI exchange sites for relevant topologies are shown in Figure 10,[40,53] and these are subject to aluminum substitution as described in section 2.1.

After the removal of organic ligands and water, further temperature elevation in vacuo or in inert atmosphere results in bare TMI coordinated to lattice oxygens. Two side reactions can occur.

First, in overexchanged zeolites, condensation leads to polynuclear TMI species of the type $[M_x^{n+}O_y]^{(xn-2y)+}$ (x = 1, 2, 3), and a zeolitic material containing a range of TMI clusters from monatomic to oxidic crystals at the external surface of the zeolite crystals. Thermodynamic calculations indicate that larger copper oxide clusters, at least up to pentamers, are more stable compared to smaller clusters when embedded in Cu-MOR and Cu-MFI due to the extra stabilization by an increased degree of oxygen coordination.[54] Consequently, copper clusters with increasing nuclearity become increasingly abundant at higher copper loadings. At overexchange (Cu^{2+}/Al > 0, 5) on H-MOR, CuO_x nanocrystals were detected with transmission electron microscopy (TEM) and single Al sites were compensated by monovalent $[Cu^{2+}OH^-]^+$ species.[55] Cluster growth in the MOR zeolite was found to be most favorable in the side pockets (Figure 6) with two symmetrically oriented aluminum tetrahedra on opposite sides of the 8MR channel.[54] In applications, it is commonly desirable to specifically stabilize a single TMI species. Other TMI species, not relevant to the intended purpose, are seen as "spectator" species and are best avoided by careful control of the exchange parameters. Often, high active site purity is achieved by limiting the loading of the TMI on the zeolite to very dilute concentrations. Developing strategies to extrapolate high active site purity to elevated metal loadings will be key in improving space-time yield and catalyst productivity for TMI zeolites to industrially relevant levels.

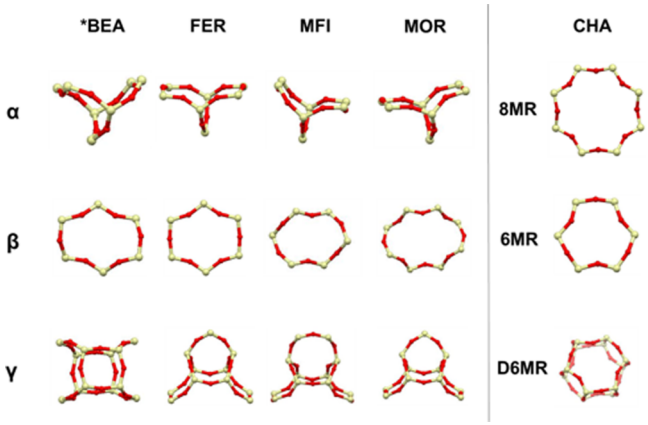

Figure 10. Common exchange sites for TMI after calcination for the *BEA, FER, MFI, MOR, and CHA topologies. Reproduced with permission from ref 53. Copyright 2000 Elsevier.

In the second side reaction, Fe^{3+} and Cu^{2+} zeolites undergo an autoreduction upon activation in inert atmosphere; this is the reduction of Cu^{2+} to Cu^+ and Fe^{3+} to Fe^{2+} accompanied by oxidation of O^{2-} ions to O_2. The O^{2-} ions may originate from the lattice, from residual water molecules, or from extraframework oxygen ($O_{Extraframework}$) atoms.

For the autoreduction of Fe^{3+}, one may formally write

$$2[Fe{-}OH]^{2+} \rightarrow [Fe{-}O{-}Fe]^{2+} + H_2O(g)$$

$$[Fe{-}O{-}Fe]^{2+} \rightarrow 2Fe^{2+} + 0.5O_2(g)$$

Autoreduction of Fe^{3+} to Fe^{2+} in zeolites was determined to range between 63 and 67% of the total Fe content,[56,57] although Sobalik et al.[58] obtained 81−96%. This difference can probably be ascribed to differences in introduction of Fe in the zeolite. These values are, however, obtained from zeolites with low Fe loadings of 7−14% of the cation exchange capacity (CEC), and even then several Fe^{2+} species were identified. Higher levels of Fe loading lead to the formation of oligomeric Fe species, complicating the chemistry of autoreduction strongly since both isolated Fe^{3+} ions and Fe_2O_3 and Fe_3O_4 are subject to autoreduction.

$$6Fe_2O_3 \rightarrow 4Fe_3O_4 + O_2(g)$$

$$2Fe_3O_4 \rightarrow 6FeO + O_2(g)$$

To avoid these complications, Snyder et al.[35] obtained Fe^{2+} zeolites with close to 100% of Fe^{2+} by autoreduction in He at

DOI: 10.1021/acs.chemrev.7b00344
Chem. Rev. 2018, 118, 2718−2768

900 °C, followed by H_2 reduction at 700 °C. The total amount of Fe^{2+} was determined by Mössbauer specstroscopy to represent more than 90% of the total Fe content. Three types of Fe^{2+} species were found: $Fe^{2+}(1)$ with a d−d band envelope around 5000 cm^{-1}, $Fe^{2+}(2)$ with a d−d band envelope in the region around 9000 cm^{-1}, and $Fe^{2+}(3)$ with a d−d band at 15 900 cm^{-1}. The former two species have not been studied in detail, but $Fe^{2+}(3)$ has been characterized by magnetic circular dichroism (MCD) and Mössbauer spectroscopy and assigned to a square planar coordinated Fe^{2+} (see section 5.1.2).

For the autoreduction of Cu^{2+}, the following reactions have been proposed in the literature:[59−61]

$$2[Cu{-}OH]^+ \rightarrow [Cu{-}O{-}Cu]^{2+} + H_2O(g)$$

$$[Cu{-}O{-}Cu]^{2+} \rightarrow 2Cu^+ + 0.5O_2(g)$$

Alternatively, one may write

$$2[Cu{-}OH]^+ \rightarrow Cu^+ + Cu^{2+}{-}O^- + H_2O(g)$$

$$Cu^+ + Cu^{2+}{-}O^- \rightarrow 2Cu^+ + 0.5O_2(g)$$

The released oxygen molecules are derived from the $[Cu{-}OH]^+$ species above 523 K in vacuo or inert atmosphere. In early research on Cu-Y zeolites (FAU topology, Figure 5, Si/Al ≥ 1.5) Beyer and Jacobs[62] proposed that the reduction of Cu^{2+} to Cu^+ is accompanied by release of lattice oxygens and Al from the lattice. The lattice oxygens desorb as O_2 and Al takes an extraframework position.

The autoreduction has been quantified for Cu-MOR and Cu-MFI. Cu-MOR, activated in O_2, contains three distinct Cu^{2+} species:[63] two are isolated (noninteracting) Cu^{2+} ions with respectively $g_{\|}$ = 2.32 and $g_{\|}$ = 2.27. The third is a bent dinuclear oxo complex: $[Cu{-}O{-}Cu]^{2+}$. Upon heating in vacuo (He) at 180 °C (453 K), O_2 is released and both Cu^{2+} with $g_{\|}$ = 2.27 and $[Cu{-}O{-}Cu]^{2+}$ are reduced to Cu^+ in agreement with the reactions given above. On a sample with Cu/Al = 0.43, 0.50 mmol/g of Cu^{2+} is reduced in total: 0.07 mmol/g isolated Cu^{2+} and 0.43 mmol of Cu^{2+} in the form of the dinuclear complex. This amounts to 70% of the total Cu content.

Moretti et al.[64] quantified the amount of Cu^+ formed in the autoreduction reaction of Cu-ZSM-5 (MFI topology, Figure 6) by measuring the amount of Cu−CO complexes and the amount of irreversibly adsorbed N_2. The CO measurement resulted in 80% of the total amount of Cu as monovalent Cu^+, irrespective of the exchange level or the Cu content.

2.4. Factors Influencing Active Site Nuclearity

The formation of a bent dinuclear $[Cu{-}\mu{-}O{-}Cu]^{2+}$ complex upon O_2 activation contrasts with the formation of $[Cu_3(\mu\text{-}O)_3]^{2+}$ in the absence of spectators (i.e., single-site tricopper) reported by Grundner et al.[55] upon O_2 activation of Cu-MOR and Cu-MFI. Both were ion-exchanged with 0.01 M aqueous copper(II) acetate. Two differences in the preparation of both materials can, however, be identified. First, the $[Cu_3(\mu\text{-}O)_3]^{2+}$ materials were exchanged from a parent material in the proton form (H-MOR and H-MFI), as opposed to a parent material in the sodium form (Na-MOR and Na-MFI) for the $[Cu{-}\mu{-}O{-}Cu]^{2+}$ materials.[36] Second, the exchange was buffered to a pH 5.7 to obtain the $[Cu_3(\mu\text{-}O)_3]^{2+}$ material. For the $[Cu{-}\mu{-}O{-}Cu]^{2+}$ materials, the exchange was not buffered.[36] The $[Cu_3(\mu\text{-}O)_3]^{2+}$ materials were reported to stabilize only single-site tricopper clusters in Cu,H-MOR from 0 up to 400 μmol of copper/g of catalyst (Si/Al ≈ 12).[55] Compared to previous literature, this is a high concentration of single copper active sites to obtain on a zeolite. The dinuclear $[Cu_2O]^{2+}$ sites in ZSM-5 are present in concentrations leveling off around 720 μmol of copper/g,[65] but with less than 10% of this copper forming the active sites.[66]

Titration of Brønsted acid sites on H-MOR with pyridine and hexane before and after copper exchange indicates a selective stabilization of the $[Cu_3(\mu\text{-}O)_3]^{2+}$ clusters in an 8MR in the MOR side pocket (Figure 6). The high concentration of Al substitution in the 8MR of MOR is expected to play a key role in the selective stabilization of the $[Cu_3(\mu\text{-}O)_3]^{2+}$ clusters, and the specific lattice environment is hypothesized to act as a directing agent toward the trinuclear clusters.[67] This is in agreement with observations on Cu,H-ZSM-5, where Al pairs are mainly located in the 6MR and other rings tend to hold only a single substitution with Al.[40,68,69] In this case, the self-organization into trinuclear sites is only initiated at a 0.20 Cu/Al atomic ratio. Similarly, a Cu/Al ≥ 0.20 ratio on Na-ZSM-5 is required to form the $[Cu{-}\mu\text{-}O{-}Cu]^{2+}$.[36] Below this threshold, isolated Cu^{2+} ions are energetically preferred in the doubly Al^{3+} substituted 6MR of MFI.[67] The importance of aluminum pairing was further demonstrated by comparing copper speciation on H-ZSM-5 samples with a different population of exchange sites containing $Al{-}O{-}(Si{-}O)_{n\leq 3}{-}Al$ sequences. At optimal copper loading, the concentration of $[Cu_3(\mu\text{-}O)_3]^{2+}$ was lower on the sample with less such sequences and the speciation was more heterogeneous.[67] Similarly, in Cu-SSZ-13 (CHA topology, Si/Al > 5), bare divalent Cu^{2+} cations first occupy the most stable positions at doubly substituted 6MR sites. At higher loadings, $[Cu(OH)]^+$ complexes, associated with low temperature SCR activity[70−72] and methane activation,[73,74] are formed in the 8MR exchange sites of CHA with a single aluminum substitution.[70−72,75,76]

In ZSM-5, a decrease in the formation of trinuclear clusters was observed in the presence of alkali metal (Na^+, K^+) and alkaline earth metal (Mg^{2+}, Ca^{2+}) cations.[77,78] Instead, a more heterogeneous mixture of copper species was obtained.[67] The formation of dinuclear copper clusters is observed in spite of ab initio thermodynamic calculations which indicate a higher stability of trinuclear species in Cu-MOR[55] and Cu-ZSM-5.[79] It is known that, like Cu^{2+}, Na^+ preferentially coordinates in the MOR side pockets,[80] while Brønsted acid sites are better accommodated in the unconfined 12MR channels of MOR.[81−83] Possibly, the presence of Na^+ avoids further self-assembly of dinuclear copper into trinuclear species.

Ab initio thermodynamic analyses reveal that TMI behavior under operating conditions may differ significantly from standard characterization conditions. Atmosphere composition and temperatures are expected to be of influence.[76] Furthermore, the presence of water hydrating the copper cations may mobilize the extraframework cations enabling a redistribution over the lattice.[61,71,75,77] The $[Cu(OH)]^+$ species in Cu-SSZ-13 is suggested to only be stable at high temperatures (>250 °C) in oxidizing conditions. In inert atmosphere tricoordinated $[Cu(OH)]^+$ autoreduces to form bare, two-coordinated Cu^+. The autoreduction can be reversed in an O_2 atmosphere with 5% H_2O at 400 °C.[72] It is interesting to note here that $[Cu(OH)]^+$ is predicted by DFT to be present in a limited amount (∼10%) within a temperature range up to 450 °C in O_2 atmosphere with 0.5−5% H_2O. This is in agreement with the fraction of active copper estimated as water-resistant active sites in methane to methanol conversion estimated on Cu-SSZ-13 by Wulfers et al.[84]

On a comparable note, trinuclear copper cluster stability on Cu,H-ZSM-5 is calculated to exceed the stability of binuclear

DOI: 10.1021/acs.chemrev.7b00344
Chem. Rev. 2018, 118, 2718−2768

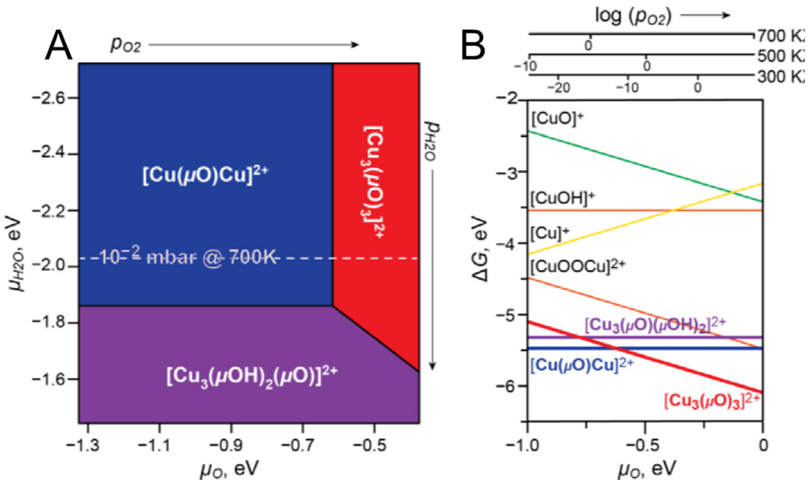

Figure 11. (A) Most thermodynamically stable Cu−oxo clusters in Cu-ZSM-5 zeolite under different conditions of temperature, oxygen partial pressure, and steam partial pressure as determined by ab initio thermodynamic analysis. (B) Cross section of the 3D phase diagram with μ_{H_2O} fixed at 10^{-2} mbar at 700 K (dashed line in (A)). Reproduced with permission from ref 79. Copyright 2016 Elsevier.

complexes in O_2 atmosphere. The order of stability is, however, reversed in an O_2-deprived atmosphere (Figure 11).[79] This result can be expected to have an impact on the correct characterization of these sites when they are implemented in reducing reaction conditions.

For iron zeolites, the factors which govern the formation of multinuclear sites remain largely unknown, but it is known that heat treatment, atmosphere composition, and iron loading are influential for iron dispersion.[85−87] Moreover, the exact nuclearity of active oligomers, to our knowledge, has never been directly detected with site selective spectroscopy. Dimeric iron sites have long been proposed as the active sites for N_2O decomposition and CH_4 activation.[57,58,88,89] This proposal was inspired by the dimeric active site in the sMMO enzyme, and further support was given by the average nuclearity derived from EXAFS results as well as TPR experiments.[90,91] At elevated iron loading, speciation between different oligomers becomes prohibitively complex for characterization and any connection between specific iron sites and reactivity becomes difficult to determine. In Fe-ZSM-5, Hammond et al.[92,93] have suggested the presence of a binuclear di-μ-hydroxo bridged Fe complex ($[Fe_2(\mu_2\text{-}OH)_2(H_2O)_2]^{2+}$) with an Fe−O−Fe symmetric stretch at 521 cm^{-1} in the Raman spectrum, though larger nuclearity sites could not be excluded. The 521 cm^{-1} feature was observed to dissipate after reaction with aqueous H_2O_2, after which the material is active in the low temperature oxidation of methane. Li et al.[94] linked a Raman feature at 867 cm^{-1} to a ν(O−O) stretch of a peroxo bridged binuclear iron site active in benzene hydroxylation on Fe-ZSM-5. Similarly, 730 cm^{-1} was assigned to a peroxo stretch associated with a binuclear iron complex in ZSM-5 by Sachtler et al.[95] The large variability in sample preparation and pretreatment makes comparison difficult, and more study on the aspects of iron introduction and pretreatment is needed for better understanding. Reliable spectroscopic probes of various iron sites would be instrumental to derive the workings of iron speciation in zeolites.

2.5. Coordination of Divalent Metal Ions in Dehydrated Zeolites

The study of the coordination of TMI in zeolites was initiated by Klier and co-workers.[96,97] They developed a ligand field model to explain the d−d spectra of the 3d series of TMI based on the ligand field transitions of Co^{2+} and Ni^{2+} in dehydrated zeolite A (LTA topology, Figure 5). The TMI were located on the trigonal axis of a symmetrical 6MR with three O atoms of the 6MR in their first coordination sphere. The point symmetry is D_{3h} if the TMI are located in the plane of the three O atoms, while it is C_{3v} for the TMI located slightly above the plane of the three O atoms. This model was extended by the group of Schoonheydt using a spin Hamiltonian analysis to include the EPR parameters of Cu^{2+} in FAU, LTA, and MOR.[98] In C_{3v}, Cu^{2+} acquires a doubly degenerate ground state and is subject to the Jahn−Teller (JT) effect. This was visualized by allowing Cu^{2+} ions to move off the trigonal axis.

These ligand field (LF) models had two major disadvantages: First, no distinction was made between Al and Si tetrahedra forming the 6MR; second, the zeolite lattice was strictly rigid and only the TMI were allowed to move so as to find a match between the theoretical d−d bands and the experimental spectra. The groups of Schoonheydt and Pierloot[99−102] developed a more detailed coordination model for TMI in zeolites, in particular for Cu^{2+} and Co^{2+}. These efforts were later extended to Fe^{2+} coordination in the 6MRs of zeolite beta (see section 5.1 for details). In this section, the focus will be on coordination of Cu^{2+} to 6MRs in dehydrated zeolites, where models have been optimized within the frame of DFT (with all the Si and Al tetrahedra included). d−d transitions and the EPR g-parameters were calculated on these optimized structures using complete active space perturbation theory (CASPT2). Typical DFT optimized coordination geometries are shown in Figure 12, with the corresponding CASPT2-predicted g-values and ligand field transitions given in Table 2.

The following conclusions could be drawn: (1) Instead of a trigonal coordination, Cu^{2+} adopted a 4-fold coordination, thus maximizing its coordination number. (2) O atoms of Al tetrahedra (Al−O−Si) are more basic than those of Si tetrahedra (Si−O−Si) and are preferentially taken up in the first coordination sphere. (3) As a consequence of (1) and (2), the 6MR is significantly distorted by the TMI. The geometry of the coordination complex is no longer D_{3h} or C_{3v}. (4) Therefore, the lattice is not rigid but is quite flexible so as to fulfill the need of the TMI to maximize its coordination number. (5) The EPR

DOI: 10.1021/acs.chemrev.7b00344
Chem. Rev. 2018, 118, 2718−2768

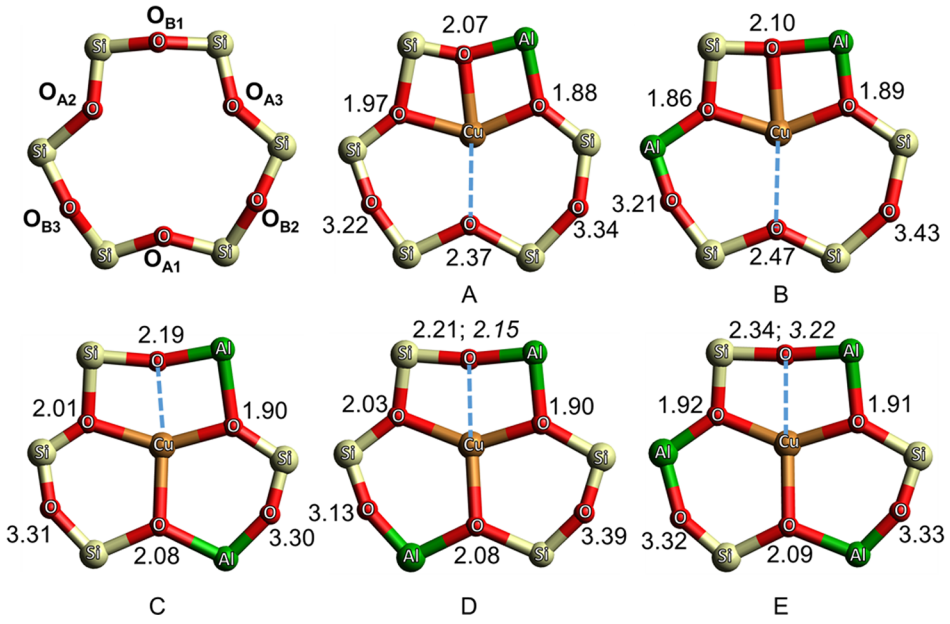

Figure 12. Coordination of Cu^{2+} in 6MRs of FAU with one (A), two (B–D), and three (E) Al atoms (in green), calculated by DFT. Bond distances (Å) are given. The italic distances in (D) and (E) are obtained by CASPT2.[102]

Table 2. CASPT2 Calculated Spectra (cm^{-1}) and *g*-Factors for Cu^{2+} in 6MRs of FAU (Figure 12A–E)[a]

	A	B	C	D	E	D′	E′
X^2A ($d_{x^2-y^2}$)	0	0	0	0	0	0	0
b^2A (d_{xy})	9476	9334	7923	7828	6632	8411	7750
c^2A (d_{xz})	10779	10341	10178	10141	9118	10644	9943
d^2A (d_{yz})	12348	12775	11132	10827	10501	11303	11361
e^2A (d_{z^2})	15353	15346	14776	14575	13924	15108	14850
g_{zz}	2.33	2.31	2.41	2.42	2.48	2.39	2.41
g_{xx}, g_{yy}	2.11, 2.04	2.12, 2.05	2.10	2.10	2.13	2.09	2.11
			2.06	2.06	2.05	2.06	2.05

[a]Clusters A–E represent B3LYP-DFT structures, while clusters D′ and E′ contain a CASPT2 optimized Cu–O_{B1} bond.

parameters and the d–d transitions depend significantly on the number and the siting of Al in the 6MR.

Table 2 summarizes the energies of the ligand field excited states relative to the $d_{x^2-y^2}$ ground state of Cu^{2+} coordinated to the O atoms of the 6MRs found in Figure 12A–E, which can be compared to the experimental d–d transitions and EPR parameters for Cu-FAU in Table 3 (along with experimental values for Cu^{2+} sites in other dehydrated zeolites). The calculated $g_{\|}$-values fall into two ranges: $g_{\|}$ = 2.31–2.32 for 6MRs A and B and $g_{\|}$ = 2.39–2.41 for 6MRs C, D′, and E′ (the latter in agreement with experiment). The calculated d–d transitions fall in the experimental range (see Table 3), but the experimental resolution is too low to resolve the two Cu^{2+} species. D′ and E′, which have CASPT2-optimized Cu–O_{B1} bonds, were therefore chosen as models of the Cu^{2+} sites in FAU based on agreement with experiment. This demonstrated that the spectroscopic signatures of Cu^{2+} coordinated to lattice oxygens in 6MRs of zeolites are determined by the number and distribution of the Al tetrahedra in the ring.

Conclusions drawn from Cu-bound 6MRs in FAU were found to map onto the spectroscopy of Cu^{2+} coordinated to 6MRs in MOR shown in Table 3.[99] Two Cu^{2+} species are observed with distinct d–d transitions at 13 500 and 16 500 cm^{-1}. The former corresponds to a Cu^{2+} species with $g_{\|}$ = 2.32; the latter corresponds to a Cu^{2+} species with $g_{\|}$ = 2.27. Cu^{2+} species with similar EPR parameters are observed for Cu-ZSM-5; however, d–d bands corresponding to individual species could not be resolved. A 6MR model with one Al gives an almost perfect square planar geometry with $g_{\|}$ = 2.27 and the $E(d_{z^2})$ – $E(d_{x^2-y^2})$ transition around 16 500 cm^{-1}. For the other Cu^{2+}

Table 3. Experimental EPR Parameters and d–d Transitions of Cu^{2+} in Dehydrated Zeolites

	EPR		
zeolite	$g_{\|}$[a]	$A_{\|}$[a] (cm^{-1})	d–d (cm^{-1})
LTA	2.37–2.41	(130–145) × 10^{-4}	*10500*; 12200; 15100
FAU	2.36–2.41	(120–145) × 10^{-4}	*10300–10700*; 12600; 15000
	2.30–2.34	(167–188) × 10^{-4}	
MOR	2.27	191 × 10^{-4}	16750
	2.32	169 × 10^{-4}	*13600*
CHA	2.358	155 × 10^{-4}	*10700*, *12900*, *14800*
	2.325	162 × 10^{-4}	
MFI	2.26–2.28	180 × 10^{-4}	*13400* (broad)
	2.30–2.33	(157–173) × 10^{-4}	

[a]$g_{\perp}$ and $A_{\perp}$ are not included because they are—within experimental error—the same for all Cu^{2+} species ($g_{\perp}$ = 2.06–2.075). This is because of the low resolution of the EPR powder spectra in the perpendicular region of the spectrum. The most intense d–d transitions are in italics.

DOI: 10.1021/acs.chemrev.7b00344
Chem. Rev. 2018, 118, 2718–2768

species, a 6MR with two Al's gives agreement between theoretical and experimental data, i.e., a d−d band maximum around 13 500 cm^{-1} and $g_{\|}$ = 2.32, again demonstrating that the Al T-sites within a 6MR have a significant impact on the electronic structure of the resulting metal-bound site.

The above results from spectroscopy and calculations enabled quantitative comparison of the ligand fields provided by 6MRs in MOR and FAU. For these lattices, the ligand field excited states of Cu^{2+} in the 6MRs are characteristic of sites with nearly square planar geometry. This is shown by the small difference between the d_{xz} and d_{yz} states, which are degenerate in rigorous D_{4h} symmetry. (As shown in Table 2, this difference is in the ranges 400−600 cm^{-1} for MOR[99] and 2400−650 cm^{-1} for 6MRs of FAU.) The ligand field strength of square planar sites is expressed by $10Dq = E(d_{xy}) - E(d_{x^2-y^2})$. $10Dq$ values and average Cu−O distances are summarized in Table 4.

Table 4. $10Dq$ Values and Average Cu−O Distances of Cu^{2+} in Various Six-Membered Rings of FAU (Figure 12) and MOR (Figure 10)[99]

sites of FAU	no. of Al	$10Dq$ (cm^{-1})	av Cu−O (nm)
A	1	9476	0.2073
B	2	9334	0.2080
C	2	7923	0.2045
D	2	7828	0.2055
D′	2	8411	0.2040
E	3	6632	0.2064
E′	3	7750	0.2035
sites of MOR			
α, γ	1	11020−11623	0.1980−0.2000
α	2	10400−10600	0.2055

From Table 4, the 6MRs of MOR are associated with stronger ligand fields than in 6MRs of FAU. This is in line with the observation that the average Cu−O distance is also shorter in 6MRs of MOR than in 6MRs of FAU. In both cases the ligand field strength decreases with increasing number of Al tetrahedra in the 6MRs, although the average Cu−O distance also decreases. One would have expected the reverse, as Cu^{2+} preferentially coordinates to the O atoms of the Al tetrahedra and these O atoms are more basic than the O atoms bridging two Si atoms (Si−O−Si).[103−105] However, this is counteracted by distortions away from square planar geometry. Deviations of O−M−O angles from 90°, lone pairs on the lattice O ligands becoming misaligned with the lobes of $d_{x^2-y^2}$ (misdirected valence), and out-of-plane distortions of the Cu atom could all contribute to a diminished $d_{x^2-y^2}/d_{xy}$ splitting.

3. ACTIVE SITE SPECTROSCOPIC PROBES

In bioinorganic chemistry, many spectroscopic techniques have been developed to focus on metal active sites in a dominant protein matrix. The goal in metallozeolite chemistry is similar: to focus on a metal active site within a dominant aluminosilicate matrix. A critical difference here is the presence of spectator metal centers. These can be difficult (or impossible) to distinguish from active sites using bulk techniques such as EXAFS and magnetic susceptibility. On the other hand, methods with single-site resolution (e.g., diffuse reflectance UV−vis, magnetic circular dichroism, electron paramagnetic resonance, and Mössbauer spectroscopy—vide infra) enable correlation of spectroscopic features to individual metal centers. This is often accomplished by tracking spectral changes associated with reactivity. Active site spectroscopic handles can then be probed selectively using, e.g., resonance Raman spectroscopy and variable-temperature variable-field magnetic circular dichroism spectroscopy (VTVH-MCD). This section provides an overview of the methods and associated experimental strategy used to elucidate Fe and Cu active sites in zeolites and their reactive metal−oxo intermediates. For most of the studies covered in this review, these techniques are applied to samples in the gas phase that operate under mild conditions (i.e., gas−solid operation). In most cases, their extension to catalysts operating in the liquid−solid or gas−liquid−solid regime is straightforward. For systems that operate at elevated temperatures and pressures, a current challenge is developing in situ or "operando" techniques to probe active sites that may only exist under such operating conditions.[106]

3.1. Ground and Excited State Properties of Transition Metal Sites

Spectroscopic methods spanning 10 decades of photon energy are currently used to probe ground and excited state properties of transition metal complexes (e.g., for $CuCl_4^{2-}$ in Figure 13).

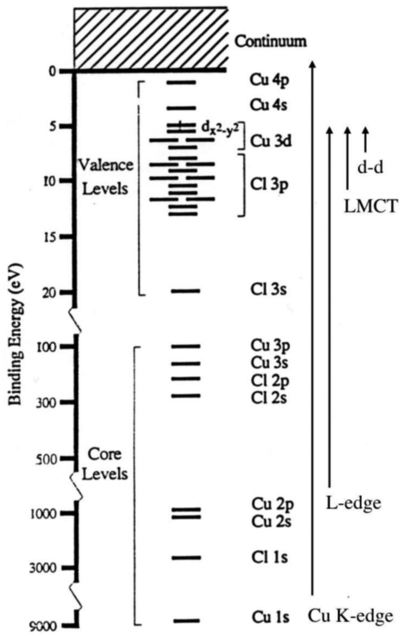

Figure 13. Electronic structure of D_{4h} $[CuCl_4]^{2-}$, showing excited state spectroscopic transitions ranging from 1 to 10 000 eV. Ground state methods probe transitions on the order of 0.0001 eV (not shown).

At low energy, microwave photons are used to drive transitions between ground state sublevels split in the presence of a magnetic field, providing insight into molecular magnetism (see section 3.1.1). Moving up in energy, NIR−vis−UV photons excite electrons among valence levels, resulting in ligand field and charge transfer transitions, which encode information related to metal−ligand bonding (see sections 3.1.2 and 3.1.3). X-ray photons excite electrons from core levels to valence levels and into the continuum. (While core excitations provide extensive chemical insight, XAS does not directly provide the single-site resolution required for metallozeolite chemistry.) Finally, at still higher photon energies (γ), it is possible to probe nuclear excited states through resonant (Mössbauer spectroscopy, section 3.4.2) and nonresonant absorption methods (NRVS, section 3.4.3).

DOI: 10.1021/acs.chemrev.7b00344
Chem. Rev. 2018, 118, 2718−2768

3.1.1. Paramagnetic Ground States. The ground state of a high spin transition metal center with n unpaired d electrons will have a total spin $S = n/2$, resulting in an effective magnetic moment $\mu = g_e\beta(S(S+1))^{1/2}$ in the absence of spin−orbit coupling (SOC), where $g_e = 2.0023$ is the free electron g-value and β is the Bohr magneton. This magnetic moment can be probed using a number of techniques (e.g., magnetic susceptibility, EPR, and VTVH-MCD; see sections 3.3.3 and 3.4.1). Its magnitude reflects the spin state of the metal, and this provides key insight into the metal center's oxidation state and nuclearity (vide infra).

The magnetism of transition metal ions encodes additional information arising from the spin−orbit interaction—a relativistic effect that couples electron spin and orbital angular momenta. SOC effects on ground state magnetism reflect orbital properties that include ligand field splittings and metal−ligand covalency. These effects can be determined experimentally, and then related to molecular electronic structure using ligand field theory. This is generally accomplished using the spin Hamiltonian formalism—a phenomenological description of ground state spectral features arising in EPR (section 3.4.1) and VTVH-MCD (section 3.3.3). The spin Hamiltonian for an effective spin-1/2 system is given in eq 1:

$$\hat{H} = \beta\vec{H}\cdot\tilde{g}\cdot\vec{S} + \vec{I}^{M}\cdot\tilde{A}^{M}\cdot\vec{S} + \sum_{L}\vec{I}^{L}\cdot\tilde{A}^{L}\cdot\vec{S} \quad (1)$$

This Hamiltonian describes the Zeeman splitting of an $S = 1/2$ system in an external magnetic field $\vec{H}$, illustrated in Figure 14

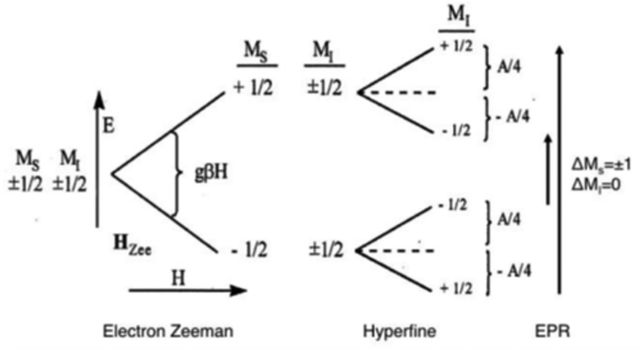

Figure 14. Effects of Zeeman splitting (left, center) and hyperfine coupling A (right) on a system with electron spin $S = 1/2$ and nuclear spin $I = 1/2$.

(including nuclear spin $I = 1/2$). In this expression, β is the Bohr magneton, $\tilde{g}$ is the molecular g-tensor, $\vec{S}$ is the effective electron spin operator, $\vec{I}^{M}$ is the nuclear spin operator of the metal, $\tilde{A}^{M}$ is the metal hyperfine tensor, $\vec{I}^{L}$ is the nuclear spin operator of ligand L, and $\tilde{A}^{L}$ is the hyperfine tensor of ligand L. Molecular g-values (components of the diagonalized g-tensor) can be measured using a number of techniques, including EPR (section 3.4.1), VTVH-MCD (section 3.4.3), and magnetic susceptibility. For transition metal ions, these may deviate significantly from the free electron g-value of 2.0023 due to SOC with low-lying ligand field excited states. These deviations can be related to ligand field splittings and metal−ligand covalencies using equations from ligand field theory.[107−111]

For systems with nonzero nuclear spin (on either the metal or ligands), the ground state will undergo additional smaller splittings due to the hyperfine interaction between the nuclear spin I and the electron spin S (Figure 14). Metal hyperfine coupling (described by the second term in eq 1) can be resolved in EPR, where it splits resonances into $2I + 1$ evenly spaced lines separated by an amount determined by the components of the metal hyperfine tensor $\tilde{A}^{M}$ (see section 3.4.1 for details). There are three contributions to $\tilde{A}^{M}$, each reflecting the nature of the ground state and its covalency.[108,110,111] For a metal complex with unpaired d electrons, the core 2s and 3s electrons are spin-polarized through s/d exchange, resulting in net negative spin density at the nucleus. This leads to an indirect isotropic Fermi contact interaction between the nuclear spin and the electron spin density at the nucleus, given as

$$A_{\text{Fermi}} = \frac{8\pi}{3}g_e\beta_e g_n\beta_n[|\Psi_\uparrow(0)|^2 - |\Psi_\downarrow(0)|^2] \quad (2)$$

where g_e is the free electron g-value, g_n is the nuclear g-value, β_e is the electron (Bohr) magneton, β_n is the nuclear magneton, and the bracketed term is the net spin density at the nucleus. Covalent delocalization of valence d electrons decreases s/d exchange, resulting in a smaller Fermi contact term. Anisotropic contributions to $\tilde{A}^{M}$ arise from spin-dipolar interactions between the spin magnetic moments of the electron and nucleus:

$$A_{\text{spin-dipolar}} = \frac{g_e\beta_e g_n\beta_n}{\langle r^3\rangle}\frac{1}{2}\langle 3\cos^2\theta_e - 1\rangle(3\cos^2\theta_n - 1) \quad (3)$$

In this expression, r is the radial position of the electron, θ_e is the angular position of the electron with respect to the molecular z-axis, and θ_n is the angle between the nuclear spin (oriented along $\vec{H}$) and the molecular z-axis. The expectation values in angled brackets are evaluated over the shape of the occupied d orbital. Since the spin-dipolar interaction is localized on the metal, this contribution also decreases with covalent delocalization. A second anisotropic contribution arises from the dipolar interaction between the orbital magnetic moment of the electron and the spin magnetic moment of the nucleus. This interaction is described by the orbital-dipolar term in the spin Hamiltonian:

$$\vec{H}_{\text{orbital-dipolar}} = \frac{g_e\beta_e g_n\beta_n}{\langle r^3\rangle}[\vec{L}\cdot\vec{I} - \frac{3}{2}\xi[(\vec{L}\cdot\vec{S})(\vec{L}\cdot\vec{I}) + (\vec{L}\cdot\vec{I})(\vec{L}\cdot\vec{S})]] \quad (4)$$

where $\xi = (2l + 1 - 4S)/[S(2l - 1)(2l + 3)(2L - 1)]$. The orbital-dipolar interaction therefore reflects spin−orbit coupling to ligand field excited states, evident from the ground state g-values deviating from 2.0023 (see section 3.4.1 for details).

Superhyperfine coupling, described by the third term in eq 1, arises mostly from delocalization of the electron spin over the nuclear spin of the ligands. As with metal hyperfine coupling, the hyperfine tensor of ligand L ($\tilde{A}^{L}$) includes contributions from Fermi contact and magnetic dipolar interactions. These interactions are weak relative to the hyperfine interaction with the metal. They can often be resolved using EPR, or with higher resolution experiments such as electron nuclear double resonance (ENDOR) and pulsed EPR via electron spin echo envelope modulation (ESEEM).[112]

For systems with more than one unpaired electron ($S \geq 1$), the $2S + 1$ components of the ground state will generally be split in the absence of a magnetic field.[108,109,111] This zero-field splitting (ZFS) is described by an additional term in the spin Hamiltonian:

$$H_{\text{ZFS}} = D(\hat{S}_z^{\,2} - S(S+1)/3) + E(\hat{S}_x^{\,2} - \hat{S}_y^{\,2}) \quad (5)$$

DOI: 10.1021/acs.chemrev.7b00344
Chem. Rev. 2018, 118, 2718−2768

where D and E are the axial and rhombic ZFS parameters, respectively. The effects of axial and rhombic ZFS are different for Kramers (odd number of electrons, 1/2-integer spin) and non-Kramers systems (even number of electrons, integer spin). For Kramers ions, axial ZFS ($D \neq 0$) splits the spin manifold into $\pm M_s$ pair states known as Kramers doublets (Figure 15, left).

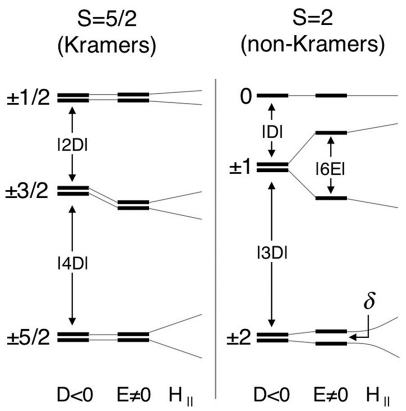

Figure 15. Effects of negative axial zero-field splitting ($D < 0$), a small rhombic zero-field splitting ($E \neq 0$), and magnetic field ($H_{||}$) on Kramers (left) and non-Kramers (right) systems.

Rhombic ZFS ($E \neq 0$) mixes M_s states with $\Delta M_s = \pm 2$. By double-group symmetry, the two components of a Kramers doublet are affected identically by this mixing, and they remain degenerate in the absence of an external magnetic field. For non-Kramers ions, axial ZFS separates the spin manifold into a singly degenerate $M_s = 0$ state along with $\pm M_s$ pair states known as non-Kramers doublets (Figure 15, right). As before, rhombic ZFS mixes M_s states with $\Delta M_s = \pm 2$, but this has an additional effect on a non-Kramers ion. In this case, this mixes and splits the $M_s = \pm 1$ doublet by the amount $S(S + 1)|E|$ ($6|E|$ in Figure 15). For non-Kramers ions with $S \geq 2$, the $M_s = \pm 2$, ± 3, ± 4, ... doublets will also be split, but by incrementally smaller amounts due to higher-order rhombic ZFS (e.g., δ in Figure 15). As a result, the ground state of a non-Kramers system will be nondegenerate even in the absence of an external magnetic field (except in the special case where $D \leq 0$, $E = 0$).

For transition metal ions, SOC provides the dominant mechanism for ZFS. D and E therefore contain information about the ground state electronic wave function, including contributions from low-lying excited states with $\Delta S = 0, \pm 1$. Zero-field splittings can be measured directly using EPR, or inferred from the combined effects of temperature and magnetic field on magnetization (via SQUID magnetic susceptibility or VTVH-MCD).[19,113] For some techniques—EPR in particular—different approaches are required for Kramers versus non-Kramers ions (see section 3.4.1).[108,110] Experimental values of D and E can then be correlated to ligand field splittings reflecting coordination geometry and covalency using ligand field theory. For systems with two or more metal centers coupled by bridging ligands, additional terms describing exchange coupling must be incorporated into the spin Hamiltonian (including isotropic, anisotropic, and antisymmetric exchange).[114,115]

3.1.2. Ligand Field Excited States. Moving up in energy from the ground state to the NIR–vis spectral region, the first electronic excited states of a transition metal complex are generally ligand field transitions, which involve excitations of electrons between valence molecular orbitals with dominantly metal d character. Ligand field transitions can be challenging spectroscopic targets, as they are parity (Laporte) forbidden and therefore weak in absorption ($\varepsilon < 100$ mol^{-1} cm^{-1}). Techniques such as CD (for chiral sites) and MCD (for all sites, see section 3.3) have different selection rules, and ligand field transitions can be observed with considerable intensity in these experiments, particularly in low-temperature MCD (see section 3.3.2).[19,116]

Since the d orbitals participate directly in metal–ligand bonding, ligand field transitions are highly sensitive to coordination geometry and ligand identity, and correlate to each in predictable ways as described by ligand field theory (vide infra). Coordination geometries that may be encountered in metallozeolite and metalloenzyme chemistry are shown in Figure 16,

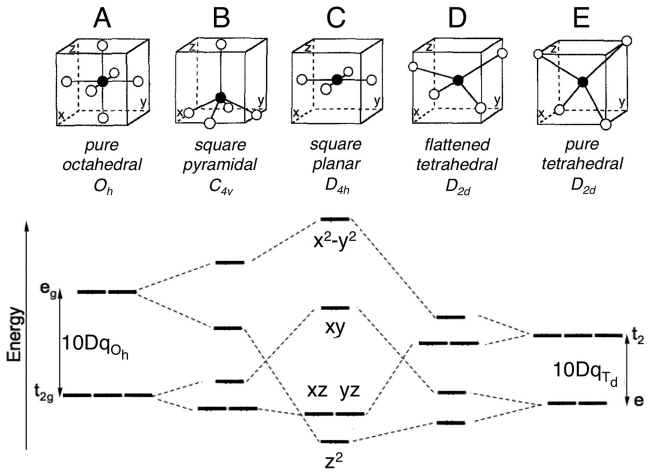

Figure 16. Five commonly encountered coordination geometries for transition metal complexes (top), and their associated ligand field splittings (bottom).

along with characteristic d-orbital splittings. These reflect differences in σ versus π bonding interactions with ligands. For an octahedral metal center with σ/π donor ligands (Figure 16A), the d orbitals split into a triply degenerate t_{2g} set and a doubly degenerate e_g set at higher energy separated by the amount $10Dq_{O_h}$. Removing one axial ligand results in a square pyramidal site (Figure 16B). This removes a strongly destabilizing σ-antibonding interaction with d_{z^2} and weaker π-antibonding interaction with $d_{xz/yz}$. To compensate for axial ligand loss, the equatorial ligands contract, destabilizing $d_{x^2-y^2}$ and d_{xy}. Removing the second axial ligand results in a square planar site (Figure 16C). A key feature of square planar geometry is the large energetic separation between d_{z^2} and $d_{x^2-y^2}$. This is a consequence of a strong σ-antibonding interaction with the ligands (the lobes of $d_{x^2-y^2}$ are directed along the M–L bonds), as well as the unique stability of d_{z^2} in square planar geometry due to 4s mixing in the absence of axial ligands. The effects of a D_{2d} distortion toward tetrahedral geometry—bringing one *trans* pair of ligands above the molecular plane and one pair below the plane—is shown in Figure 16D. This eventually leads to a tetrahedral structure (Figure 16E), with a t_2 level above an e level separated by the amount $10Dq_{T_d} = -4/9(10Dq_{O_h})$. This distortion toward tetrahedral geometry has been particularly significant in bioinorganic chemistry due to its contribution to the properties of the type 1 "blue copper" active sites (see section 6.3.3 for detailed discussion).[117,118]

3.1.3. Charge Transfer Excited States. Moving to higher energy, the next electronic excited states for first row transition

DOI: 10.1021/acs.chemrev.7b00344
Chem. Rev. 2018, 118, 2718–2768

metal centers are charge transfer transitions. For first row metals in zeolites, these are typically ligand to metal charge transfer (LMCT) transitions, which involve excitation of electrons from filled ligand-based valence molecular orbitals into unoccupied or half-occupied metal d orbitals (Figure 17A).

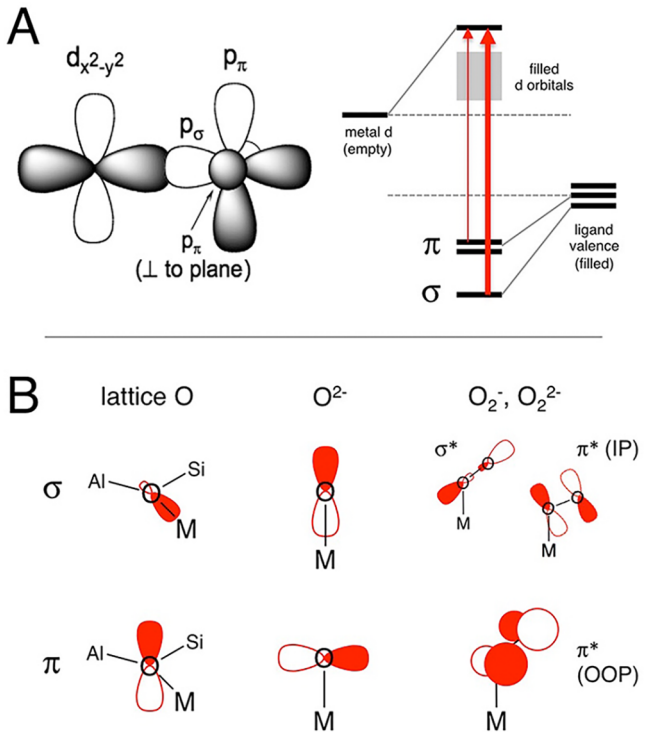

Figure 17. (A) Difference in energy and overlap between empty metal d and filled ligand valence orbitals leads to weak low-energy π and intense high-energy σ charge transfer transitions. (B) Metal−oxygen bonding interactions encountered in metallozeolite chemistry. For O_2-derived ligands (right), there are two perpendicular π^* orbitals that can participate in pseudo-σ (top) and π interactions (bottom), as well as an empty σ^* orbital that can participate in σ back-bonding.

Unlike ligand field transitions, LMCT transitions are electric dipole allowed, and can be intense in Abs spectroscopy (ε > 1000 mol^{-1} cm^{-1}). They may also be strongly coupled to metal−ligand vibrations through excited state distortions, as LMCT transitions involve a large change in bonding moving from the ground state to the excited state. This effect is probed using resonance Raman spectroscopy (see section 3.2).

LMCT transitions occur between orbitals directly involved in metal−ligand bonding. They therefore contain information about donor/acceptor orbital overlap and covalency. For ligands commonly encountered in metallozeolite chemistry (Figure 17B), there are both σ and π lone pairs available for bonding. Zeolite lattice O atoms, which bridge adjacent Al and Si T-sites, have an in-plane σ hybrid lone pair and an out-of-plane p_π lone pair available for bonding. The in-plane p orbital participates in bonding with the T-sites, and is not available as a donor orbital. Oxo ligands (derived from O_2 or N_2O) may bind in a bridging or terminal fashion, with donor interactions from three filled p orbitals (one σ, two π). For O_2-derived ligands (superoxide, peroxide), there is a lone pair available for pseudo-σ donation derived from the filled π^* orbital, a perpendicular π^* orbital (filled or half-filled) available for π donation, and an empty σ^* orbital available for back-bonding from the metal and for electrophilic reactivity. Since σ bonding is stronger than π bonding due to directional orbital overlap, σ lone pairs will be stabilized relative to the π lone pair(s) through bonding with the metal (Figure 17B). σ-LMCT transitions therefore occur at high energy relative to π-LMCT bands, and because LMCT intensity is proportional to donor/acceptor orbital overlap, σ-LMCT transitions are generally more intense.[119]

Bonding interactions are dominated by occupied ligand donor orbitals and unoccupied metal valence orbitals that are close in energy and have significant overlap. Thus, highly covalent ligand−metal bonds exhibit intense, low energy LMCT transitions. These are often associated with ligands having high energy lone pairs (e.g., oxides) and metals with low energy d orbitals (high Z_{eff} metals). Relevant to this review are metal−oxygen intermediates, where covalent bonding leads to intense, low energy oxygen → metal CT transitions. (This is in contrast to ionic complexes, which exhibit weak CT transitions at higher energy, reflecting low covalency.) For these intermediates, charge transfer spectroscopy provides a direct connection between electronic structure and function, as metal−oxygen covalency contributes significantly to reactivity (see sections 4, 5, and 6).

3.2. Resonance Raman Spectroscopy

Like Raman spectroscopy, resonance Raman (rR) spectroscopy is used to study molecular vibrations excited through inelastic scattering of laser photons.[107,119] In rR, the photon energy is tuned to match an intense absorption band associated with a transition to an electronic excited state, resulting in resonant enhanced vibrational scattering. Depending on the specific structural and electronic properties of the excited state, this leads to resonant enhancement of certain vibrations by up to 3−4 orders of magnitude. From an experimental standpoint, this offers two key advantages. First, resonantly enhanced features of an active site are intense and easily resolved above background nonresonant contributions. Second, resonant enhancement is selective for vibrations coupled to a particular absorption feature, making rR a site-selective technique. This is particularly important in metallozeolite chemistry, where rR can be used to resolve the vibrations of a minority species that exists in a heterogeneous distribution of metal sites.

The dominant mechanism for resonant Raman scattering, known as *A*-term enhancement for an electric dipole allowed transition, derives from the first term in the Kramers−Heisenberg−Dirac dispersion equation for the Raman polarizability tensor, shown in eq 6.[120] (Other intensity mechanisms exist, but these reflect vibronic coupling and are generally less important in metallozeolite and non-heme metalloenzyme spectroscopy.[119])

$$A^{\rho\sigma} = \sum_{ev} \frac{\langle \Psi_g | \hat{M}_\rho | \Psi_e \rangle \langle \chi_{gf} | \chi_{ev} \rangle \langle \Psi_e | \hat{M}_\sigma | \Psi_g \rangle \langle \chi_{ev} | \chi_{gi} \rangle}{\nu_{ev} - \nu_{gi} - \nu_L + i\Gamma_{ev}} \quad (6)$$

In this expression, ρ and σ are Cartesian coordinates (x, y, z), M_ρ and M_σ are components of the electric dipole operator, Ψ_g and Ψ_e are the ground and excited state electronic wave functions (respectively), χ_{gi} and χ_{gf} are the initial and final ground state vibrational wave functions, and χ_{ev} is the excited state vibrational wave function. In the denominator, ν_{gi}, ν_{gf}, and ν_{ev} are the initial/final frequencies (energies) of the ground state and the excited state, while ν_L is the photon frequency. Γ_{ev} is a damping factor inversely proportional to the excited state lifetime. Note that $A^{\rho\sigma}$ in eq 6 becomes very large when the photon energy matches the allowed excited state absorption

DOI: 10.1021/acs.chemrev.7b00344
Chem. Rev. 2018, 118, 2718−2768

energy, and it is this behavior in the energetic vicinity of an intense absorption band that leads to resonant enhancement.

From this expression, which includes the square of electric dipole operator, *A*-term enhancement ($\propto A^2$) of vibrational mode χ is proportional to the square of the intensity of the electronic absorption band. It is also proportional to the square of the overlap between the ground and excited state vibrational wave functions. For this to be nonzero, there must be a geometric distortion in the excited state relative to the ground state along the χ normal mode, and since excited state distortions can only occur along totally symmetric normal modes of vibration, only totally symmetric vibrations experience *A*-term enhancement.[120] The energy dependence of this integral follows the band shape since they have the same origin (Figure 18).

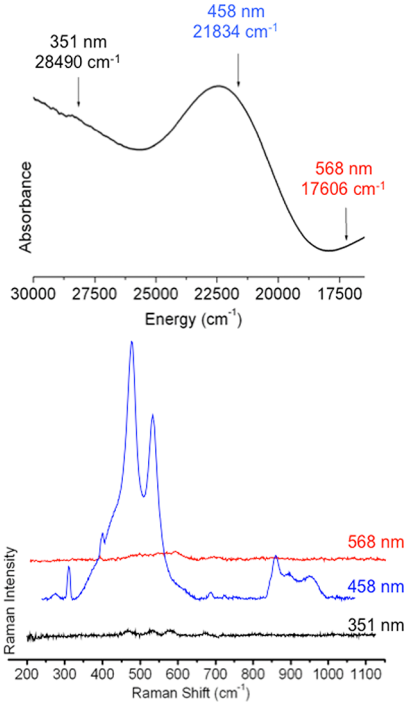

Figure 18. Effect of excitation energy on resonance intensity (bottom), which is maximized for photons tuned to an absorption feature (458 nm, top). Adapted from ref 18. Copyright 2014 American Chemical Society.

rR spectroscopy is often used to probe charge transfer transitions, as these are associated with high absorption intensities and large distortions of the ligand−metal bond involved in the charge transfer transition. This leads to efficient *A*-term enhancement of these ligand−metal vibrations. Large excited state distortions typically derive from weaker M−L bonding in the excited state, leading to M−L elongation. This can be used to assign charge transfer transitions to a specific L−M bond, including the σ (large ES distortion) versus π (smaller ES distortion) contributions to the bonding interaction.[121]

3.3. Magnetic Circular Dichroism Spectroscopy

Magnetic circular dichroism spectroscopy (MCD) involves the induction of circular dichroism by the presence of a longitudinal magnetic field (H parallel to the propagation of the circularly polarized light). This experiment probes Zeeman splittings of paramagnetic ground and excited states, as well as magnetic field induced mixing between states. From the general expression for MCD intensity (eq 7), there are three contributions by which an MCD transition can gain intensity.[122−125]

$$\frac{\Delta A}{E} = \text{const}\cdot\beta H\left[\mathcal{A}_1\left(\frac{\partial f(E)}{\partial E}\right) + \left(\mathcal{B}_0 + \frac{C_0}{k_B T}\right) f(E)\right] \quad (7)$$

In this expression, ΔA is the difference in absorption of left versus right circularly polarized light of energy $E = h\nu$ in the presence of a magnetic field of magnitude H. $f(E)$ is the absorption band shape, and $\partial f(E)/\partial E$ is its first derivative. The constants $\boldsymbol{A}_1$, $\boldsymbol{B}_0$, and $\boldsymbol{C}_0/k_B T$ quantify the magnitude of MCD intensity arising from the linear ***A***-, ***B***-, and ***C***-term mechanisms, described below. $\boldsymbol{A}_1$ is the contribution of any derivative-shaped contribution to MCD intensity; $\boldsymbol{B}_0$ is the contribution of any temperature-independent feature with an absorption band shape, and $\boldsymbol{C}_0$ is the contribution of any feature with the absorption band shape where the magnitude increases in intensity with decreasing temperature (as $1/T$). MCD studies generally focus on paramagnetic metal centers and measure ***C***-term intensity, as this dominates at low temperature and has rich information content.[116] MCD intensity also correlates to a specific chromophore, and it can therefore be site-selective in heterogeneous systems.[35]

3.3.1. *A*- and *B*-Term Mechanisms. For a nondegenerate ground state and a degenerate electronic excited state (Figure 19A)

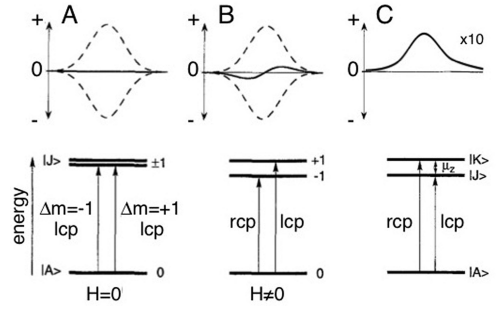

Figure 19. MCD ***A***-term (A, B) and ***B***-term mechanisms (C, with 10× intensity scale).

in the absence of a magnetic field, LCP and RCP transitions occur at the same energy with equal and opposite magnitude, and no net MCD intensity is observed. In the presence of a magnetic field (Figure 19B), the excited state experiences a Zeeman splitting determined by its g-values. If the excited state g-value is nonzero (i.e., for states carrying angular momentum), LCP and RCP transitions from the ground state occur with equal and opposite magnitude, but at different energies (split on the order of 10 cm^{-1} for a 6 T magnetic field). The net effect is in a temperature-independent, derivative shaped feature known as an ***A***-term. ***B***-term intensity has a similar origin, but in this case the MCD signal arises through field-induced mixing between nondegenerate states (states J and K in Figure 19C). The net effect is a temperature independent, absorption shaped feature known as a ***B***-term. If the field-induced mixing occurs exclusively between the two excited states, the result is a pair of ***B***-terms with equal magnitude and opposite sign known as a (temperature-independent) pseudo ***A***-term. Note that temperature-dependent ***B***-term intensity can arise when field-induced mixing occurs between the ground state and a thermally accessible low-lying excited state (vide infra).

3.3.2. The *C*-Term Mechanism. For systems with degenerate ground states, in particular paramagnetic metal centers,

DOI: 10.1021/acs.chemrev.7b00344
Chem. Rev. 2018, 118, 2718−2768

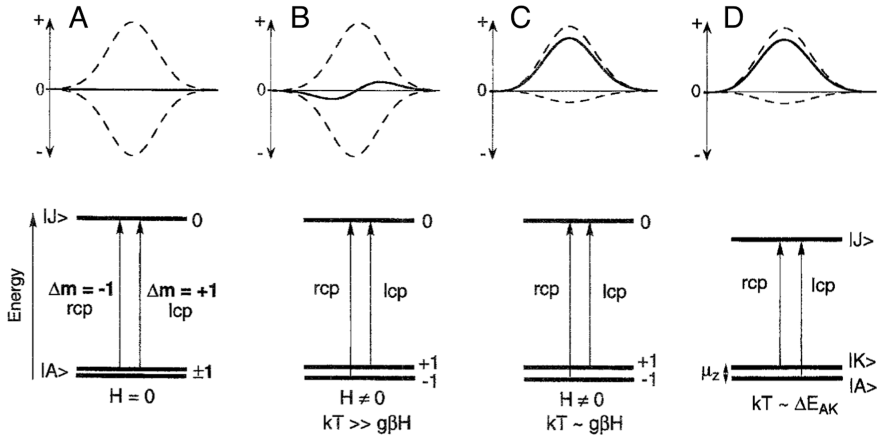

Figure 20. MCD *C*-term (A–C) and temperature-dependent *B*-term mechanisms (D).

temperature-dependent MCD intensity will generally be observed.[116,122,123] In the absence of a magnetic field, LCP and RCP transitions from a degenerate ground state occur at the same energy with equal and opposite magnitude, resulting in no net MCD intensity (Figure 20A). In the presence of a magnetic field, the ground state experiences a Zeeman splitting determined by the ground state's *g*-values. LCP and RCP transitions occur with equal and opposite magnitude, but at different energies (split by $g\beta H$). At high temperature ($k_BT \gg g\beta H$), the components of the ground state are equally Boltzmann populated, and the net effect is a weak derivative-shaped feature (an ***A***-term, Figure 20B). At low temperature ($k_BT \sim g\beta H$), the lowest Zeeman split component of the ground state becomes preferentially Boltzmann populated, resulting in a temperature-dependent, absorption shaped MCD feature called a ***C***-term (Figure 20C). ***C***-term intensity generally dominates at low temperature (by a factor of 100–1000). This is evident from eq 7, which shows ***C***-term intensity is inversely proportional to temperature in the linear limit ($k_BT > g\beta H$). Similar behavior occurs when there is a low-lying thermally accessible excited state that interacts with the ground state through an off-diagonal matrix element in the magnetic field (Figure 20D). This leads to equal and oppositely signed ***B***-term MCD intensity from the interacting levels. Since the ground state is preferentially Boltzmann populated at low temperature, this leads to a temperature dependent ***B***-term. If the interacting levels are separated by an amount that is comparable to the Zeeman splitting ($\Delta E \sim g\beta H$), this results in a nonlinear temperature-dependent ***B***-term (see section 3.3.3 and Figure 22).

The information content of ***C***-term MCD intensity is high.[122] It reflects magnetic properties of the ground state and excited state involved in the MCD transition, including ground state spin Hamiltonian parameters (see section 3.3.3) and excited state *g*-values and spin–orbit coupling. This can be seen from the expression for orientation averaged ***C***-term intensity for a transition between the ground state *A* and excited state *J*:

$$\boldsymbol{C}_0 = -\frac{1}{|3d_A|}\sum_{A,J}\langle A|\vec{L} + 2\vec{S}|A\rangle\cdot(\langle A|\hat{\mu}_e|J\rangle \times \langle J|\hat{\mu}_e|A\rangle) \quad (8)$$

In this expression, d_A is the degeneracy of the ground state, μ_e is the electric dipole operator, and the sum is carried out over all components of the ground state *A* and excited state *J*. For the cross product in this expression to be nonzero, two nonzero perpendicular transition moments are required. This condition is satisfied if either the ground or excited state carries orbital angular momentum. On the other hand, transitions between orbitally nondegenerate states can only have a transition moment in a single direction. Paramagnetic species with orbitally nondegenerate ground states can exhibit significant ***C***-term intensity, however. In this case, spin–orbit coupling mixes states with different polarizations, satisfying the requirement for two perpendicular transition moments. (Note that the spin–orbit mixing must occur along a third, mutually perpendicular direction.) The magnitude of spin–orbit coupling is high for transition metal centers relative to, e.g., organic ligands. This, combined with the inherently strong spin–orbit mixing of ligand field states, means that d–d transitions can be significantly enhanced in low-temperature MCD relative to Abs. The ability to resolve these otherwise weak features is a key advantage of MCD. Since the spin–orbit mixing of charge-transfer states is generally weaker, charge-transfer enhancement in MCD (relative to Abs) is not nearly as pronounced. It is therefore possible to discriminate between ligand field and charge transfer excitations based on their relative intensities in MCD and Abs. Finally from eq 8, if the *g*-values (derived from $\langle L + 2S\rangle$) are known (e.g., from EPR, see section 3.4.1), it is possible to experimentally determine the polarization of an MCD transition even in a randomly oriented sample. If the orientation of the *g*-tensor is known relative to the molecular axes, this can greatly facilitate spectral assignments—especially for charge-transfer transitions, which tend to be polarized along M–L bonds.

3.3.3. Saturation Magnetization: Variable-Temperature Variable-Field MCD. For a paramagnetic transition metal site, ***C***-term MCD intensity reflects the magnetization of the metal center. MCD can therefore provide the same ground state information as magnetic susceptibility, but with a number of distinct advantages. First, there is no diamagnetic contribution to ***C***-term intensity. It is therefore straightforward to study the magnetization of <1 wt % metal in diamagnetic matrix using MCD. This is particularly important for metal centers in metalloenyzmes and metallozeolites. Second, a component in a mixture can be studied selectively through its characteristic MCD features. This makes it possible to focus on the ground state of a single species, even if it exists within a distribution of paramagnetic spectator sites (as is often the case in metallozeolite chemistry). Finally, MCD offers additional information concerning the polarization of electronic transitions.[19,113,122]

Saturation magnetization occurs when the thermal energy is on the order of, or smaller than, the Zeeman splitting of the ground state and the system is no longer in the Curie limit.

DOI: 10.1021/acs.chemrev.7b00344
Chem. Rev. 2018, 118, 2718–2768

Like magnetic susceptibility, *C*-term MCD intensity is studied using a saturation magnetization experiment conducted over a range of magnetic fields and low temperatures (typically 0−7 T, 2−50 K). This is known as variable-temperature variable-field MCD (VTVH-MCD). In the limit of low temperature or high magnetic field, there is a deviation from Curie law behavior (intensity linear in $1/T$), and at high magnetic fields and low temperature, *C*-term intensity becomes field- and temperature-independent. This corresponds to the case where the Zeeman splitting $g\beta H$ is large relative to k_BT, and only the lowest component of the ground state is Boltzmann populated. This approach to this limit is described by the Brillouin curves shown in Figure 21, which are sensitive to spin state and

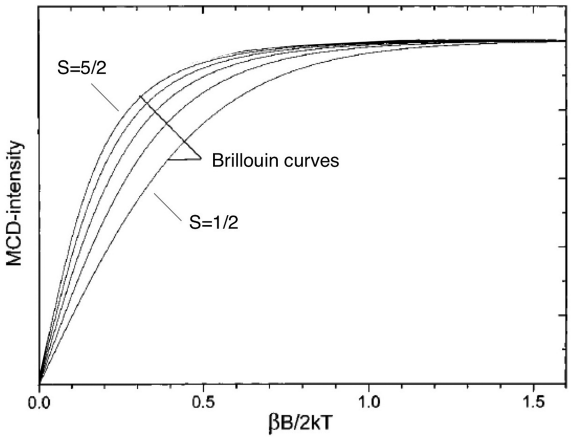

Figure 21. Simulated MCD Brillouin curves for isotropic $S = 1/2-5/2$ ground states. Adapted from ref 122. Copyright 1999 American Chemical Society.

molecular *g*-values, but only depend on H/T. The saturation magnetization MCD of $S > 1/2$ metals is generally more complicated than the behavior shown in Figure 21, however. This is a consequence of ZFS (see section 3.1.1). For systems with axial ZFS ($D \neq 0$), the Zeeman levels of the ground state will be separated in energy in the absence of a magnetic field. Since MCD intensity from a given Zeeman level is proportional to $\langle S_i \rangle$, the spin projection of the level on the axis mutually perpendicular to the two nonzero transition moments (e.g., $\langle S_z \rangle$ for an *xy*-polarized transition), differential Boltzmann population of Zeeman levels with different $\langle S_i \rangle$ leads to nested saturation magnetization isotherms (i.e., nonsuperimposed curves in the H/T plots shown in Figure 22). The magnitude of this effect reflects the magnitude of *D*. For non-Kramers ions, there are additional effects due to rhombic ZFS ($E \neq 0$). For these systems, the ground state, which is an equal mixture of $|+2\rangle$ and $|-2\rangle$ (see bottom of Figure 22) will have a spin expectation value $\langle S_i \rangle = 0$ resulting in no MCD intensity (see section 3.1.1). In the presence of a magnetic field, however, the ground state becomes MCD active through a field-induced mixing of the zero-field split levels.[126] As shown in the bottom right of Figure 22, these become the pure $|+2\rangle$ and $|-2\rangle$ states at high magnetic fields. This results in a nonzero $\langle S_i \rangle$ when the Zeeman interaction becomes large relative to the rhombic splitting (δ in Figure 22, bottom right). Evidence for this is seen in the saturation magnetization isofields of integer-spin metals (Figure 22, middle right), where variation of the ground state wave function with magnetic field leads to magnetic field dependence in the low-temperature (large $1/T$) saturation limit

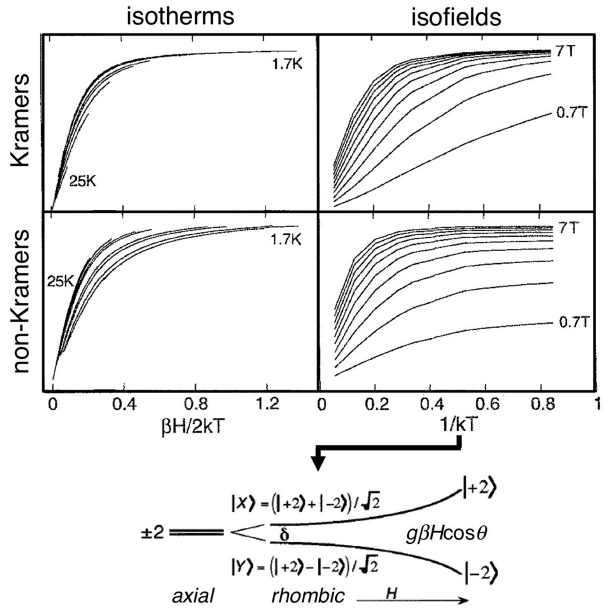

Figure 22. VTVH-MCD saturation magnetization isotherms (left) and isofields (right) for a rhombic $S = 2$ system, including the effects of rhombic ZFS and magnetic field *H* on an $M_s = \pm 2$ non-Kramers doublet (bottom right). Analogous VTVH-MCD data are presented for an $S = 5/2$ Kramers system (middle). The $S = 2$ and $S = 5/2$ isotherms display nesting behavior (i.e., do not overlay) due to differential Boltzmann population of zero-field split levels with different spin expectation values. The $S = 2$ isofields show field dependence in the low temperature saturation limit, reflecting variation of the non-Kramers ground state with field. No such effect is seen in the $S = 5/2$ isofields, reflecting the lack of field dependence in the ground state of Kramers ions.

(Figure 22, bottom right). This effect can be quantified by VTVH-MCD, and then related to the energetic separation δ between the field-mixed Zeeman levels (Figure 22, bottom right). For both Kramers and non-Kramers systems, spin Hamiltonian parameters (see section 3.1.1) are extracted by fitting VTVH-MCD isotherms/isofields.

3.4. Other Spectroscopic Methods with Single-Site Resolution

While site-selective spectroscopy provides the most reliable data on metallozeolite active sites, useful insight is also derived from techniques where features of single sites can be resolved from a mixture. In metallozeolite chemistry, electron paramagnetic resonance spectroscopy and Mössbauer spectroscopy have proved to be particularly useful. Nuclear resonance vibrational spectroscopy also holds significant potential for Fe-zeolites.

3.4.1. Electron Paramagnetic Resonance Spectroscopy. Electron paramagnetic resonance spectroscopy (EPR) is used to probe transitions between Zeeman split sublevels of a paramagnetic ground state.[107,108,110,115] EPR can be used to measure *g*-values and ZFS parameters reflecting the electronic structure of the metal center (see section 3.1.1) with high accuracy. The high energy resolution of EPR also enables detection of small magnetic couplings between unpaired electrons and metal/ligand nuclear spins that are inaccessible using saturation magnetization experiments (e.g., magnetic susceptibility, VTVH-MCD). These hyperfine and superhyperfine interactions provide a direct experimental handle on metal−ligand covalency (see section 3.1.1).

DOI: 10.1021/acs.chemrev.7b00344
Chem. Rev. 2018, 118, 2718−2768

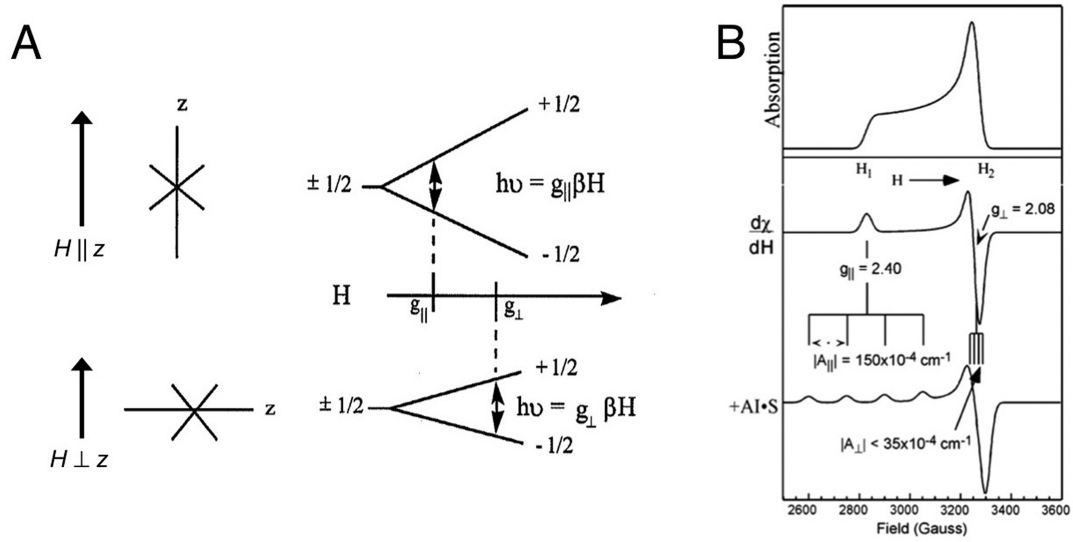

Figure 23. (A) Orientation dependence of the Zeeman splitting of an $S = 1/2$ ground state due to g anisotropy. (B) Simulated EPR absorption spectrum of an axial Cu(II) center (top); its first derivative (middle), including effects from hyperfine coupling to the $I = 3/2$ nuclear spin of Cu (bottom).

In the standard EPR experiment, the sample is irradiated with a fixed microwave frequency (X band, at 9 GHz ≈ 0.3 cm^{-1}) in the presence of a magnetic field oriented perpendicular to the microwave B field. The magnetic field is swept, and microwave radiation is absorbed when the Zeeman splitting between levels with $\Delta M_s = \pm 1$ is brought into resonance with the microwave energy. As shown in Figure 23A, this induces a magnetic dipole transition between Zeeman split levels, and the resonance field associated with this transition is a function of the molecular g-values and the orientation of the molecule with respect to the magnetic field. For a frozen solution or powder, the EPR spectrum is a weighted sum of contributions from all orientations (contribution increasing from ∥ to ⊥, as shown in the top of Figure 23B). Since each orientation is weighted differently, it is possible to measure anisotropic quantities (e.g., g-values and hyperfine couplings) from a randomly oriented sample. High sensitivity is achieved by modulating the external field and using lock-in detection, which leads to a first derivative spectrum. For example, a spin-1/2 system such as Cu(II) will have an absorption spectrum similar to Figure 23B (top), whose first derivative $d\chi/dH$ (Figure 23B, middle) shows distinct features at the resonance fields corresponding to $g_\parallel$ and $g_\perp$.[18] (These deviate from the free electron g-value of 2.0023 due to spin−orbit coupling with ligand field excited states—see section 3.1.1.) Additional features arise due to hyperfine interactions between the unpaired electron spin and the nuclear spin of the metal (see section 3.1.1). For Cu(II), the $S = 1/2$ ground state couples to the $I = 3/2$ nuclear spin of Cu, splitting spectral features into $2I + 1 = 4$ lines (Figure 23B, bottom). The hyperfine splittings of the $g_\parallel$ and $g_\perp$ resonances will in general be different, reflecting the anisotropy of the hyperfine interaction. In some cases, it is also possible to resolve small superhyperfine couplings arising from interactions between the unpaired electron spin and the nuclear spin of ligands (see section 3.1.1). Hyperfine coupling and superhyperfine coupling provide a direct probe of the covalency of the ligand−metal bond. For molecules with $S > 1/2$, the ground state will experience zero-field splitting when the molecule has axial or lower symmetry. This is described by the phenomenological ZFS spin Hamiltonian discussed in section 3.1.1, and

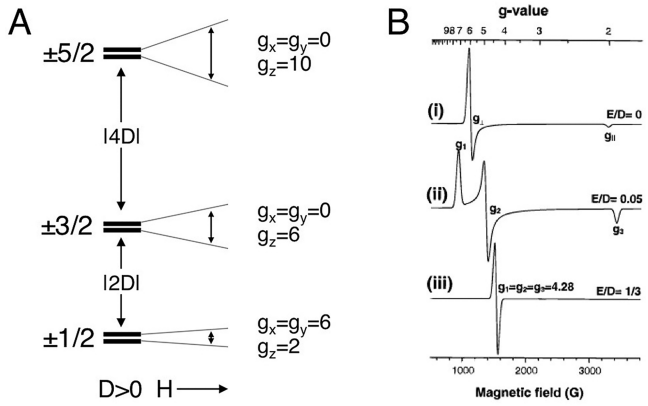

Figure 24. (A) Orientation-dependent response of an axial zero-field split $S = 5/2$ spin to magnetic field applied along the x, y, z directions. (B) Simulated EPR spectra from axial (i, $E/D = 0$), rhombic perturbed (ii, $E/D = 0.06$), and maximally rhombic (iii, $E/D = 1/3$ $S = 5/2$ ground states. The rhombicity parameter E/D is defined based on the zero-field splitting parameters E and D in eq 5. E/D deviates from zero for geometries in which the x and y directions are inequivalent.

characterized by the ZFS parameters E and D introduced in eq 5. In the limit that the zero-field splitting is large relative to the Zeeman splitting ($|D| \gg g\beta H$ for magnetic field strengths used in X-band EPR), the zero-field-split sublevels behave as isolated doublets with unusual effective g-values. For example, for an axial high spin Fe(III) site with molecular g-values $g_\perp = g_\parallel = 2$, the $M_s = \pm 1/2$, $\pm 3/2$, and $\pm 5/2$ Kramers doublets will have anisotropic effective g-values ranging from 0 to 10 (Figure 24A). This significantly impacts the resonance positions observed in EPR for high spin Fe(III) relative to a simple $S = 1/2$ system (Figure 24B). The resonance positions of high spin Fe(III) are also highly sensitive to the presence of rhombic ZFS (Figure 24B), EPR enables direct quantification of rhombicity (E/D), and temperature-dependent studies can be used to assign the sign and magnitude of D.

In contrast to Fe(III), integer spin metals such as high spin Fe(II) are generally inaccessible using the standard X-band EPR experiment. This is because the zero-field splitting between

DOI: 10.1021/acs.chemrev.7b00344
Chem. Rev. 2018, 118, 2718−2768

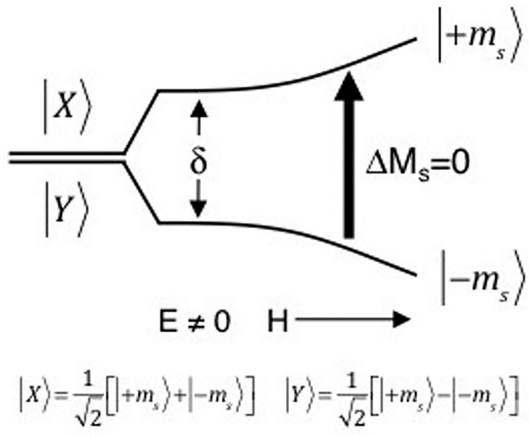

Figure 25. Non-Kramers doublet with rhombic splitting δ smaller than the microwave frequency, enabling detection of the $\Delta M_s = 0$ transition.

levels with $\Delta M_s = \pm 1$ is generally too large to be brought into resonance with the X-band microwave energy (0.3 cm^{-1}). For negative zero-field-split non-Kramers ground states, it is in some cases possible to probe the transition between components of the lowest non-Kramers doublet due to the rhombic mixing of the spin sublevels (Figure 25).[127,128] This is done using parallel-mode EPR, where the B field of the microwave is oriented parallel to the external magnetic field resulting in the selection rule $\Delta M_s = 0$. Note that, while non-Kramers ions are generally difficult to study using EPR, they are amenable to saturation magnetization experiments such as VTVH-MCD (see section 3.3.3).[19,116]

3.4.2. Mössbauer Spectroscopy. Mössbauer spectroscopy is an element-specific technique that probes the resonant absorption of γ photons by Mössbauer-active nuclei.[119] It is most commonly used to study the chemical environment of the ^{57}Fe nucleus, which is sensitive to oxidation state, spin state, and coordination geometry (vide infra). This experiment uses a ^{57}Co source, which decays through electron capture to form a metastable nuclear excited state of ^{57}Fe. The excited ^{57}Fe nucleus subsequently relaxes to its ground state, emitting a 14.4 keV γ ray. This γ ray almost exactly spans the gap between the $I = 1/2$ ground state and metastable $I = 3/2$ nuclear excited state of the ^{57}Fe nucleus (^{57m}Fe, Figure 26A). However, it will not be in exact resonance due to the differing chemical environments of the source and the absorber. The γ ray can be brought into resonance using the Doppler effect, accomplished by varying the velocity of the ^{57}Co source toward or away from the sample (usually over a range of ±10 mm/s, corresponding to Doppler shifts ranging over $\pm 3.87 \times 10^{-3}$ cm^{-1}).

As shown in Figure 26B, the Mössbauer spectrum of an isolated (mononuclear) iron center will generally appear as a doublet of Lorentzian lines. (Additional features arise for slowly relaxing paramagnetic sites, or with the application of an external magnetic field.) The center point of the doublet, δ, is known as the isomer shift. As shown in eq 9, δ reflects the difference in electron density at the nucleus of the absorber $|\Psi_0|^2_A$ versus the source $|\Psi_0|^2_S$, as well as the relative change in nuclear radius upon nuclear excitation ($\partial R/R$):

$$\delta = (\text{const})(\partial R/R)(|\Psi_0|^2_A - |\Psi_0|^2_S) \quad (9)$$

For iron, $\partial R/R$ is negative. A positive δ therefore reflects reduced electron density at the nucleus. Since $|\Psi_0|^2$ derives mostly from electrons in core s orbitals, electrons in valence 3d orbitals affect δ indirectly, decreasing $|\Psi_0|^2$ through shielding effects (mostly from 3s). δ is therefore sensitive to oxidation state and spin state. The Mössbauer transition is generally split into two lines, reflecting the interaction between the electric quadrupole moment of the ^{57m}Fe nuclear excited state with the electric field gradient (EFG) at the nucleus. This interaction splits the $I = 3/2$ excited state into $M_I = \pm 1/2$, $\pm 3/2$ doublets separated by the amount ΔE_Q (Figure 26). The interaction energy, called the quadrupole splitting, will be nonzero for sites with noncubic distributions of electron density:

$$\Delta E_Q = \frac{eQ}{2} V_{zz} \sqrt{1 + \frac{\eta^2}{3}} \quad (10)$$

In this expression, e is the electron charge, Q is the nuclear quadrupole moment (positive for ^{57m}Fe), $\eta = (V_{xx} - V_{yy})/V_{zz}$ is the asymmetry parameter, and the V_{ii} are eigenvalues of the EFG tensor. For sites with cubic molecular symmetry, differential population of the valence 3d orbitals leads to noncubic electron density, and the V_{ii} will become nonzero. This "valence" contribution to ΔE_Q is highly sensitive to oxidation state and spin state, as these affect d orbital occupancy. Deviations from cubic site symmetry lead to an additional "lattice" contribution to ΔE_Q arising from a noncubic distribution of ligand electron density. (While ΔE_Q can be separated into valence and lattice contributions for ionic complexes, this distinction is less meaningful for highly covalent active sites.)

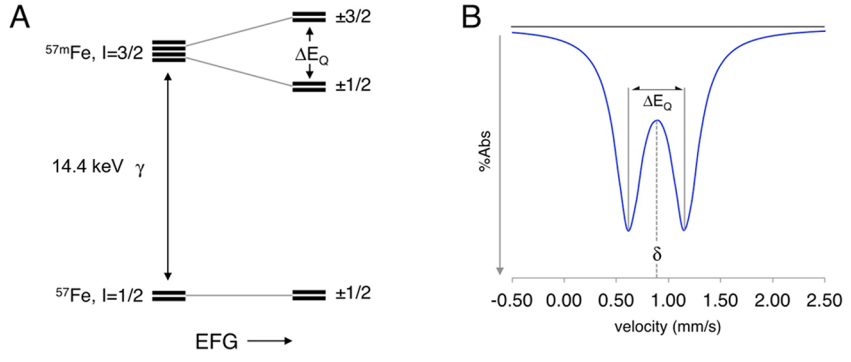

Figure 26. (A) Mössbauer transition, including effects due to a nonzero electric field gradient (EFG) at the ^{57}Fe nucleus ($\Delta E_Q > 0$). (B) Simulated Mössbauer spectral data, with the isomer shift (δ) and quadrupole splitting (ΔE_Q) indicated.

DOI: 10.1021/acs.chemrev.7b00344
Chem. Rev. 2018, 118, 2718−2768

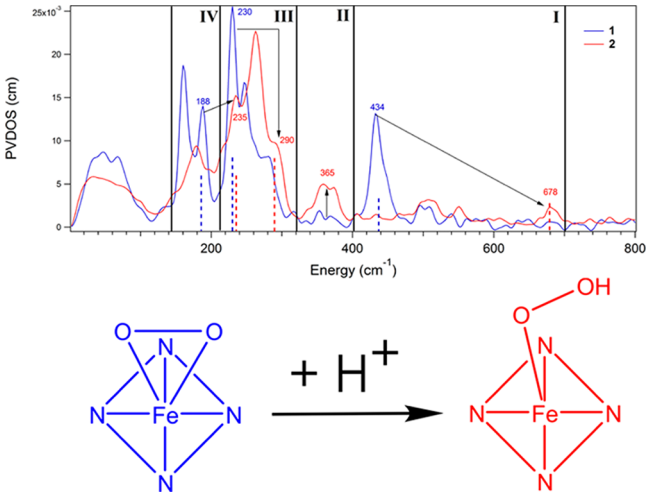

Figure 27. NRVS spectral changes associated with the protonation of the side-on peroxoferric complex $[(TAML)Fe^{III}(OO)]^{+}$ (blue) to form the corresponding end-on hydroperoxide complex (red). Reproduced from ref 240. Copyright 2016 American Chemical Society.

3.4.3. Nuclear Resonance Vibrational Spectroscopy.

Whereas Mössbauer spectroscopy is used to probe resonant absorption by the ^{57}Fe nucleus, nuclear resonance vibrational spectroscopy (NRVS) is a synchrotron-based technique used to study vibrational sidebands of the Mössbauer transition.[129,130] Since NRVS involves inelastic absorption, conservation of momentum dictates the excess linear momentum of the photon be transferred to the absorbing ^{57}Fe nucleus. As a result, vibrations that contain iron motion are active in NRVS, and NRVS intensity correlates to the magnitude of Fe displacement in a particular normal mode at a given energy. NRVS is therefore sensitive to low-energy (150−600 cm^{-1}) core vibrations of Fe active sites.[131−133] These vibrations are highly sensitive to coordination geometry, and can be difficult to resolve using other vibrational techniques such as resonance Raman spectroscopy (sensitive to higher energy vibrations reflecting excited state distortions). NRVS has therefore been used to evaluate structures for intermediates across many mono- and binuclear Fe enzymes and model complexes (see Figure 27, for example). These studies are now being extended to iron active sites in zeolites, and this will provide detailed structural information that is currently inaccessible using other techniques.

4. Cu/O ACTIVE SITES IN ZEOLITES

Cu-zeolites carry out diverse functions ranging from reduction of NO_x pollutants to selective hydrocarbon oxidation using atmospheric O_2. The best-studied system, Cu-ZSM-5, is notable for hydroxylating methane rapidly at low temperatures (150 °C) to form methanol.[36,37] Reactivity occurs at a binuclear extralattice Cu active site, which is activated by either O_2 or N_2O to form the reactive intermediate in methanol synthesis. An experimental approach based on site-selective spectroscopy was developed to distinguish this minority species from 95% spectator Cu, and coupled to DFT, this defined the geometric and electronic structure of the active site and elucidated its reactivity toward strong C−H bonds.[37] These studies were extended to analogous active sites in other lattice topologies—notably Cu-MOR—as well as the precursor intermediates formed during the activation of O_2/N_2O.[66,134−136] Different catalyst preparations are also believed to result in methane-reactive Cu sites with different nuclearities (e.g., trinuclear, mononuclear).[55,74] However, these possibilities have not yet been evaluated using site selective spectroscopy.

4.1. Methane Hydroxylation by Cu-ZSM-5

Activating Cu-ZSM-5 under an atmosphere of either O_2 at 450 °C or N_2O at 150−200 °C leads to the formation of an intense absorption feature centered at 22 700 cm^{-1} (Figure 28A) that decays in the presence of methane (Figure 28B).[36,37] This absorption feature is correlated with the production of methanol, and is therefore a spectroscopic handle of the Cu active site of methanol synthesis.[37] As shown in Figure 28C, the decay of the absorption feature can be used to track the kinetics of methane hydroxylation. This provided an apparent activation energy of 15.7 kcal/mol, and an H/D kinetic isotope effect that is consistent with C−H cleavage in the rate-limiting step (see section 4.2 for details).

The 22 700 cm^{-1} Abs feature was used to selectively probe this active site that exists in a dominant (95%) distribution of spectator Cu.[37] Tuning a laser into the 22 700 cm^{-1} band enabled its study by resonance Raman spectroscopy (Figure 29, inset A). This selectively resonance enhances vibrations of the active site, shown in Figure 29. Work from the Solomon group has defined the characteristic resonance Raman vibrations of all known structures in Cu/O chemistry (Table 5), and these were compared to data from activated Cu-ZSM-5. The active site was originally thought to be a bis-μ-oxo 2Cu(III) species based on the energy of its 22 700 cm^{-1} absorption feature;[36] however this was excluded by rR, as there is is no intense $^{16/18}$O-sensitive vibration at 600 cm^{-1} in Figure 29 (characteristic of a bis-μ-oxo

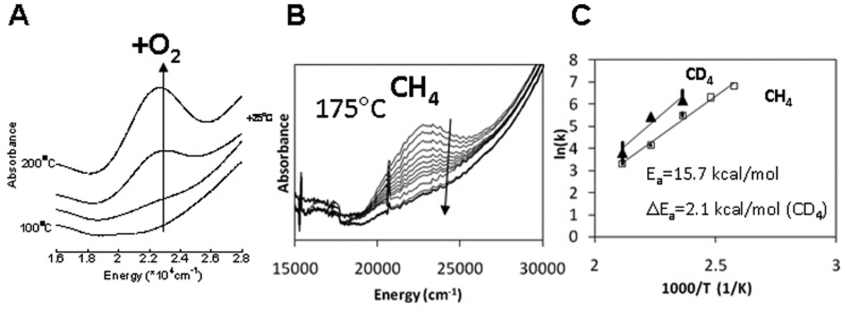

Figure 28. (A) Growth of the 22 700 cm^{-1} absorption feature of the active site during O_2 activation and (B) its subsequent decay upon interaction with methane. (C) Kinetics of methane hydroxylation from decay of the 22 700 cm^{-1} band. Time interval between spectra is 15 s. Adapted with permission from ref 212. Copyright 2011 Royal Society of Chemistry.

DOI: 10.1021/acs.chemrev.7b00344
Chem. Rev. 2018, 118, 2718−2768

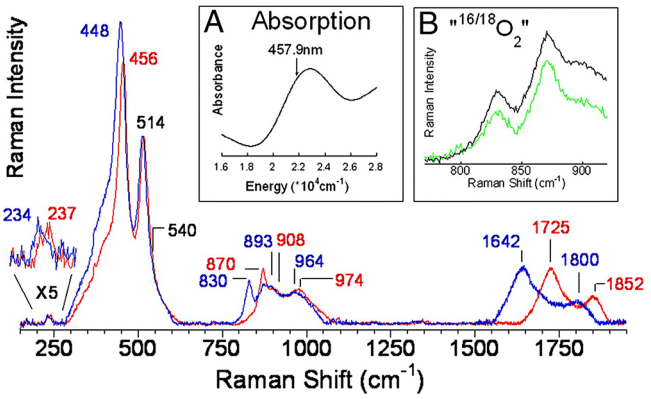

Figure 29. Resonance Raman spectra (λ_{ex} = 458 nm, see inset A) of Cu-ZSM-5 activated with $^{16}O_2$ (red) and $^{18}O_2$ (blue). Inset B shows a comparison of spectra in the 800−900 cm^{-1} region following activation with a 1:2:1 statistical mixture of $^{16}O_2$:$^{16/18}O_2$:$^{18}O_2$ (green) with summed spectra following $^{16}O_2$ and $^{18}O_2$ activation (black). Reproduced with permission from ref 37. Copyright 2009 National Academy of Sciences.

Table 5. Characteristic Resonance Raman Vibrations and Their $^{16/18}$O Isotope Shifts for Known Cu/O Intermediates (Reproduced with permission from ref 37. Copyright 2009 National Academy of Sciences.)

Cu/O_2 species	rR vibrations ($\Delta^{18}O_2$) /cm^{-1}
O_2 activated Cu-ZSM-5	*456 (8)* *870 (40)*
bis(μ-oxo) dicopper(III)	$\nu_{Cu\text{-}O}$=606 (23)
μ-(η^2:η^2) peroxo dicopper(II)	$\nu_{Cu\text{-}Cu}$=284 (0) $\nu_{O\text{-}O}$=763 (40)
η^1-superoxo copper(II)	$\nu_{Cu\text{-}O}$=472 (20) $\nu_{O\text{-}O}$=1121 (63)
η^2-superoxo copper(II)	$\nu_{Cu\text{-}O}$=554 (20) $\nu_{O\text{-}O}$=1043 (59)
η^1-hydroperoxo copper(II)	$\nu_{Cu\text{-}O}$=624 (17) $\nu_{O\text{-}O}$=843 (44)
trans-μ-1,2-peroxo dicopper(II)	$\nu_{Cu\text{-}O}$=561 (26) $\nu_{O\text{-}O}$=832 (44)
μ-1,1-hydroperoxo dicopper(II)	$\nu_{Cu\text{-}O}$=322 (10) $\nu_{O\text{-}O}$=892 (52)

core, Table 5).[137,138] Cu(II) superoxide structures were also excluded due to the absence of an isotope sensitive vibration at ∼1100 cm^{-1} (Table 5).[139,140] On the other hand, the vibration at 870 cm^{-1} with a $^{16/18}$O isotope shift of 40 cm^{-1} in Figure 29 is in the correct range for a Cu/OOH species.[141] To evaluate this possibility, mixed-isotope $^{16/18}O_2$ labeling studies were performed to test for the presence of an O−O bond. Cu-ZSM-5 was activated with a statistical (1:2:1) mixture of $^{16}O_2$/$^{16/18}O_2$/$^{18}O_2$. If an O−O bond were present, vibrations would be observed at 870, ∼845, and 830 cm^{-1} with a 1:2:1 intensity distribution. As shown in Figure 29, inset B (green spectrum), no intermediate frequency mode is observed, indicating that no O−O bond is present in the reactive intermediate.[37] All known structures (Table 5) were therefore excluded for Cu-ZSM-5, indicating the active site was a new species in Cu/O chemistry.

In the rR spectrum of activated Cu-ZSM-5, the most intense isotope sensitive vibration is observed at 456 cm^{-1} ($\Delta^{16/18}$O = 8 cm^{-1}). There is also a weak vibration at 870 cm^{-1} that exhibits a large $^{16/18}$O isotope shift (40 cm^{-1}). Based on frequency and isotope shift, the second quantum of this vibration is seen at 1725 cm^{-1} ($\Delta^{16/18}$O = 83 cm^{-1}), and it is 6 times as intense as the fundamental. The same intensity distribution is seen in mono-μ-oxo bridged diferric sites.[142] This led to the assignment of the active site as a mono-μ-oxo bridged dicopper site. The intense 456 cm^{-1} feature therefore corresponds to the symmetric stretch of the Cu_2O core, while the 870 cm^{-1} feature corresponds to the antisymmetric stretch, which is forbidden in resonance Raman and therefore weak. At higher frequency, the 1725 cm^{-1} feature is the second quantum of the antisymmetric stretch, which is symmetric and therefore rR allowed and intense relative to the fundamental. Finally, based on frequency and isotope shifts, the 1852 cm^{-1} ($\Delta^{16/18}$O = 52 cm^{-1}) feature is assigned as the fourth quantum of the symmetric stretch. This gains intensity through Fermi resonance with the $2\nu_{as}$ feature.

The symmetric and antisymmetric modes of the Cu_2O core are particularly important as they are sensitive to the bridge angle of the three-atom core. A normal coordinate analysis of these modes and their isotope shifts provided an estimated bridge angle of 140° (Figure 30).[37] There is only one location

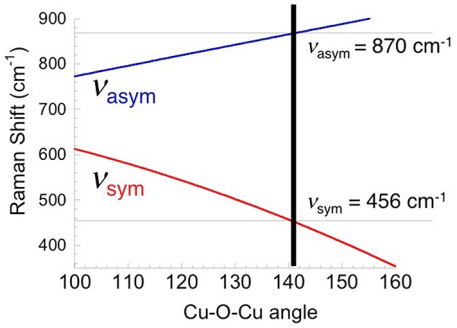

Figure 30. Predicted ν_{sym} and ν_{asym} frequencies as a function of ∠CuOCu.

in the ZSM-5 lattice where (1) Cu is known to bind[143] and (2) a methane-accessible Cu_2O site with a 140° bridge angle can be accommodated. This is the 10-membered-ring motif shown in Figure 31A. Within this ring, there are two aluminum T-sites separated by two silicon T-sites (i.e., an Al−O−Si−O−Si−O−Al sequence) that mediate metal binding. DFT indicates a Cu(III)−O−Cu(III) site is electronically unstable at this site, oxidizing the lattice.[37] On the other hand, this site does stabilize a Cu(II)−O−Cu(II) core with a 139° bridge angle (Figure 31B, versus 140° from experiment) which reproduces the experimental Abs and resonance Raman spectroscopic features of the active site (Figure 31C). In this structure each Cu is three coordinate, bound in a bidentate fashion by two lattice O atoms derived from one Al T-site, as well as the bridging oxo ligand. The lattice modes seen in the experimental rR spectrum at 514/540 cm^{-1} were assigned to the symmetric stretching mode of the bidentate Al T-site ligands. This site is highly covalent, with two electron holes delocalized over the $[Cu_2O]^{2+}$ core. Time-dependent DFT predicts an intense oxo → Cu(II) charge transfer at 23 400 cm^{-1} for the triplet $[Cu_2O]^{2+}$ model—in good agreement with the intense 22 700 cm^{-1} band in Abs spectroscopy. (The singlet and triplet models have nearly identical geometries, energies within 0.5 kcal/mol, and highly similar predicted spectral features.) The low energy and high intensity of this charge transfer band reflect the high covalency of the $[Cu_2O]^{2+}$ core, which is important for reactivity (see sections 4.2 and 6.3.1).[37]

DOI: 10.1021/acs.chemrev.7b00344
Chem. Rev. 2018, 118, 2718−2768

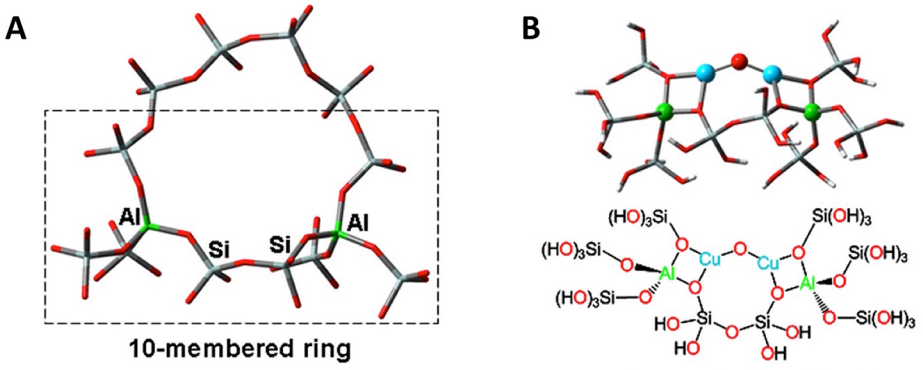

C

	Abs features		rR features			Geometric parameters	
	LMCT	ν_{sym} ($\Delta^{18}O_2$) /cm^{-1}	ν_{asym} ($\Delta^{18}O_2$) /cm^{-1}	$\nu_{lattice}$ ($\Delta^{18}O_2$) /cm^{-1}	<Cu-O-Cu	Cu-O (Å)	Cu-Cu (Å)
experiment	22,700	456 (-8)	870 (-40)	514/540 (0)	140°	-	-
$[Cu_2O]^{2+}$ model	23,400	456 (-5)	852 (-37)	556/568 (0)	139°	1.75/1.76	3.29

Figure 31. (A) Ten-membered ring motif in the ZSM-5 lattice, with the Al−O−Si−O−Si−O−Al sequence implicated in Cu binding highlighted, and (B) the $[Cu_2O]^{2+}$ cluster model derived from this motif. This model was generated by excising the cluster from the lattice in (A), and capping its peripheral oxygen atoms with protons. (C) Comparison of experimental and DFT-predicted $[Cu_2O]^{2+}$ spectral features and geometric structure.

4.2. Reactivity of $[Cu_2O]^{2+}$ Active Sites in Zeolites

The kinetics of methane hydroxylation were evaluated by monitoring the disappearance of the 22 700 cm^{-1} Abs feature in the presence of methane (Figure 28B,C).[37] The reaction was performed at temperatures ranging from 110 to 200 °C, and the resulting Arrhenius plot gave an apparent activation barrier of 15.7 kcal/mol. Performing the same experiment with CD_4 resulted in a 3.1 kcal/mol higher barrier, leading to a large H/D kinetic isotope effect (KIE) of 3.1 at 175 °C—consistent with NMR product analysis of the reaction performed with mixed-isotope substrate (CH_2D_2).

The observation of a large H/D KIE indicates C−H cleavage occurs during the rate-limiting step, and this includes a small activation barrier for the strong, 104 kcal/mol C−H bond of methane. The spectroscopically validated model of the Cu-ZSM-5 active site (vide supra) was used to computationally evaluate the ability of a $[Cu_2O]^{2+}$ core to cleave the C−H bond of methane. On the triplet surface, the $[Cu_2O]^{2+}$ model reacts with methane through H-atom abstraction with a predicted activation barrier of 18.5 kcal/mol (versus 15.7 kcal/mol experimentally—see Figure 32).[37] This produces a mixed-valent $S = 1/2$ $[Cu_2OH]^{2+}$ site coupled to a methyl radical, and the reaction is endothermic by just 13.8 kcal/mol. The 13.8 kcal/mol reaction enthalpy reflects the difference in the strengths of the C−H bond of methane (104 kcal/mol) and the O−H bond of the hydroxo-bridged product. The driving force for forming a strong 90 kcal/mol O−H bond lowers the barrier for H-atom abstraction. The electronic structure of the $[Cu_2O]^{2+}$ core was also found to be intrinsically activated toward H-atom abstraction. In the triplet ground state, the electron holes from each Cu are significantly covalently delocalized onto the bridging oxo. These low-lying unoccupied orbitals therefore have high oxo 2p content, and are good acceptor orbitals for H-atom abstraction. As shown in the top of Figure 32, methane interacts with the singly occupied molecular orbital (SOMO) with oxo 2p character oriented out of the Cu−O−Cu plane. At the transition state geometry, this hole localizes onto the

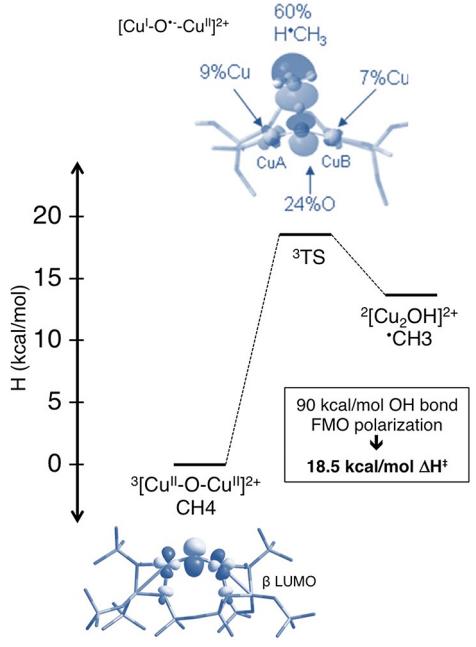

Figure 32. Methane H-atom abstraction reaction coordinate on the triplet surface, highlighting changes in electronic structure that occur at the transition state geometry—in particular, polarization toward $[Cu(I)-O^{\bullet-}-Cu(II)]^{2+}$.

bridging oxo, resulting in a Cu(I)−oxyl-like electronic structure that is highly activated for HAA.[37]

Other Cu-zeolites are known to react with methane at low temperature,[36,66,134] including Cu-MOR, where methane reactivity is also correlated with an absorption feature at ~22 000 cm^{-1}.[36,134] Unlike Cu-ZSM-5, the absorption maximum for Cu-MOR shifts during reaction with methane.[134] This is also seen in spectral changes accompanying desorption of the Cu-MOR active sites at high temperature. In Figure 33, heating Cu-MOR to 450 °C in an atmosphere of O_2 results in loss of an

DOI: 10.1021/acs.chemrev.7b00344
Chem. Rev. 2018, 118, 2718−2768

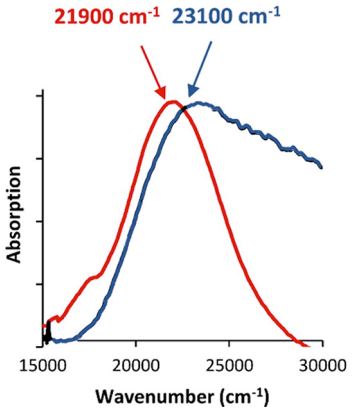

Figure 33. DR-UV–vis difference spectra of activated Cu-MOR showing components lost during heating in O_2 atmosphere at 450 °C (red trace), and then switching to 450 °C He atmosphere (blue trace). Adapted from ref 134. Copyright 2015 American Chemical Society.

Abs feature centered at 21 900 cm^{-1} (red trace). The remaining Abs component centered at 23 100 cm^{-1} (blue trace) decays upon switching from O_2 to He atmosphere (still at 450 °C). This indicates two Cu/O components contribute to the 22 000 cm^{-1} Abs feature, and kinetics studies show these components react with methane at different rates. Two rates are required to fit the Arrhenius plot of the decay of this absorption feature shown in Figure 34. One of these components (MOR 1, red) has reactivity

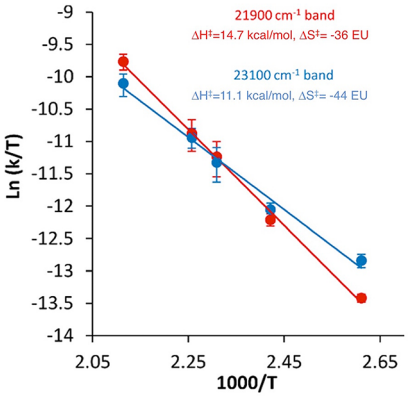

Figure 34. Eyring plot for the decay of the 21 900 (red) and 23 100 cm^{-1} (blue) components of the Cu-MOR Abs feature during reaction with methane. Adapted from ref 134. Copyright 2015 American Chemical Society.

comparable to ZSM-5, while the other (MOR 2, blue) exhibits a significantly lower activation barrier (by 3–4 kcal/mol) and significantly higher entropy of activation (by 8–9 eu). This showed Cu/O active sites with perturbed reactivity exist in Cu-MOR.[134]

Resonance Raman studies summarized in Figure 35 were performed to determine the origin of this difference in reactivity.[134] From data shown in Figure 33, the 22 000 cm^{-1} Abs feature was resolved into two components with absorption maxima at 21 900 and 23 100 associated with MOR 1 and MOR 2, respectively. Tuning a laser into the 22 000 cm^{-1} Abs feature also results in resonance enhancement of vibrations associated with both components. As shown in Figure 35, the rR spectrum of Cu-MOR strongly resembles that of Cu-ZSM-5. However, some features in the Cu-MOR spectrum are clearly split into two components (see marked peaks in Figure 35)—consistent

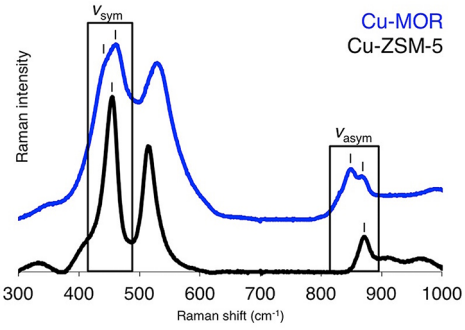

	ZSM-5	MOR 1	MOR 2
Abs feature (cm^{-1})	22,700	21,900	23,100
ν_{sym} (cm^{-1})	456	465	450
ν_{asym} (cm^{-1})	870	850	870
ΔH‡ (kcal/mol)	15.7	14.7	11.1
ΔS‡ (cal/mol•K)	-35	-36	-44

Figure 35. Comparison of rR spectra from Cu-MOR (blue) and Cu-ZSM-5 (black). Peaks corresponding to ν_{sym} and ν_{asym} are indicated, showing two components are present in Cu-MOR. The table summarizes the spectroscopy and reactivity of $[Cu_2O]^{2+}$ cores in Cu-ZSM-5 and Cu-MOR.

with two types of $[Cu_2O]^{2+}$ active sites in Cu-MOR. Since MOR 1 reacts more rapidly at 200 °C (due to the smaller entropic contribution to the Gibbs free energy of activation), it was possible to enrich samples in MOR 2, and this enabled assignment of the rR features of each component. This showed the rR features and Abs features of MOR 1 and MOR 2 are highly similar to each other, as well as to Cu-ZSM-5. Thus, from Abs and rR spectroscopy, the three $[Cu_2O]^{2+}$ active sites have highly similar geometric and electronic structures.[37,134]

The differences in geometric and electronic structure defined experimentally across the $[Cu_2O]^{2+}$ cores in Cu-ZSM-5 and Cu-MOR are too subtle to explain the 25–30% reduction in activation barrier of MOR 2. This indicates there is a contribution to reactivity that does not manifest in the ground state spectral features of MOR 2. The differential reactivity of MOR 2 is therefore ascribed to a second-sphere effect; however, the precise nature of this interaction is not yet understood.[134] This raises a parallel to biology, where for example the coupled binuclear Cu enzymes (i.e., hemocyanin, tyrosinase, catechol oxidase, and NspF) carry out diverse functions ranging from O_2 binding to aromatic hydroxylation using $[Cu_2(O_2)]^{2+}$ intermediates with highly similar geometric and electronic structures (see section 6.3 for details).[18]

4.3. Activation of O_2

The ability of Cu-zeolites to activate atmospheric O_2 for selective oxidation chemistry is highly significant, as this is the most appealing oxidant for industrial scale applications. Reduced Cu(I)-ZSM-5 and Cu(I)-MOR bind and reduce O_2 by four electrons during $[Cu_2O]^{2+}$ formation,[36,37,134] and an oxygen precursor in the $[Cu_2O]^{2+}$ formation reaction has been trapped in Cu-ZSM-5.[136] As shown in Figure 36A, reacting Cu(I)-ZSM-5 with O_2 at room temperature results in formation of an intense absorption feature at 29 000 cm^{-1}. Upon heating, the 29 000 cm^{-1} absorption feature decays with the concomitant growth of the 22 700 cm^{-1} band of the $[Cu_2O]^{2+}$ intermediate (Figure 36B).

Tuning a laser into the 29 000 cm^{-1} Abs band selectively resonance enhances vibrations of the oxygen precursor.[136]

DOI: 10.1021/acs.chemrev.7b00344
Chem. Rev. 2018, 118, 2718–2768

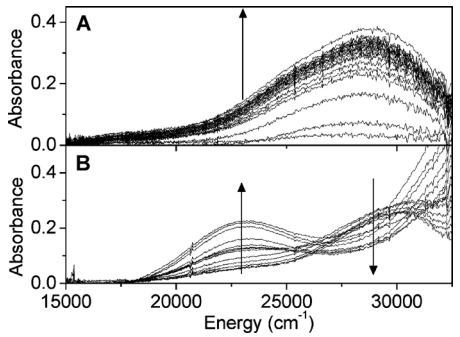

Figure 36. DR-UV−vis spectral changes during O_2 activation of Cu(I)-ZSM-5 (A), and subsequent heating to form $[Cu_2O]^{2+}$ (B). Reproduced from ref 136. Copyright 2010 American Chemical Society.

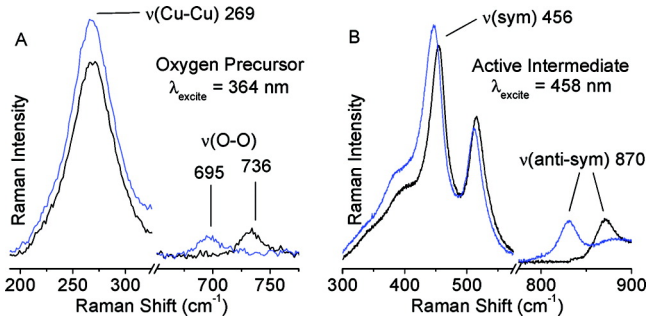

Figure 37. (A) rR data from Cu(I)-ZSM-5 activated at room temperature with $^{16}O_2$ (black) and $^{18}O_2$ (blue), and (B) after heating the oxygen intermediate to form $[Cu_2O]^{2+}$. Reproduced from ref 136. Copyright 2010 American Chemical Society.

The resulting resonance Raman spectrum in Figure 37A (λ_{ex} = 364 nm) shows an intense isotope insensitive vibration at 269 cm^{-1}, as well as a weak feature at 736 cm^{-1} that shifts down by 41 cm^{-1} with $^{18}O_2$. These rR features decay upon heating, and shifting to 458 nm laser excitation, the resonance Raman vibrations of the $[Cu_2O]^{2+}$ intermediate grow in (Figure 37B). The above Abs and 364 nm rR features are therefore correlated with the oxygen intermediate, which converts directly to $[Cu_2O]^{2+}$.

The rR and Abs spectral features of the oxygen precursor in Cu-ZSM-5 are characteristic of μ-η^2:η^2 peroxo-bridged dicopper sites (see Table 5). The 29 000 cm^{-1} Abs band was therefore assigned as an $O_2^{2-}(\pi^*_\sigma \rightarrow Cu(II)$ charge transfer transition, while the 269 and 736 cm^{-1} features in the resonance Raman spectrum are assigned as the Cu−Cu stretching mode and O−O stretch (respectively) of a $[Cu_2(O_2)]^{2+}$ core. $[Cu_2(O_2)]^{2+}$ cores with highly similar spectral features are stabilized in the coupled binuclear Cu enzymes (i.e., hemocyanin, tyrosinase, catechol oxidase, and NspF—discussed in section 6.1).[18]

Spectral changes in Abs and rR that occur upon heating demonstrate this $[Cu_2(O_2)]^{2+}$ site converts directly into the $[Cu_2O]^{2+}$ intermediate.[136] O_2 temperature-programmed-desorption (TPD) studies were performed to clarify the mechanism of this conversion—in particular, the fate of the second O atom of the $[Cu_2(O_2)]^{2+}$ precursor. Heating activated Cu-ZSM-5 leads to desorption of the bridging oxo of the $[Cu_2O]^{2+}$ core, forming the reduced 2Cu(I) active site and releasing O_2. Through microscopic reversibility, the molecular-level details of this process relate directly to the mechanism of O atom loss from the peroxide intermediate. As shown in Figure 38, O_2

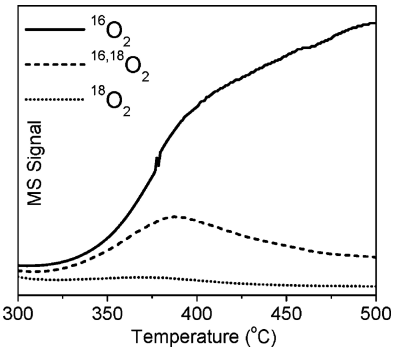

Figure 38. O_2 temperature-programmed desorption quantifying release of O_2 isotopomers during $[Cu_2{}^{18}O]^{2+}$ desorption. Reproduced from ref 136. Copyright 2010 American Chemical Society.

TPD of $^{18}O_2$-activated Cu-ZSM-5 results in release of three isotopomers: $^{16}O_2$, $^{16/18}O_2$, and $^{18}O_2$. Since $^{18}O_2$ activation is known to produce fully labeled $[Cu_2{}^{18}O]^{2+}$, only the $^{16/18}O_2$ and $^{18}O_2$ MS signals reflect desorption of $[Cu_2{}^{18}O]^{2+}$. As the core desorbs between 350 and 420 °C, the ratio of $^{16/18}O_2$:$^{18}O_2$ released is greater than 10:1. This indicates most $[Cu_2{}^{18}O]^{2+}$ recombines with a ^{16}O atom, and not an ^{18}O atom (derived from $[Cu_2(^{18}O_2)]^{2+}$). The isotope scrambling observed in O_2 TPD therefore reflects the ability of the zeolite lattice to act as a reservoir of mobile O atoms.[144−146] This reservoir includes ^{18}O atoms derived from the $[Cu_2(^{18}O_2)]^{2+}$ oxygen precursor, but from experiment the ratio of ^{16}O:^{18}O in this O atom reservoir is greater than 10:1. The ability of the zeolite lattice to accept exogenous atoms is therefore critical to the conversion of $[Cu_2(O_2)]^{2+}$ into $[Cu_2O]^{2+}$.[136]

The conversion of $[Cu_2(O_2)]^{2+}$ into $[Cu_2O]^{2+}$ requires two additional electrons to cleave the O−O bond and liberate O^{2-}. Oxo loss from $[Cu_2(O_2)]^{2+}$ would form a $[Cu(III)_2O]^{4+}$ site that is predicted by DFT to be electronically unstable, oxidizing the zeolite lattice to form $[Cu(II)_2O]^{2+}$.[37] The capacity of the zeolite lattice to serve as an electron donor/acceptor has been established,[147−149] indicating the electron holes generated by $[Cu(II)_2O]^{2+}$ formation can propagate over significant distances to spectator Cu(I) sites. Thus, spectator Cu(I) sites would provide the two exogenous electrons required to cleave the O−O bond to form $[Cu_2O]^{2+}$ during O_2 activation of Cu-zeolites. This has led to the model of active core formation summarized in Figure 39.[136] In this model, O_2 binds to a reduced 2Cu(I) active site, which reduces O_2 by two electrons to form a

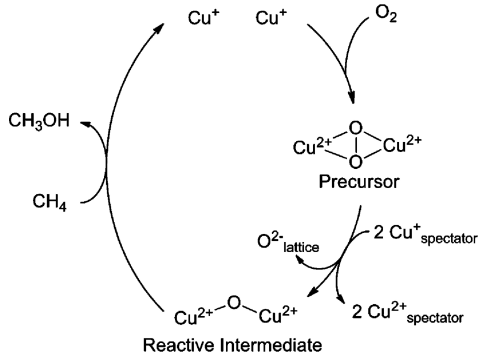

Figure 39. Proposed reaction cycle for O_2 activation and CH_4 hydroxylation by Cu-zeolites. Reproduced from ref 136. Copyright 2010 American Chemical Society.

DOI: 10.1021/acs.chemrev.7b00344
Chem. Rev. 2018, 118, 2718−2768

$[Cu_2(O_2)]^{2+}$ oxygen precursor. Upon heating, spectator Cu(I) centers provide two additional electrons to cleave the O−O bond. This results in formation of the $[Cu_2O]^{2+}$ reactive intermediate, as well as Cu(II) spectator sites, and an oxo that enters the pool of "mobile" lattice O atoms (vide supra). Methane then in principle reduces the active site by two electrons, forming methanol, which is released to return the active site to its reduced 2Cu(I) state. These steps subsequent to H-atom abstraction still need to be explored as does the role of spectator Cu in the conversion of $[Cu_2(O_2)]^{2+}$ to $[Cu_2O]^{2+}$.

Recently, an oxygen intermediate has also been identified in Cu-SSZ-13 using Raman spectroscopy.[150] In this system, O_2 activation is correlated with the appearance of absorption and Raman features characteristic of a μ-1,2-peroxide-bridged 2Cu(II) site (see Table 5). In the same study, Raman and absorption features assigned to a $[Cu_2O]^{2+}$ core with an acute bridge angle of ca. 100 were reported. It will be interesting to evaluate whether this end-on-bridged peroxide intermediate converts to the $[Cu_2O]^{2+}$ core, and once quantitative reactivity data on this acute $[Cu_2O]^{2+}$ site become available, it will be also interesting to see how this change in geometry alters the reactivity of the $[Cu_2O]^{2+}$ core.

4.4. Activation of N_2O

In addition to O_2, the 2Cu(I) active sites of Cu-ZSM-5 and Cu-MOR also activate N_2O, forming $[Cu_2O]^{2+}$ intermediates through O-atom transfer with release of N_2.[37,134,135] In contrast to O−O bond cleavage of O_2, which requires four electrons, only two electrons are required to cleave the N−O bond of N_2O. In this case, the 2Cu(I) active site provides both electrons directly, and exogenous electrons from spectator sites are not required (unlike O_2 activation, vide supra). To define the geometric and electronic structural requirements for N_2O activation by Cu-zeolites, DFT models were constructed of $[Cu_2O]^{2+}$ intermediates stabilized by each of the 10 possible Al−O−Si−O−Si−O−Al sequences in a 10-membered ring of the ZSM-5 lattice (see Figure 31A, right).[135] These all feature three-coordinate Cu(II) centers, each ligated by two lattice oxygen atoms derived from an Al T-site, as well as the bridging oxo ligand. The geometric structures and predicted spectroscopic features (Abs/rR) of the 10 $[Cu_2O]^{2+}$ models are given in Table 6, and these are highly similar across the 10 models. The corresponding 2Cu(I) sites were generated by deleting the bridging O atoms of $[Cu_2O]^{2+}$ cores and geometry optimizing the resulting structures. There is significant variability in the Cu(I) coordination environment across the 10 2Cu(I) models (see Table 6 and Figure 40B), and this leads to a large spread in relative stabilities of the 2Cu(I) sites (>40 kcal/mol, see Figure 40A, left). This is in contrast to the $[Cu_2O]^{2+}$ models, where their similar geometric structures lead to a small spread in relative energies (15 kcal/mol, Figure 40A, right). It was also found that 2Cu(I) sites with approximately linear Cu(I) coordination were found to be the most stable, while two- and three-coordinate Cu(I) structures featuring more acute O−Cu−O angles were destabilized (Figure 40B).[135]

Table 6. Predicted Geometric Structures and Spectroscopic Features of the Ten $[Cu_2O]^{2+}$ and 2Cu(I) Active Sites Stabilized in a 10MR of ZSM-5 (Reproduced from ref 135. Copyright 2014 American Chemical Society.)

	oxidized form ($[Cu_2O]^{2+}$)			reduced form ($Cu^I\cdots Cu^I$)	
	∠Cu−O−Cu (deg)	$\nu_{sym}/\nu_{antisym}$ (cm^{-1})	$CT_{oxo\ to\ Cu}$ (cm^{-1})	binding types	$d_{Cu\cdots Cu}$ (Å)
exp.	**139**	**456/870**	**22 700**	**2 or 3 CN**	**4.43**
site 1	134	445/855	23 159	II,III	4.56
site 2	143	426/857	23 502	II,III	5.03
site 3	146	407/784	21 693	I,I	4.14
site 4	144	417/850	22 280	II,III	5.02
site 5	133	447/859	22 617	I,I	2.48
site 6	**135**	**451/842**	**22 926**	III,III	4.17
site 7	145	415/856	21 300	II,III	5.85
site 8	147	391/860	22 841	I,III	3.54
site 9	145	419/843	21 077	I,III	3.57
site 10	145	408/815	22 897	I,III	4.76

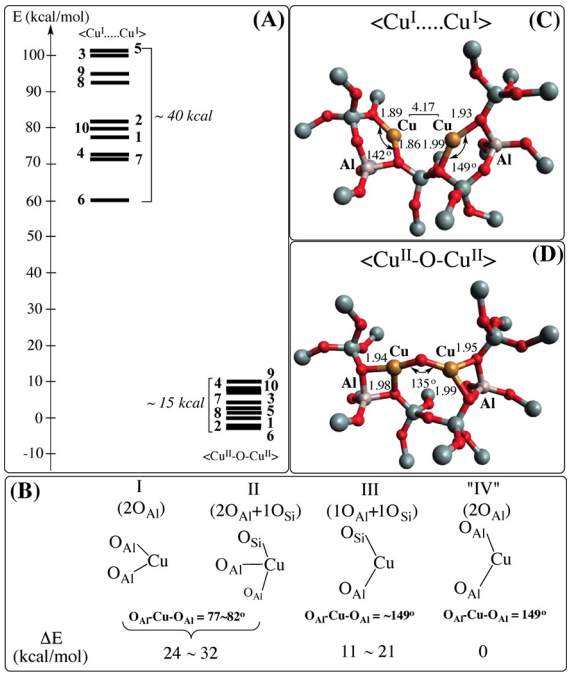

Figure 40. (A) Relative energies of the reduced and oxidized active site DFT models and (B) their Cu(I) coordination modes. Structures of the reduced (C) and oxidized (D) model assigned to the active site seen in experiment. Si atoms are colored dark gray; Al atoms are white. Reproduced from ref 135. Copyright 2014 American Chemical Society.

The most stable $[Cu_2O]^{2+}$ and 2Cu(I) sites (site 6 in Table 6) correspond to the active site discussed in section 4.1, which was initially identified as a candidate structure based on results from X-ray diffraction.[37,135,143] This 2Cu(I) site is at least 12 kcal/mol more stable than the others, and the corresponding $[Cu_2O]^{2+}$ accurately reproduces the spectral features of the reactive intermediate defined experimentally (see section 4.1).[37,135] Based on this, the $[Cu_2O]^{2+}$ site observed experimentally was assigned to site 6, and the reduced and oxidized structures of this site are shown in parts C and D, respectively, of Figure 40.[135] In the reduced site, both Cu(I) centers are bound in an approximately linear fashion by one lattice O atom derived from an Al T-site, and another derived from the neighboring Si T-site (i.e., motif III in Figure 40B). The Cu centers are separated by 4.17 Å, which is sufficiently short to enable bridging required for facile N_2O reduction (vide infra).[135]

The reduced 2Cu(I) active site model was used to evaluate the mechanism of N_2O activation by Cu-ZSM-5.[135] First, the kinetics of N−O cleavage were evaluated experimentally by tracking the growth of the 22 700 cm^{-1} during reaction of Cu(I)-ZSM-5 with N_2O. The resulting Arrhenius plot shown in Figure 41A gave an apparent activation barrier E_a = 2.5 kcal/mol.

DOI: 10.1021/acs.chemrev.7b00344
Chem. Rev. 2018, 118, 2718−2768

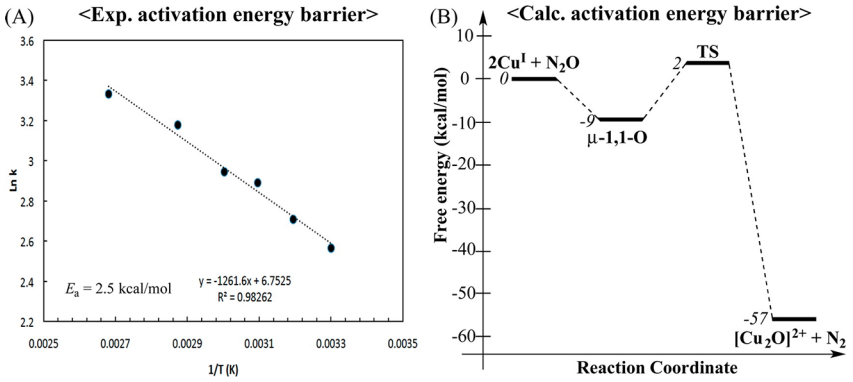

Figure 41. (A) Arrhenius plot for N_2O activation by Cu(I)-ZSM-5 to form $[Cu_2O]^{2+}$ and (B) summary of DFT reaction coordinate for N_2O activation. Reproduced from ref 135. Copyright 2014 American Chemical Society.

	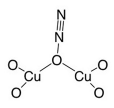	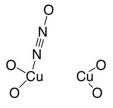	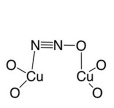
binding modes	μ-1,1-O	η^1-N	μ-1,3-O,N
binding energy[a]	−9	−13	−11
E_a[a]	2	>60	5
N−N−O angle	178	178	173

Figure 42. Binding modes of N_2O, their associated binding energies, and apparent activation energies (E_a) for N−O cleavage. [a]Given in kcal/mol.

Note that this apparent barrier includes the enthalpy of N_2O adsorption, and is therefore reduced from the value for N−O cleavage. As shown in Figure 42, N_2O can bind in three ways to the 2Cu(I) active site. In all cases, N_2O binding is exothermic by 9−13 kcal/mol. While monohaptic binding through the terminal nitrogen to a single Cu(I) center is the most stable, there is no reaction coordinate for O-atom transfer resulting in a $[Cu_2O]^{2+}$ for this intermediate. The μ-1,1-O and μ-1,3-O,N structures in which N_2O bridges adjacent Cu(I) centers, on the other hand, lead to low apparent barriers (2−5 kcal/mol) that are consistent with experiment (2.5 kcal/mol).[135]

The μ-1,1-O intermediate leads to the lowest barrier for N−O cleavage (Figures 41B and 42).[135] As shown in Figure 43A, the transition state for N−O cleavage lies on the singlet surface, with the N−O bond elongated from its equilibrium length of 1.21 to 1.46 Å. At the transition state geometry (shown in Figure 43B), the N−N−O angle is no longer linear, but is instead bent to 143°. The electronic structure associated with this geometry is shown in Figure 43C, where the π^* lowest unoccupied molecular orbital (LUMO) of N_2O is significantly delocalized onto one of the Cu centers. This reflects transfer of a single electron from Cu_1 to N_2O at the transition state. With further N−O elongation past the transition state, the second electron is transferred from Cu_2, completing the reaction and releasing N_2. Two factors contribute to the low barrier for N−O cleavage. First, the 2Cu(I) site has a sufficiently short Cu···Cu separation to enable N_2O to bridge adjacent Cu(I) centers. This geometric structure provides a direct orbital pathway for the sequential two-electron reduction of N_2O, whereby each Cu(I) center donates a single electron to cleave the N−O bond. On the other hand, for longer Cu···Cu distances where N_2O cannot bridge the Cu(I) centers, there is no such orbital pathway for transfer of the second electron and this results in a 14 kcal/mol higher barrier for N−O cleavage.

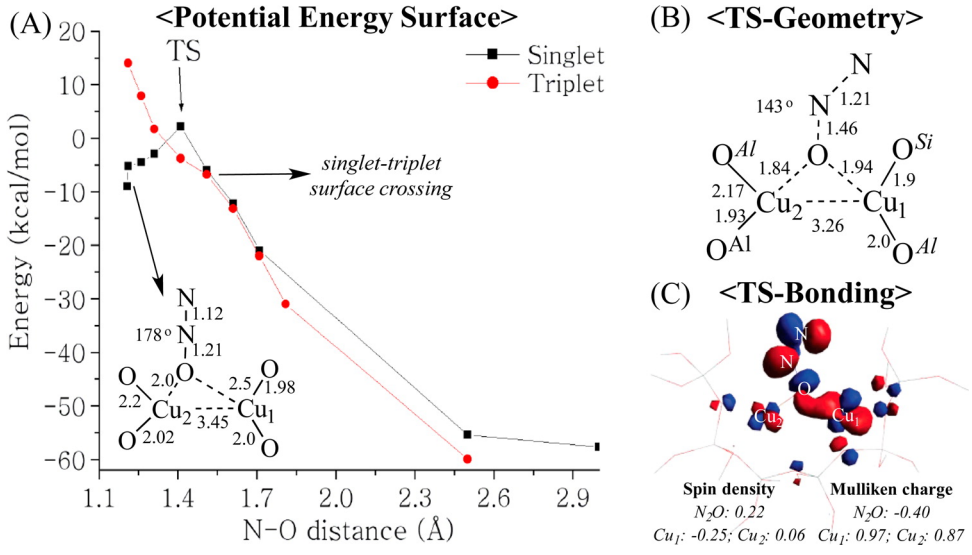

Figure 43. (A) Singlet (black) and triplet (red) potential energy surfaces associated with N−O elongation. (B) Geometric structure of the N−O cleavage transition state, with the associated electronic structure (C) showing delocalization of the N_2O π^* LUMO into the Cu centers of the active site. Reproduced from ref 135. Copyright 2014 American Chemical Society.

DOI: 10.1021/acs.chemrev.7b00344
Chem. Rev. 2018, 118, 2718−2768

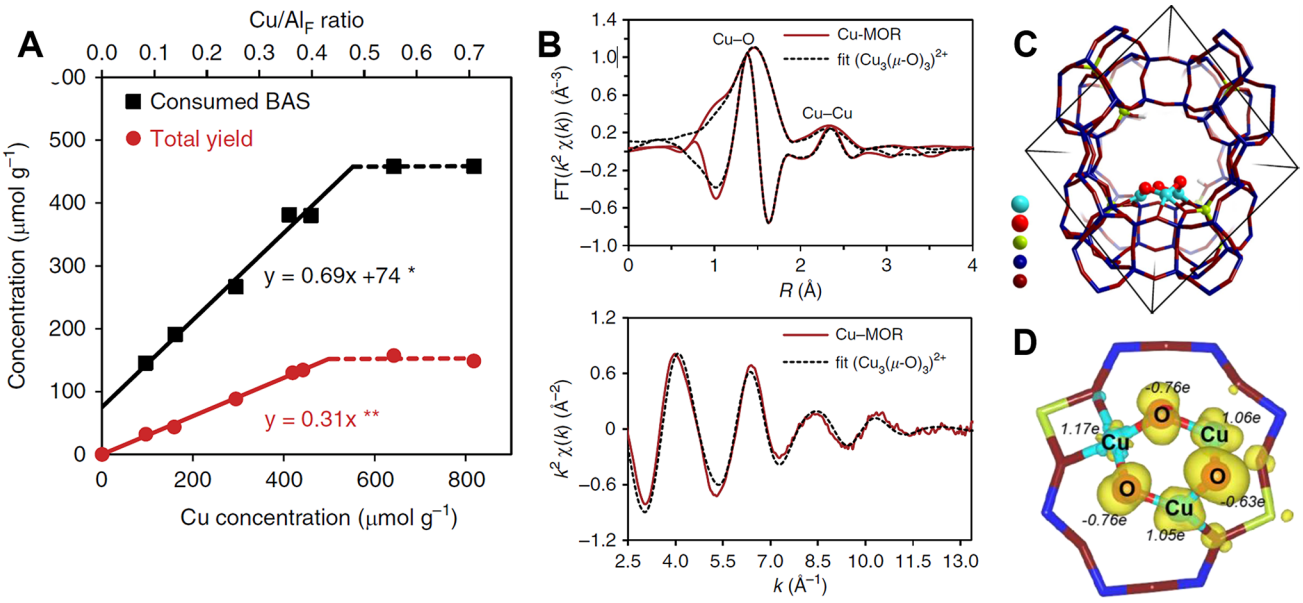

Figure 44. (A) Relation between copper concentration in the MOR zeolite versus consumed BAS and quantity of methane converted into oxygenated products (CO_2, CO, CH_3OH, and $(CH_3)_2O$). (B) Experimental EXAFS spectrum (red) and EXAFS spectrum calculated for the model in (D) (black). (C) Proposed location of the trinuclear copper cluster in the side pocket of the MOR framework. (D) DFT model of the trinuclear copper cluster with Bader charges indicated. Al atoms are in yellow color, Si atoms are in dark blue, and Cu atoms are in light blue.[55] Adapted with permission from ref 55. Copyright 2015 Nature Publishing Group.

Second, the formation of two strong Cu(II)−oxo bonds during O-atom transfer provides the strong driving force for N−O cleavage, tuning down the reaction barrier.[135] In nature, the same reaction is also performed with a low barrier using a multinuclear Cu center—the Cu_Z cluster of nitrous oxide reductase.[151] Parallels and differences between Cu_Z and the Cu(I)-zeolites are discussed in section 6.1.

4.5. Other Cu_xO_y Active Sites of Methane Hydroxylation

Thus far, the $[Cu_2O]^{2+}$ sites in MFI and MOR (vide supra) are the only active Cu−O species identified in zeolites with site selective spectroscopy. However, other reactive Cu−O species of varying nuclearity and with variable activation and reaction constraints have been proposed.[36,66,77,152,153] This is indicated by the extraction of additional methanol after high temperature activation with O_2 or N_2O and methane reaction at ≥473 K, or at elevated pressure, in several copper zeolites (e.g., FER, SSZ-13, SSZ-16, SSZ-39, MOR, ZSM-5, BEA, FAU) and zeotypes (SAPO-34)[66,84,152,154,155] which lack known spectroscopic features. Only recently, anaerobic reoxidation of the active site with H_2O was observed, forming H_2 as a side product.[156] The clarification of the unknown active site structures and reactivity is a work in progress, and an overview will be given in this section. The interest in these active sites is linked to their attractive properties from an engineering point of view. Tomkins et al., for example, detected methanol (up to 55.4 μmol/g) upon steaming of overexchanged Cu-ZSM-5, Cu-MOR, and Cu-Y after O_2 treatment at 200 °C and methane reaction at 200 °C and 36 bar.[155,157] The isothermal conditions of oxidation and methane activation, as well as the consistent yield in subsequent reaction cycles, are promising characteristics for industrial applications.

Influential parameters in obtaining different active sites are the zeolite topology, aluminum distribution and counterbalancing cations, exchange conditions (pH, concentration, salt precursor), and total copper loading. These are discussed in sections 2.2−2.5. Copper speciation is furthermore dependent on environmental conditions, such as temperature and atmosphere composition and pressure.[76] Therefore, operando characterization techniques are imperative for reliable detection of active sites. Often, a multitude of reactive sites is encountered within the same material,[66,152,154] the majority of which lacks site-specific spectroscopy for unambiguous identification of the active sites.

A high spin density localized on the reactive oxygen consistently appears to be crucial in determining the reactivity of Cu active sites in zeolites. Also the stabilization of the oxidized product and confinement effects induced by the zeolite lattice play a role (vide infra). Extralattice oxygen sites with radical character in copper zeolites have already been described by the group of Ismagilov et al. in a 2002 study in the context of NO decomposition.[158] They reported the formation of near-linear copper−oxygen chains in the channels of the MFI zeolite. Upon high temperature vacuum treatment, a distinctive EPR signal ($g_\parallel$ = 2.02, $g_\perp$ = 2.05) lacking typical copper hyperfine splitting is formed and attributed to an anionic oxyl radical $[O^{\bullet-}]$.[159] The origin is proposed to be the autoreduction of linear $[...-Cu^{2+}-O^{2-}-...]$ chains in the zeolite channels to form a new mixed Cu^{2+}/Cu^{+} species with $[...-Cu^{+}-O^{\bullet-}-...]$. An absorption feature at 15 800 cm^{-1} in the vacuum treated sample is linked to $Cu^{2+}-Cu^{+}$ intervalence transitions (IVT) in the partially autoreduced copper oxide linear chains.

4.5.1. Trinuclear $[Cu_3O_3]^{2+}$ Active Sites. The active site of particulate methane monooxygenase is presently defined as binuclear by the X-ray crystallography studies of Rosenzweig et al.[160−162] However, due to challenges involving the instability of the enzyme in preparatory steps prior to analysis, arguments for a trimeric copper oxide cluster are postulated by Chan et al.[163−166] Furthermore, a mononuclear active site resembling that of the lytic polysaccharide monooxygenases is also under consideration.[21] In zeolites, a tricopper oxide species with high reactivity toward methane was recently proposed by Grundner et al.[55]

Single-site tricopper species were synthesized in copper exchanged MOR and ZSM-5[67,79] zeolites by aqueous exchange at a controlled pH of 5.7 followed by activation at 450 °C in O_2

DOI: 10.1021/acs.chemrev.7b00344
Chem. Rev. 2018, 118, 2718−2768

Table 7. Yields of Methanol and Activation Energies for the Stoichiometric Conversion

catalyst	Si/Al	Cu/Al	yield (μmol g^{-1})	E_a (kcal/mol)	ref
CuNaMFI	12	0.58	8.2;[a] 21.7[b]	15.8[c]	36, 37
CuHMFI	14	≤0.67	≤89[d]	15.1[e]	67, 79
CuNaMFI	13.6	0.37	37[f]	–	154
CuHMFI	13.2	0.31	82[f]	–	154
CuNaMOR	8.8	0.43	11.34[a]	MOR 1, 14.7; MOR 2, 11.1[c]	36, 63
CuHMOR	11	≤0.40	≤140[d]	17.7[e]	55, 79

[a]Yield as measured by methanol from liquid phase extraction. [b]Yield as measured by oxidized carbon desorption upon thermal treatment. [c]Experimental apparent activation enthalpy. [d]Yield as measured by total activated methane. [e]Calculated activation energy. [f]Yield as measured by methanol from steam extraction at 483 K, P_{H_2O} = 3.2 kPa.

(section 2.4). A linear 1:3 relation of oxidized CH_4 (calculated from the carbon balance in oxidized products CH_3OH, CO_2, CO, and $(CH_3)_2O$) versus the total copper content and a linear 2:3 ratio of consumed BAS per added copper is observed over a range of copper loadings on Cu-MOR (Figure 44A). This is an indication for a single-site cationic cluster composed of three coppers per two exchanged protons, and is compatible with an extraframework divalent tricopper cluster at a cation exchange site with two nearby lattice Al tetrahedra. A broad absorption band around 31 000 cm^{-1} in the UV−vis spectrum has been linked to the tricopper site in the initial paper reporting the tricopper site, although without computational support. The band was observed to dissipate upon stoichiometric reaction with methane and to reemerge upon reoxidation of the catalyst with O_2.[55]

A structure of the tricopper site was proposed by DFT simulation and is depicted in Figure 44C,D. Formally, the charge on the atoms can be written as [Cu(II), 2Cu(III), 3O(−II)]$^{2+}$ or [3Cu(II), 2O(−I), O(−II)]$^{2+}$. The latter was preferred because it expresses the oxyl character of the extraframework oxygen ions, proposed by Woertink et al. to be necessary in the transition state for methane C−H activation by mono-μ-oxo dicopper.[37] This is also reflected by the spin densities of the calculated structure.[55] The structure assignment is further supported by fitting the experimental Cu K-edge EXAFS spectrum of the material with the simulated spectrum of the $[Cu_3O_3]^{2+}$ (Figure 44B). The EXAFS spectrum below 2 Å can be fitted with two distinct Cu−O metal−ligand bonds, corresponding to the Cu−$O_{Framework}$ and the Cu−$O_{Extraframework}$ bonds.[55,79]

The assignment of the $[Cu_3O_3]^{2+}$ active site was based on sample averaging X-ray techniques and reactivity studies, using the reaction products of methane as a titrant for active site quantification (Figure 44A). This method is reliant on the presence of a single site only. It is worthwhile to note that similar arguments were made in initial attempts to identify the α-Fe site,[88] first identified by Panov et al., as a binuclear iron site. Per contra, thorough spectroscopic investigation recently showed this site to be mononuclear[35] (see section 5). Site selective spectroscopy on the trinuclear cluster would circumvent the necessity of a single site and is required for the full characterization of the $[Cu_3O_3]^{2+}$ cluster in Cu-MOR, Cu-ZSM-5, and other materials. Moreover, no spectroscopic data in support of the absence of any spectator copper are given (e.g., UV−vis, EPR). Additionally, CO_2 and CO were observed in the reaction products, while the oxidation sites required to further oxidize the activated methane species to deeply oxidized CO and CO_2 were not accounted for.

Finally, given the susceptibility of copper speciation to reaction conditions, operando techniques should be employed to ensure that the observed $[Cu_3O_3]^{2+}$ site, if present, is the actual active site at the basis of the catalytic function and not a precursor of, for example, a dinuclear active site formed under reducing CH_4 atmosphere.

4.5.2. Other Cu_nO_x Copper Clusters, $n > 3$. Larger copper oxide clusters, with a nuclearity greater than 3, have also been suggested as reactive sites.[155] These clusters form within the zeolite micropores of overexchanged Cu-zeolites by exchange of aqueous copper hydroxo oligomers with the zeolite Brønsted acid sites (Si(OH)Al) and silanol nests (Si(OH)). This process is influenced by solution pH and the parent material's Si/Al ratio. Alternatively, intraporous copper oxide nanoclusters can be formed during dehydration and calcination of overexchanged copper zeolites via migration and sintering of $CuOH^+$ species (vide supra, section 2.3). In ZSM-5, copper clusters have been detected in the 5.5 Å micropores by N_2 sorption and magnetic susceptibility measurements.[167]

No experimental study has so far demonstrated a conclusive link between methane C−H activation and large ($n > 3$) Cu_nO_x clusters in the zeolitic micropores. Tomkins et al. suggest highly dispersed, subnanometer copper oxide clusters as active sites based on TEM and EXAFS results,[155] and XPS confirms the reduction of a large fraction of the Cu^{2+} in the sample over 13 h of methane reaction at 200 °C at 6 bar. The same oxidized copper clusters may also be active in the catalytic methane to methanol conversion reported by Narsimhan et al.[154] They observe absorption bands at 20 800, 26 800, and 30 000 cm^{-1} during steady-state methanol production with in situ DR-UV−vis spectroscopy, which may be related to subnanoscale copper oxide species. DFT results indicate a positive effect of increased nuclearity on the activation of methane and support the stability of Cu_xO_x, $2 \leq x \leq 5$ species in the 8MR channels of MOR and ZSM-5, with an increase in stability with increasing nuclearity.[54] Verma et al. showed with DFT that Cu_xO_x, $x \leq 8$, clusters can grow from nucleated dimers in the 8MR of CHA.[168] It should be noted that the aluminum atoms in this DFT model are placed on opposite sides of the 8MR. This is unlike the Al−Si−O−Si−O−Al chain in the 8MR, proposed to preferentially stabilize the dinuclear $[Cu_2O]^{2+}$ active site.[37]

4.5.3. Comparative Reactivity of Cu_nO_x Clusters. The mono-μ-oxo dicopper sites and tricopper sites identified on Cu-MFI and Cu-MOR and discussed respectively in sections 4.1 and 4.5.1 require high temperature activation to form a reactive oxygen which abstracts a hydrogen atom from methane at $T \leq$ 200 °C. At this reaction temperature, a strongly chemisorbed product is formed rendering the reaction stoichiometric. At reactivation temperature, the product is thermally decomposed to form CO_2 and H_2O. Yields of methanol upon extraction and apparent activation energies of HAA are given in Table 7 for various materials. Regardless of the existence of a stoichiometric

DOI: 10.1021/acs.chemrev.7b00344
Chem. Rev. 2018, 118, 2718−2768

Table 8. Rates of Methanol Formation in the Catalytic Regime

catalyst	Si/Al	Cu/Al	temp (K)	rate[a] (μmol h^{-1} g^{-1})	E_a^{app} (kcal/mol)	ref
CuNaMFI	13.6	0.37	483	0.88	12.9 ± 1.2	154
CuNaMFI	13.1	0.17	483	0.51	11.2 ± 0.5	154
CuHMFI	14.1	0.38	483	1.51	19.1 ± 0.5	154
CuHMFI	13.9	0.13	483	0.84	21 ± 1.4	154
CuNaMOR	11.4	0.14	483	0.30	22 ± 0.7	154
CuHMOR	11.1	0.14	483	0.84	35.6 ± 0.5	154
CuHMFI	11.5	0.44	543	6 ± 1	–	152
CuNaMOR	5	0.33	543	2 ± 0.1	–	152
CuHMOR	5	0.30	543	10 ± 3	–	152
CuH-SSZ-13	13.8	0.50	483	3.12 ± 0.01	23.9 ± 0.5	154
CuH-SSZ-13	12	0.41	543	28 ± 1	34 ± 7	152

[a]Rate is given in micromoles of methanol desorbed from the catalyst per hour per gram of catalyst at 483 K, P_{H_2O} = 3.2 kPa.

regime, some copper exchanged zeolites perform methane activation under a catalytic regime at T > 200 °C in the presence of CH_4, O_2, and steam, although conversion and selectivity toward methanol remain very low. Active catalysts and their corresponding reaction rates are given in Table 8. The active sites in the catalytic regime are unlikely to be the same as those of the stoichiometric regime, and it has to be investigated whether the di- and trinuclear clusters are stable under reaction conditions above 473 K.

The most reliable apparent activation energies are those determined from the decrease of the LMCT band of the $[Cu_2O]^{2+}$ band around 22 000 cm^{-1} identified on CuNaMOR and CuNaMFI (Figure 35), for which the corresponding mechanism was discussed in section 4.2. For the proposed trinuclear active site only a theoretical activation energy is calculated. The tricopper $[Cu_3(\mu\text{-}O)_3]^{2+}$ active species is expected to hold a substantial radical character on the extraframework oxygen ligands in the ground state, resembling the radical character found in the transition state of the mono-μ-oxo dicopper site. It is proposed that a SOMO mainly consisting of the p orbital of a bridging oxygen ligand cleaves the C−H bond through interaction with the empty antibonding σ^*(CH) orbital with an activation barrier of 17.7 kcal/mol.[55] The proposed orbital interaction is nucleophilic in nature; however, the reaction results in reduction of a bridging oxyl to a hydroxide-level species. This is electrophilic chemistry, consistent with other metal/oxo active sites in zeolites[35,37,134] and other late transition metals.[169] A similar activation energy of 17 kcal/mol was calculated for the hydroxylated $[Cu_3(\mu\text{-}OH)_2(\mu\text{-}O)]$ species.[79] The methyl radical produced in HAA can either form an adsorbed methanol via a rebound[170] of the hydroxyl, bind to another extraframework oxygen, bind to a framework oxygen, or heterolytically bind to one of the coppers in the cluster.[79] An equivalent rebound mechanism was proposed for the mono-μ-oxo dicopper sites.[37]

The data in Tables 7 and 8 reveal two trends. First, at comparable Si/Al and Cu/Al, the methanol yield of the CuH-zeolites exceeds that of the CuNa-zeolites both in the stoichiometric and in the catalytic regime. Second, the apparent activation energies measured for the CuH-zeolites are higher than those for the CuNa-zeolites in the catalytic regime. Two reasons can be advanced to explain the difference in activation energy of CuH-zeolites and CuNa-zeolites: the first is a difference in active site composition and structure; the second is a difference in the siting of the active site in the zeolite structure. In H-zeolites the protons are preferentially located in the most open parts of the zeolitic structures.[81−83] This means that the di- or trinuclear Cu clusters are formed in the more confined parts of the zeolitic structures, where confinement effects more strongly influence the stability of reaction products and transition states. For MOR these are the 8MR side pockets. Analogous to observations on the mono-μ-oxo dicopper in Cu-MOR, a 50% lower methanol yield obtained per copper from CuH-ZSM-5 hosted $[Cu_3(\mu\text{-}O)_3]^{2+}$ active sites compared to that from CuHMOR hosted $[Cu_3(\mu\text{-}O)_3]^{2+}$ was hypothesized to be related to confinement effects.[67] In mordenite, the preferential substitution of Al^{3+} in the 8MR side pocket pore mouth would limit the speciation of $[Cu_3(\mu\text{-}O)_3]^{2+}$ to these specific locations, where confinement effects enable their reactivity and selectivity. In ZSM-5, aluminum pairs can be situated in various zeolite positions, only half of which would sustain $[Cu_3(\mu\text{-}O)_3]^{2+}$ in a suitable environment to enable its reactivity toward methane activation at 200 °C and 1 atm.[67] Periodic DFT calculations on $[Cu_2(\mu\text{-}O)]^{2+}$ sites in MFI and small-pore zeolites CHA, AEI, and AFX further indicate the influence of zeolite confinement on the site geometry and on the activation barrier for methane C−H cleavage.[171]

Expansion of the copper oxide cluster model to $[Cu_4O_4]^{2+}$ and $[Cu_5O_5]^{2+}$ demonstrates a further stabilization of the bound CH_3 and OH fragments resulting from methane HAA with increasing cluster size. It is suggested that larger clusters, with more linkages between copper atoms and extraframework oxygen ligands, can be expected to be more resistant to disturbances caused by the stabilization of reaction intermediates.[54] This does not, however, take into account the energy of the transition state in activating the C−H bond, and therefore cannot be seen as a direct indication for improved active site reactivity. It is possible that reactivity of such sites is enhanced by undercoordinated oxygen species chemisorbed to the cluster upon high temperature oxygen treatment. Such oxygen species attached to the high energy CuO(010) surface of bulk copper oxide were calculated by Varghese et al. to cleave the methane C−H bond with a barrier of only 14.4 kcal/mol in a DFT simulation (Figure 45).[172] In this case, high surface area copper oxide particles, preferably with a large availability of the most active surface face, would be the only requisite regardless of the support material. The zeolite matrix then does not contribute to the intrinsic reactivity of the active site, and its role would be limited to the stabilization of the most active copper phase. All considerations about the reactivity of these copper clusters remain, however, purely computational, and experimental corroboration is needed.

4.5.4. Mononuclear $[Cu(OH)]^+$ Active Sites. Mononuclear copper sites in zeolites are usually considered spectator species in partial methane oxidation, or their role is limited to a cocatalyst effect.[173] With the observation of undefined, water stable active sites in various microporous materials in

DOI: 10.1021/acs.chemrev.7b00344
Chem. Rev. 2018, 118, 2718−2768

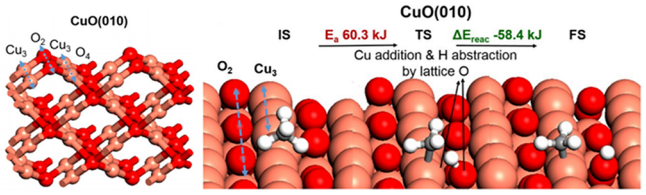

Figure 45. (left) High energy CuO(010) surface of bulk CuO with two-coordinated surface oxygen atoms; (right) DFT model of CH_4 activation over the CuO(010) surface. Reproduced from ref 172. Copyright 2016 Royal Society of Chemistry.

mind,[84,152,154,173] researchers should, however, keep the option open. $[CuOH]^+$ extraframework cations have been experimentally confirmed to be present in Cu-CHA upon high temperature activation in an O_2 atmosphere by the observation of the ν(OH) stretch vibration of $[CuOH]^+$ at 3650 cm^{-1} in Fourier transform infrared spectroscopy (FTIR)[72,76] and have been proposed as active sites in low temperature SCR.[70] The location of $[CuOH]^+$ in the CHA 8MR with a single Al^{3+} substitution was proposed by a combination of experimental (XAS, FTIR, chemical titration) and theoretical DFT work.[71] A $[CuOH]^+$ site has been calculated to be stable in the 8MR of the CHA topology in the presence of moisture, and is predicted to exhibit a reactivity toward methane HAA comparable to the experimental Cu-SSZ-13 catalyst[154] by quantum chemical calculations[74] (E_a = 26.3 kcal/mol by DFT vs E_a^{ap} = 23.9 kcal/mol, Table 8). Likewise, ligated $[CuO]^+$ and $[CuOH]^+$ sites for methane C−H activation have been identified outside of zeolite catalysis,[174−176] and their reactivity and electronic properties have been evaluated with theoretical post-Hartree−Fock and DFT methods.[177] Nevertheless, a conclusive experimental link between $[CuOH]^+$ and methane activation is still lacking.

5. Fe/O ACTIVE SITES IN ZEOLITES

The most widely studied Fe-zeolite, N_2O-activated Fe-ZSM-5, is notable for oxidizing methane to methanol rapidly and selectively at room temperature and pressure.[33,178−180] Fe-zeolites also catalyze the low temperature hydroxylation of benzene to form phenol,[33,94,181,182] and for this reaction, Li and co-workers have identified a spectroscopic intermediate assigned as a ferric phenolate species.[94] Selective hydroxylation of methane and benzene occurs at an extralattice active site called α-Fe(II), which is activated by nitrous oxide to form the reactive intermediate α-O.[181,183] Analogous active sites are stabilized in a number of other lattice topologies.[58,181,182] The geometric and electronic structures of these sites, and factors contributing to their reactivity, were defined recently using VTVH-MCD spectroscopy (see section 3.3) coupled to experimentally validated DFT models—the first application of MCD to distinguishing an active site in a heterogeneous system.[35] These studies showed the exceptional reactivity of α-O derives from a constrained coordination geometry enforced by the rigid zeolite lattice (see sections 5.2.1 and 5.2.2), producing what is referred to in bioinorganic chemistry as an "entatic" state (see section 6.3.3).[35,118] It has also been shown that Fe-ZSM-5 converts methane to methanol using aqueous peroxide at low temperature (see section 5.3).[92] Here, reactivity occurs at active site(s) that are distinct from α-Fe(II)/α-O, but the nature of the active Fe component in this system is unclear.[93,184]

5.1. The α-Fe(II) Active Site

5.1.1. α-Fe(II) Structure. Combined spectroscopic and computational studies of Fe-zeolites have defined α-Fe(II) to be a mononuclear, high spin Fe(II) center with square planar geometry (Figure 46).[35] This extralattice site binds in beta-type 6-membered rings (β-6MR, Figure 46, left),[35] which are present in a number of lattice topologies (notably MFI, *BEA, and FER).[40,185,186] α-Fe(II) binds to the β-6MR through two Al T-sites, each of which binds in a bidentate fashion. Thus, the Fe(II) center is bound to four $_{Al}O_{Si}$ ligands, each carrying a partial negative charge. Other configurations of Al T-sites within the active site fail to reproduce the spectroscopically defined spin Hamiltonian parameters of α-Fe(II) (see section 5.1.2). Currently, no structural data exist for α-Fe(II), although spectroscopically calibrated DFT models predict Fe−O bond lengths of 1.99−2.01 Å for α-Fe(II) in Fe(II)-BEA.[35] In most Fe(II)-zeolites, one face of α-Fe(II) is sterically

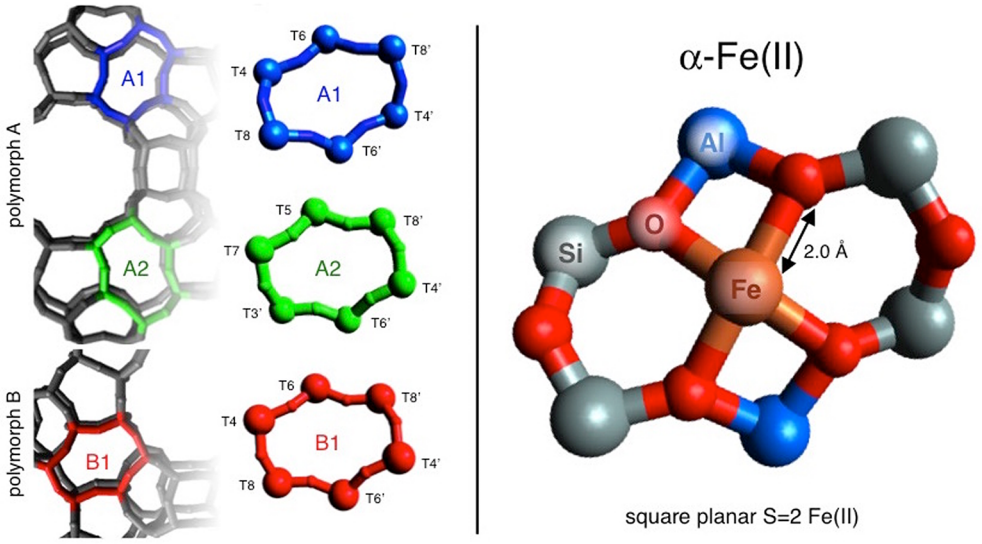

Figure 46. β-6MR motifs in BEA, with T-site labels (left). The predicted structure of α-Fe(II) sited in ring A1 is shown to the right, with Al T-sites at positions T6 and T6′. Adapted with permission from ref 35. Copyright 2016 Nature Publishing Group.

DOI: 10.1021/acs.chemrev.7b00344
Chem. Rev. 2018, 118, 2718−2768

unencumbered, while the other is sterically protected.[185] (An exception is FER, whose β-6MRs are accessible from both faces.[187]) α-Fe(II) therefore has a readily accessible open coordination site that is required for function: accepting an O atom from N_2O to form α-O, the reactive intermediate in selective hydrocarbon oxidation (vide infra).

Based on variations in β-6MR structure, some structural perturbations are expected for α-Fe(II) across different zeolite lattices. The crystal structure of BEA shows three species of β-6MR (Figure 46, left).[186] Rings A1 and A2 are rigorously C_2-symmetric, while ring B1 is slightly perturbed from ideal C_2 symmetry. The T-sites that bind Fe are separated by 5.1−5.6 Å, and the plane defined by the bidentate bite of these T-sites is angled out of the plane defined by the ring. Spectroscopy coupled to DFT shows this leads to rhombic distortions of the active site, resulting in two inequivalent pairs of (*trans*) Fe−O bonds, and an out-of-plane displacement of the Fe(II) center.[35] In the MFI lattice (ZSM-5), the β-6MRs are C_1-symmetric, and also show significant distortions from planarity.[188] In contrast to the BEA and MFI topologies, a single species of D_{2h}-symmetric β-6MR exists in FER.[187] The T-sites that bind Fe(II) are separated by 5.9 Å, and the plane defined by the bidentate bite of these T-sites lies in the plane defined by the ring. The face-to-face separation of neighboring β-6MRs in FER is also relatively short (7.5 Å versus >9 Å in other lattices), and it has been proposed that this allows neighboring α-Fe(II) sites in FER to act cooperatively in the activation of N_2O.[58,189] For FER and MFI, it is not yet understood how these differences in lattice geometry perturb the geometric/electronic structure and reactivity of α-Fe(II).

5.1.2. α-Fe(II) Spectroscopy. Several spectroscopic methods have been used to focus on the reduced α-Fe(II) active site and define its geometric and electronic structure.[35] These studies have defined unique spectral features that reflect the unusual combination of square planar geometry and high spin (S = 2) ferrous electronic structure.[35,190−195] Fe(II)-BEA contains the most extensively characterized α-Fe(II) site, while limited data exist for α-Fe(II) in other zeolite lattices. In DR-UV−vis (Figure 47a, top), α-Fe(II) in Fe(II)-BEA exhibits a single, high energy ligand field band at 15 900 cm^{-1}. As shown in Figure 48, a similar feature is observed in Fe-ZSM-5 and Fe-FER but not Fe-MOR.[35] Based on Abs spectroscopy of structurally defined high spin Fe(II) sites coupled to electronic

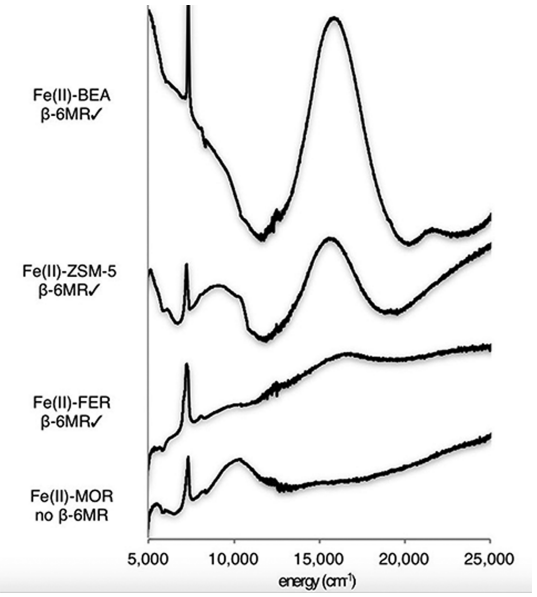

Figure 48. Ligand field spectra of three zeolites known to stabilize α-Fe(II) (BEA, ZSM-5, FER) as well as Fe(II)-MOR, which does not contain α-Fe(II). Adapted with permission from ref 35. Copyright 2016 Nature Publishing Group.

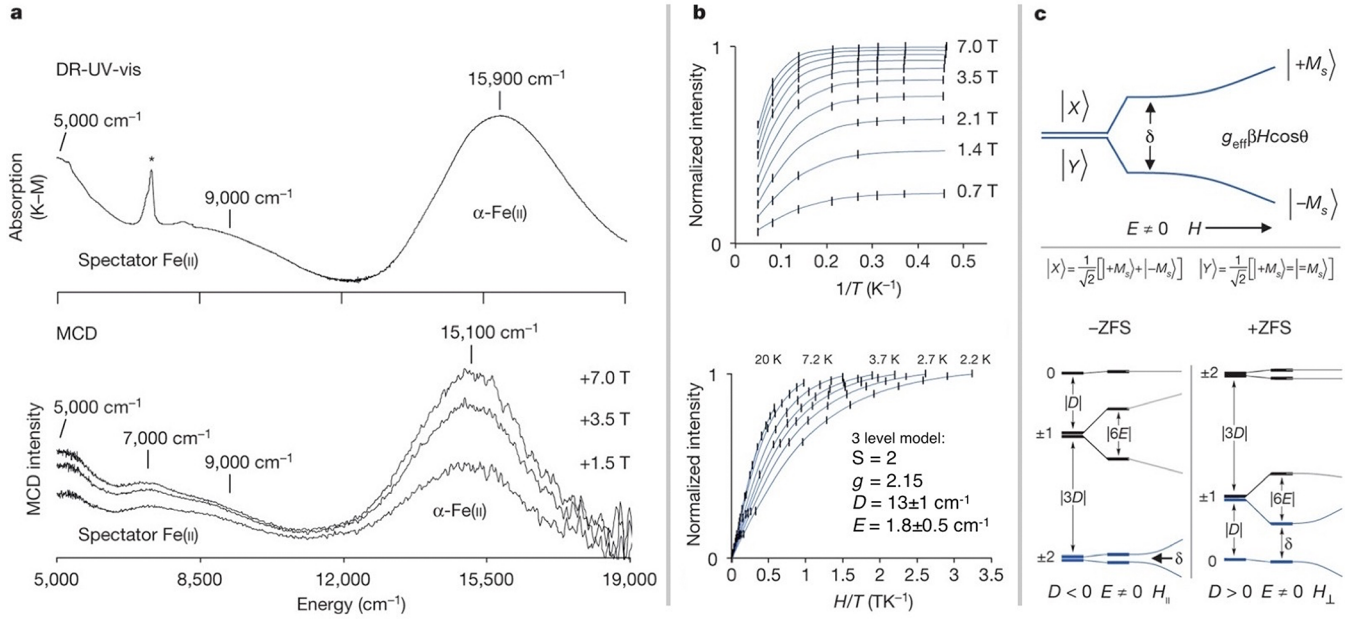

Figure 47. (a) Comparison of 298 K DR-UV−vis data (∗ = OH overtone) and variable-field 3 K MCD data from Fe(II)-BEA (Si/Al = 12, 0.3 wt % Fe). (b) (top) Saturation magnetization isofields for the 15 100 cm^{-1} band of α-Fe(II) (1σ error bars are in black; the fit is in blue). (bottom) Saturation magnetization isotherms for α-Fe(II) (fit in blue), including best-fit spin Hamiltonian parameters. (c) (top) Effects of rhombic ZFS (δ) and external magnetic field on a non-Kramers doublet. (bottom) Comparison of +ZFS and −ZFS S = 2 spin manifolds, including effects due to axial ($D \neq 0$) and rhombic ($E \neq 0$) ZFS. Levels identified with the non-Kramers doublet model shown in the top of the figure are highlighted in blue. Adapted with permission from ref 35. Copyright 2016 Nature Publishing Group.

DOI: 10.1021/acs.chemrev.7b00344
Chem. Rev. 2018, 118, 2718−2768

structure calculations, the red band of α-Fe(II) was assigned as the $3d_{z^2} \rightarrow 3d_{x^2-y^2}$ ligand field transition of a square planar site.[35,190,193,195] The high energy of this transition reflects the axial/equatorial anisotropy of the ligand field provided by the β-6MR, as well as the unique stability of $3d_{z^2}$ in square planar geometry brought about by $3d_{z^2}$/4s mixing in the absence of axial ligands. DR-UV−vis bands at lower energy (<12 000 cm^{-1}) are also present in Fe(II)-zeolites, but these are assigned as ligand field bands of spectator Fe(II) sites.[35]

In low-temperature MCD (Figure 47a, bottom), the $3d_{z^2} \rightarrow 3d_{x^2-y^2}$ transition of α-Fe(II) in Fe(II)-BEA appears as a positive band at 15 100 cm^{-1}.[35] This feature is sensitive to both temperature and field due to the paramagnetic ground state of α-Fe(II). It gains intensity through what is formally a temperature-dependent ***B***-term mechanism (see section 3.3.2), as is evident from VTVH-MCD isofields from the $3d_{z^2} \rightarrow 3d_{x^2-y^2}$ transition (Figure 47b, top), which show field dependence in the low-temperature saturation limit. This reflects changes to the ground state wave function brought about by field-induced mixing of Zeeman sublevels—a characteristic behavior of non-Kramers (integer spin) systems.[113,116] At zero field, a non-Kramers doublet ground state is split by the amount δ due to rhombic ZFS (Figure 47c, top). The $\pm M_s$ wave functions also mix equally, forming linear combinations $|X\rangle$ and $|Y\rangle$. The levels undergo an additional Zeeman splitting in the presence of a magnetic field, and the pure $|-M_s\rangle$ and $|+M_s\rangle$ states are recovered in high fields (Figure 47c, top). A g_{eff} = 8.6 indicates α-Fe(II) is an S = 2 system, and a large δ = 9.0 cm^{-1} indicates this is a positive zero-field-split system (see Figure 47c, bottom). VTVH-MCD isotherms from the 15 100 cm^{-1} transition (Figure 47b, bottom) are highly nested due to a large and positively signed axial zero-field splitting (D = 13 ± 1 cm^{-1}) of the S = 2 ground state of α-Fe(II).[35] This large positive D—a characteristic of high spin square planar Fe(II)—is a consequence of spin−orbit coupling between the d_{z^2} ground state and low-lying d_{xz}/d_{yz} ligand field excited states. VTVH-MCD data also indicate a rhombic site distortion (E/D = 0.14) of α-Fe(II) due to deviations from ideal square-planar geometry (see section 6.2).

In room-temperature Mössbauer spectroscopy (Figure 49), α-Fe(II) in Fe(II)-BEA exhibits a single quadrupole-split doublet

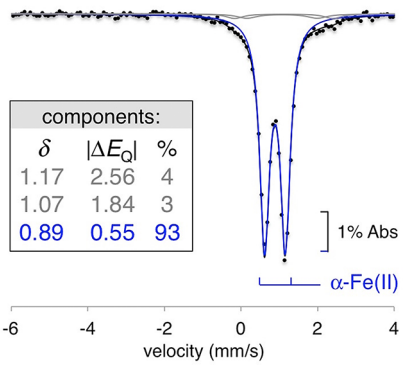

Figure 49. The 300 K Mössbauer spectrum of Fe(II)-BEA (Si/Al = 12, 0.3 wt % Fe), with the α-Fe(II) doublet shown in blue. Adapted with permission from ref 35. Copyright 2016 Nature Publishing Group.

with an isomer shift of ca. δ = 0.89 mm/s and quadrupole splitting $|\Delta E_Q|$ = 0.55.[35] Similar features have been reported for Fe(II)-FER (δ = 0.94 mm/s, $|\Delta E_Q|$ = 0.69 mm/s) and Fe(II)-ZSM-5 (δ = 0.89 mm/s, $|\Delta E_Q|$ = 0.74 mm/s), but at the time these were not assigned to α-Fe(II).[180] These are unusually small quadrupole splittings for S = 2 ferrous sites, where $|\Delta E_Q|$ typically exceeds 1.5 mm/s. For S = 2 square planar Fe(II) sites, however, an equatorial distribution of ligand electron density together with an axial distribution of d electron density due to a doubly occupied $3d_{z^2}$ orbital (see section 3.1.2) leads to near-cancellation of large, oppositely signed lattice and valence contributions (respectively) to ΔE_Q.[194]

5.1.3. Reactivity of α-Fe(II). Studies of the reactivity of α-Fe(II) are currently limited to its role in O-atom transfer from N_2O.[58,189] In this reaction, α-Fe(II) donates two electrons to cleave the N−O bond of N_2O, releasing N_2 and forming α-O. This occurs rapidly at moderate temperatures (e.g., 200 C), with an apparent activation enthalpy of 10 kcal/mol in Fe-ZSM-5.[32] Similar reactivity is observed for Fe(II)-BEA.[58,189] Fe(II)-FER has improved reactivity relative to other Fe(II)-zeolites (vide infra).[58,189] Molecular-level insight into the activation of N_2O by α-Fe(II) is lacking; however, two general factors enabling rapid N_2O reduction have been defined in studies of Cu-zeolites (Cu-ZSM-5) and the Cu_Z cluster of N_2OR.[135,151] First, N_2O must bind to the active site with a geometry that facilitates the transfer of two electrons required to cleave the N−O bond. (Unlike the multinuclear Cu active sites of N_2O reduction, however, the mononuclear α-Fe(II) active site can reduce N_2O by two electrons without the participation of a second metal center.) Second, the formation of a strong metal−oxo/hydroxo bond in the oxidized product creates a large driving force for O-atom transfer.

The thermodynamics of N_2O reduction have been explored computationally for α-Fe(II) sites in Fe(II)-FER.[189] N_2O can bind to α-Fe(II) terminally by either the O or N atom, forming a square pyramidal intermediate. The N-bound sites are predicted to be more stable (8−12 kcal/mol binding energy versus 6−9 kcal/mol for O binding), but are unproductive in O-atom transfer. The O-bound intermediates feature axial Fe−O bond lengths of 2.16−2.26 Å, bent Fe−O−N angles (ca. 120−130°), and minimal changes to O−N and N−N bond lengths. The predicted electronic structure of this intermediate was not discussed. The transition state for O-atom transfer lies 18−19 kcal/mol above the ground state, translating to an apparent activation enthalpy of 9−13 kcal/mol. This agrees well with the value from Fe(II)-ZSM-5;[32] however, no experimental kinetic parameters exist for N_2O activation by Fe(II)-FER. Electronic structure contributions to N−O cleavage also have not yet been defined, and the strength of the product iron−oxo bond has not been evaluated (however, see section 5.2). The geometry of the FER lattice is unique in that it may allow neighboring α-Fe(II) sites to act cooperatively in N_2O reduction. This has been proposed as an explanation for the ~3-fold enhancement of rate in N_2O reduction for Fe(II)-FER relative to Fe-BEA and Fe-ZSM-5 (at 230 °C).[58,189] In this scheme, N_2O forms a μ-1,3-O,N bridge between adjacent α-Fe(II) centers. The apparent barrier for O-atom transfer calculated for this bridged intermediate is 3−4 kcal/mol (versus 9−13 kcal/mol for the mononuclear site). No explanation is provided for how N_2O bridging tunes down the barrier, however, and no experimental kinetics data exist for comparison.

While the N_2O reactivity of Fe-zeolites has been studied extensively, it is currently accepted that O_2 does not function in O-atom transfer to α-Fe(II).[32,183] (O_2 may react with sites distinct from α-Fe(II), however.[95]) This is in contrast to the Cu-zeolites, where O_2 does transfer an O atom to the 2Cu(I)

DOI: 10.1021/acs.chemrev.7b00344
Chem. Rev. 2018, 118, 2718−2768

active sites of Cu-ZSM-5 and Cu-MOR (see section 4.3).[37,134,136] A key intermediate step to O-atom transfer in the Cu-zeolites is reduction of O_2 by two electrons to form a peroxy-level $[Cu_2(O_2)]^{2+}$ intermediate.[136] In this case, the Cu(I) centers are oxidized by one electron, meaning two electrons can be readily transferred to O_2 without the formation of a strong metal−oxo bond. (This is in contrast to the reduction of N_2O, where Fe(IV)−oxo or $Cu(II)_2$−oxo bond formation drives electron transfer.) The ability of α-Fe(II) to transfer two electrons to O_2 has not yet been evaluated. Many mononuclear non-heme Fe(II) centers that bind O_2 exist in biology and model chemistry, but in the absence of exogenous electrons these generally activate O_2 at the superoxy level, and do not go on to form stable peroxo−Fe(IV) species. Whether α-Fe(II) fits with this trend remains to be experimentally evaluated.

5.2. The α-O Reactive Intermediate

5.2.1. α-O Structure. Combined spectroscopic and computational studies of N_2O-activated Fe-zeolties have defined α-O to be a mononuclear, high spin ($S = 2$) Fe(IV)═O species (Figure 50).[35] In this square pyramidal site, equatorial ligation

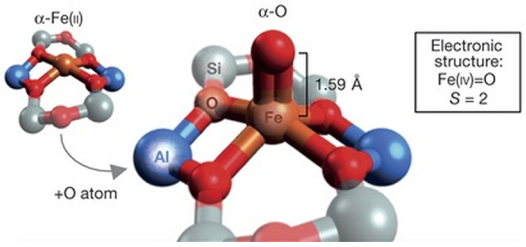

Figure 50. DFT-predicted structure of α-O in Fe-BEA. Adapted with permission from ref 35. Copyright 2016 Nature Publishing Group.

is provided by the β-6MR. The oxo ligand occupies the axial position of the exposed face of the active site, and is thus readily accessible to substrates as large as benzene. Spectroscopically calibrated DFT models of α-O in Fe-BEA predict equatorial $Fe-O_{lattice}$ bond lengths of 2.00−2.02 Å, which are highly similar to the $Fe-O_{lattice}$ bonds of α-Fe(II). The Fe═O bond is predicted to be short (1.59 Å) and highly covalent due to the absence of a *trans* axial ligand. A similar geometric structure has been predicted for α-O in Fe-ZSM-5.[178] Currently, no structural data exist for α-O in any zeolite lattice, however.

α-O is the first $S = 2$ Fe(IV)═O site with axial square pyramidal geometry to be identified. This geometry is inherently unstable for a high spin d^4 site with a single strongly bound ligand (oxo) and four weak ligands (lattice O).[196,197] As shown in Figure 51, shifting an equatorial lattice O ligand to the vacant *trans* axial position would exchange a destabilizing equatorial σ-antibonding interaction (occupied σ^* $d_{x^2-y^2}$) for a stabilizing axial σ-bonding interaction (vacant σ^* d_{z^2}), resulting in stronger bonding between the Fe(IV) and the zeolite lattice. The strong ligand therefore prefers to bind in the equatorial plane. This creates a driving force for geometric distortion (ca. 6 kcal/mol by DFT) toward square pyramidal geometry with the oxo ligand in the equatorial plane.[35] The role of the zeolite lattice is therefore 2-fold. First, the weak equatorial ligand field provided by the zeolite lattice stabilizes the $S = 2$ Fe(IV)═O electronic structure of α-O. The rigid β-6MR then opposes the distorting force associated with this electronic structure, enforcing the vacant *trans* axial position that is key to function. This defines an entatic state for α-O, whereby rigid lattice

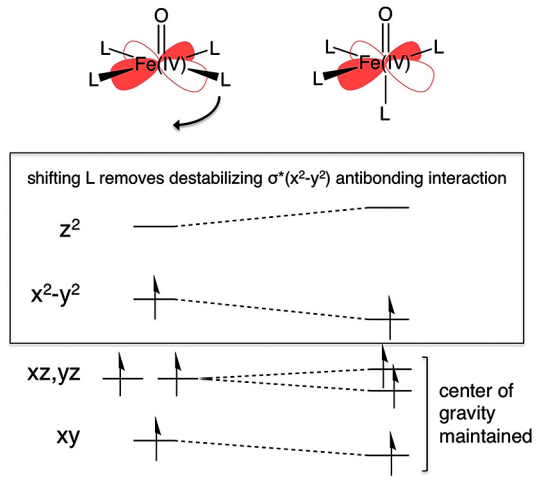

Figure 51. Walsh diagram illustrating the ligand field origin of the distorting force experienced by an axial square pyramidal $S = 2$ Fe(IV)═O site (left) toward an equatorial square pyramidal structure (right).

constraints maintain an electronic structure that is associated with high reactivity (see section 6.3.3 for details).

5.2.2. α-O Spectroscopy. α-O has been studied in detail by DR-UV−vis, MCD, VTVH-MCD, and Mössbauer spectroscopy.[35] Fe(II)-BEA contains the most extensively characterized α-O site, but some data also exist on α-O in Fe-ZSM-5 (including DR-UV−vis and resonance Raman).[94] These studies have defined unique spectral features that reflect the ($S = 2$) ferryl oxo electronic structure of α-O. In DR-UV−vis (Figure 52, top), α-O in Fe-BEA exhibits three absorption features below 22 000 cm^{-1}. The shoulder of a weak, low energy feature is seen between 5000 and 9000 cm^{-1}. At higher energy, there is a more intense 16 900 cm^{-1} band with a high energy shoulder at ~20 000 cm^{-1}. A similar absorption band is seen in N_2O-activated Fe-ZSM-5 at 16 500 cm^{-1}, but this feature has not yet been correlated to α-O through methane reactivity.[94] In Raman spectroscopy of Fe-ZSM-5 (ν_{ex} = 16 500 cm^{-1}), a feature at 867 cm^{-1} is observed that is not present before N_2O activation, and decays in the presence of benzene. This feature has been assigned to α-O, but is misattributed as the O−O stretch of a binuclear oxo/peroxo-bridged diferric site.[94] The $^{16/18}O$ sensitivity of the 867 cm^{-1} vibration feature has also not been evaluated, and it has not yet been shown to be in resonance with the 16 500 cm^{-1} absorption band of α-O.

In low temperature MCD (Figure 52, middle), the lowest energy absorption band of α-O in Fe-BEA appears as a weak negative feature in the 5000−9000 cm^{-1} region with fine structure.[35] For mononuclear non-heme $S = 2$ Fe(IV)═O sites, the lowest energy MCD features are the $d_\pi \rightarrow d_{z^2}$ ligand field excited states, which show fine structure due to vibronic progressions in the Fe−O stretch.[198,199] However, these transitions generally occur at energies >12 000 cm^{-1}. The low energy of the α-O band may result from the stability of d_{z^2} in the absence of a *trans* axial ligand, reflecting the entatic geometry of the active site. This possibility has not yet been evaluated. At higher energy, there is a positive band at 20 100 cm^{-1} with a low-energy shoulder at ca. 16 900 cm^{-1}. These MCD bands correspond to the DR-UV−vis features at 16 900 and ~20 000 cm^{-1}, but with an inverted intensity ratio.

Like α-Fe(II), the MCD features of α-O are temperature-dependent nonlinear ***B***-terms (see sections 5.1.2 and 3.3.2).[35,116]

DOI: 10.1021/acs.chemrev.7b00344
Chem. Rev. 2018, 118, 2718−2768

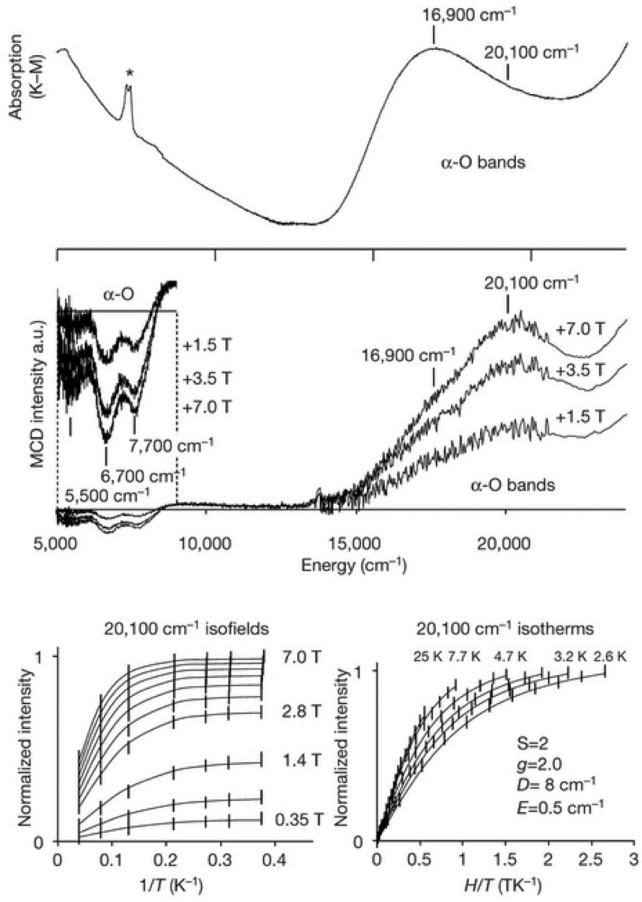

Figure 52. Comparison of 298 K DR-UV−vis data (top, ∗ = OH overtone) and variable-field 3 K MCD data (middle) from N_2O-activated Fe-BEA (Si/Al = 12, 0.3 wt % Fe), along with saturation magnetization isofields for the 20 100 cm^{-1} band of α-O (bottom left, 1σ error bars are in black; the fit is in blue) and saturation magnetization isotherms for α-Fe(II) (bottom right, fit in blue) with best-fit spin Hamiltonian parameters. Adapted with permission from ref 35. Copyright 2016 Nature Publishing Group.

This is evident from field dependence in the low-temperature saturation limit of VTVH-MCD isofields for the 20 100 cm^{-1} transition shown in the bottom left of Figure 52. VTVH-MCD isotherms (Figure 52, bottom right) are nested due to the positively signed axial zero-field splitting (D = 8 ± 1 cm^{-1}) of the S = 2 ground state of α-O. This value of D is comparable to other S = 2 mononuclear Fe(IV)═O sites, where spin−orbit coupling to low-lying triplet excited states contributes dominantly to the zero-field splitting.[200] Importantly, VTVH-MCD indicates α-O is not an Fe(III)−$O^{\bullet-}$ species as has been proposed extensively in the literature, as D = 8 ± 1 cm^{-1} is well outside the range possible for this electronic structure (D < 2 cm^{-1}).[19,109]

5.2.3. Reactivity of α-O. α-O is remarkable for its ability to hydroxylate the strong, unactivated C−H bonds of methane and benzene rapidly at room temperature, making α-O one of the most reactive metal−oxo sites known. Due to the extreme reactivity of α-O, no experimental estimates of activation barriers for selective hydrocarbon oxidation currently exist. The barriers for methane hydroxylation here are significantly lower than those observed for the Cu-zeolites ($\Delta H^{\ddagger}$ = 11−16 kcal/mol—see section 4.2), which react only sluggishly at room temperature. The H/D KIEs for methane and benzene hydroxylation have been evaluated in Fe-ZSM-5 using mixed-isotope substrates (e.g., CH_2D_2 and $C_6H_3D_3$; intramolecular KIEs are not susceptible to H/D isotope effects on diffusion).[33] The intramolecular H/D KIE for CH_2D_2 hydroxylation is 1.9 at 100 C, increasing to 5.5 at −50 °C (the temperature dependence of the KIE indicates an H/D $\Delta\Delta H^{\ddagger}$ of 1.2 ± 0.1 kcal/mol), indicating the rate-limiting step in methane hydroxylation is C−H cleavage. On the other hand, the intramolecular H/D KIE for $C_6H_3D_3$ hydroxylation is close to unity at 25 °C (1.05), indicating C−H cleavage does not occur in the rate-limiting step of benzene hydroxylation, characteristic of an electrophilic aromatic substitution mechanism (EAS, vide infra). For Fe-zeolites, the methane reaction is generally considered to be stoichiometric (although conditions enabling multiple turnovers have recently been reported).[201] α-Fe−OH and α-Fe−OCH_3 sites have been identified by isotopically perturbed IR studies following reaction with methane.[202] The −OCH_3 species are described as product-trapped sites formed by methyl radical recombination with α-O. These must be hydrolyzed with steam, releasing methanol. The benzene reaction on the other hand does not suffer from product trapping.[181] There are however issues related to coke formation with aromatic substrates.

Spectroscopically validated DFT models of α-O have provided insight into how its entatic state (vide supra) leads to high reactivity with methane.[35] Reacting α-O (BEA) with CH_4 in silico shows the first fundamental step in the hydroxylation reaction coordinate is H-atom abstraction, which yields an Fe(III)−OH product and a methyl radical (Figure 53). HAA

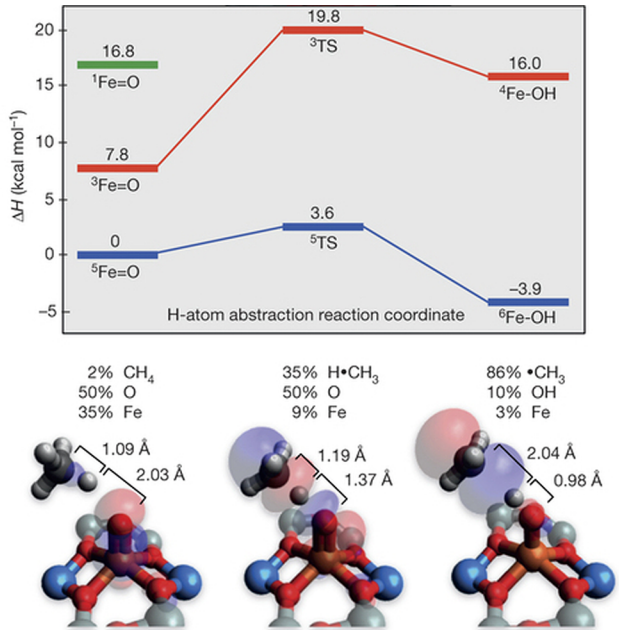

Figure 53. α-O/CH_4 HAA abstraction reaction coordinate (top), including geometric structures and reactive FMOs for the reactants (bottom left), transition state (bottom middle), and products (bottom right). Adapted with permission from ref 35. Copyright 2016 Nature Publishing Group.

occurs on the quintet surface with a low activation barrier of 3.6 kcal/mol (Figure 53, top)—consistent with the room-temperature CH_4 reactivity of α-O. A similar barrier is predicted for Fe-ZSM-5.[178] Two factors contribute to this exceptionally low barrier. First, the HAA reaction is nearly isoenthalpic, indicating the O−H bond of the Fe(III)−OH first product and the C−H

DOI: 10.1021/acs.chemrev.7b00344
Chem. Rev. 2018, 118, 2718−2768

bond of CH_4 are comparable in strength. There is therefore an unusually large driving force for O−H bond formation with α-O, and this substantially lowers the barrier for HAA. The exceptional strength of the product O−H bond is related to the entatic geometry of α-O (see section 5.2.1), which destabilizes the S = 2 Fe(IV)═O active site over the S = 5/2 Fe(III)−OH product, increasing the driving force for O−H bond formation by about 6 kcal/mol. This additional driving force would be quenched by adding a *trans* axial ligand, or by spin pairing (i.e., for the reaction on the S = 1 surface, see Figure 53, top). The enatic state of α-O also leads to high intrinsic reactivity in HAA. The site's entatic geometry (vacant *trans* axial position) stabilizes the Fe($3d_{z^2}$) orbital, resulting in a highly covalent Fe═O unit. This, combined with a large exchange stabilization of the Fe(3d) manifold (associated with the S = 2 electronic structure), leads to an Fe(IV)═O bond that strongly spin-polarizes toward an Fe(III)−$O^{\bullet-}$ electronic structure at the transition-state geometry for HAA (where the Fe−O bond elongates from 1.59 to 1.72 Å).

Unlike methane, the reaction of benzene with α-O (ZSM-5) results in the formation of a spectroscopic intermediate with a broad absorption feature centered at 14 500 cm^{-1}.[94] Using 16 500 cm^{-1} laser excitation, Raman vibrations are observed that have been assigned to a ferric phenolate chromophore. How this spectroscopic intermediate fits with the catalytic cycle for benzene hydroxylation is not yet understood, although it has been proposed that this represents a product-trapped state.[94] The reaction of α-O with benzene has not yet been explored using a spectroscopically validated DFT model. For mononuclear S = 2 non-heme Fe(IV)═O sites, the rate-limiting step in aromatic hydroxylation is believed to be the initial electrophilic attack of the oxo on the aromatic ring.[196,203] This occurs through a radical EAS mechanism, forming a σ-complex with an S = 5/2 Fe(III) center. Whether α-O follows this trend remains to be seen. In this case, the same factors that activate α-O for HAA would be relevant, as the radical EAS mechanism and HAA both generate an axial square pyramidal S = 5/2 Fe(III) first product.

5.3. Selective Hydrocarbon Oxidation with H_2O_2

In addition to the gas-phase oxidation chemistry performed by Fe- and Cu-zeolites using N_2O/O_2, Fe-ZSM-5 has been shown to perform aqueous-phase methane hydroxylation using H_2O_2 at low temperature and high pressures (e.g., 50 °C at 30.5 bar).[92] In contrast to the gas-phase chemistry, the H_2O_2/Fe-ZSM-5 system is catalytic (turnover frequency (TOF) = 14 000 h^{-1}). The initial steps in methane activation are also distinct here, forming MeOOH instead of MeOH. (MeOH is formed via subsequent decomposition of the MeOOH first product.) It is believed that MeOOH formation proceeds via H-atom abstraction.[204] The activation of methane is unaffected by the presence of radical traps. This indicates free peroxyl or hydroxyl radicals (from Fenton chemistry) do not contribute to MeOOH formation, and that reactivity occurs at a bound Fe/O or Fe−OOH intermediate. H-atom abstraction is proposed to be mediated by an activated Fe/O intermediate with an inactive peroxide ligand that does not participate directly in C−H cleavage.[204] The methyl radical product of H-atom abstraction is then proposed to recombine with the peroxide ligand to form MeOOH. This represents a deviation from the mechanisms proposed for the N_2O/O_2 gas-phase oxidation of methane, where the methyl radical recombines directly with the active oxygen. In addition to MeOOH and MeOH, higher oxygenates (formate and CO_2, but not formaldehyde) are observed in the product distribution—sometimes contributing dominantly. This issue has been resolved with the addition of Cu as a cocation.[92] Methanol selectivities exceeding 95% have been achieved for this system, referred to as Cu-promoted Fe-ZSM-5. The role of Cu in improving selectivity is not currently understood.

The iron active site(s) in the H_2O_2/Fe-ZSM-5 system are extralattice species that are distinct from α-Fe(II)/α-O.[205] The nature of the active iron component and its activation by H_2O_2 are not currently understood. Active sites are generated during heat treatment of Fe-ZSM-5 containing isomorphously substituted lattice Fe(III) sites. This causes some Fe(III) to be extruded from the lattice, forming cationic (extralattice) Fe(III) sites. The migration of Fe(III) is evident from DR-UV−vis spectral data shown in Figure 54 (left). Tetrahedral lattice

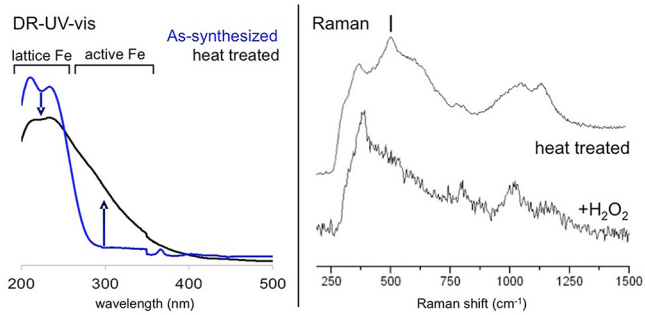

Figure 54. DR-UV−vis changes during heat treatment (left) and UV Raman features (λ_{ex} = 325 nm) correlated with H_2O_2 activation (right, marked peak eliminated).[93,205]

Fe(III) sites exhibit a pair of lattice → Fe(III) CT transitions in the 40 000−50 000 cm^{-1} region, and these decrease in intensity following heat treatment.[205] This is associated with the growth of a new band centered around 33 000 cm^{-1} that is correlated with activity. While the peroxide sensitivity of this band has not yet been evaluated, tuning a laser (325 nm) into this absorption feature enhances a vibration at 521 cm^{-1} that is not present before heat treatment and decays in the presence of peroxide (Figure 54, right).[93] This vibration may be related to the Fe(III) precursor to the reactive intermediate in MeOOH synthesis. Peroxide-induced loss of the 521 cm^{-1} vibration is correlated with growth of a new vibration at 631 cm^{-1} seen only with visible excitation (514 nm). It has been proposed that this is the Fe−O stretch of an Fe(III)−OOH site. This proposal has not been fully evaluated.

6. CORRELATION OF METALLOZEOLITES TO METALLOENZYMES

Parallels have been drawn between metallozeolite and metalloenzyme catalyses, particularly with respect to selective oxidation of methane. Analogies have been proposed between Cu-zeolites and the dicopper active site of particulate methane monooxygenase (pMMO),[66,160,206] and between Fe-zeolites and the diiron active site of soluble methane monooxygenase (sMMO).[33,94,202,207] These analogies can now be evaluated and amended based on emerging insight into metallozeolite and metalloenzyme active sites.

6.1. Cu-Zeolites and pMMO

Particulate methane monooxygenase is an enzyme expressed across methanotrophs that performs the first step of their

DOI: 10.1021/acs.chemrev.7b00344
Chem. Rev. 2018, 118, 2718−2768

metabolism, oxidizing methane to methanol under physiological conditions.[21,208] Like the Cu-zeolites, methane hydroxylation in pMMO is believed to occur at a binuclear Cu active site.[161,162] In resting (as isolated) pMMO, crystallography and ^{14}N ENDOR indicate bis-His ligation for one Cu center, while the other is bound by a terminal histidine and its amine (Figure 55).[162,209] No water/hydroxide ligand is detected by

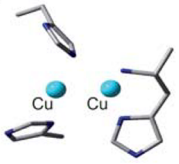

Figure 55. Binuclear Cu active site of pMMO. Reproduced with permission from ref 212. Copyright 2011 Royal Society of Chemistry.

ESEEM.[209] Finally, in the reduced 2Cu(I) state of the pMMO active site, EXAFS shows a short Cu−Cu separation of 2.65 Å (versus 4.2 Å for the geometry optimized reduced 2Cu(I) active site in Cu-zeolites).[135,210]

Adding O_2 or peroxide to the reduced active site of pMMO results in formation of an absorption feature at 345 nm that decays in the presence of methane (Figure 56).[211] (Note that

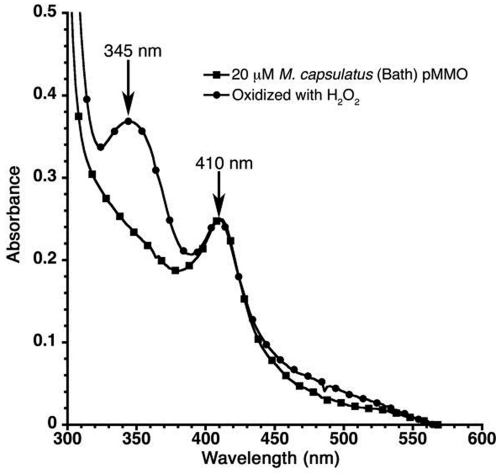

Figure 56. Comparison of absorption data before and after H_2O_2 binding in solubilized pMMO from *Methylococcus capsulatus* (Bath) (absorption at 410 nm due to heme contaminants). Reproduced from ref 211. Copyright 2012 American Chemical Society.

only the solubilized active protomer of pMMO reacts with O_2, and not the full membrane-bound protein—an $\alpha_3\beta_3\gamma_3$ trimer which only reacts with H_2O_2.) This Abs feature is suggested to derive from a μ-η^2:η^2 peroxodicopper(II) intermediate, but this possibility has not been evaluated experimentally. It is also not yet understood how the O_2/H_2O_2-derived species relates to the reactive intermediate in methanol synthesis. In Cu-ZSM-5, a 345 nm Abs feature also forms in the presence of O_2 at room temperature, and using isotopically perturbed rR spectroscopy, this was shown to correspond to a μ-η^2:η^2 peroxodicopper(II) species that upon heating converts to the $[Cu_2O]^{2+}$ reactive intermediate (see section 4.3).[136] Since the $[Cu_2O]^{2+}$ cores in Cu-zeolites are the only spectroscopically characterized dicopper sites that react with methane, there is interest in evaluating whether a $[Cu_2O]^{2+}$ core is a viable intermediate in pMMO catalysis. The methane reactivity of a $[Cu_2O]^{2+}$ core stabilized in the pMMO active site has been explored using DFT, and like Cu-ZSM-5, it was found that polarization toward a 2Cu(I/II)−oxyl electronic structure was key to the high reactivity of this model (Figure 57).[212] The lack of spec-

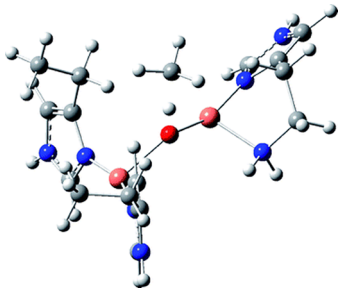

Figure 57. Transition state structure for H-atom abstraction by a $[Cu_2O]^{2+}$ core stabilized at the active site of pMMO. Reproduced with permission from ref 212. Copyright 2011 Royal Society of Chemistry.

troscopic data on the reactive intermediate in pMMO makes it difficult to evaluate this proposal, however.

A more complete comparison can be made to the binuclear Cu enzyme tyrosinase, where extensive spectroscopic and structural data already exist.[18] Tyrosinase activates O_2 to hydroxylate monophenols and oxidize the resulting diphenols to quinones. The active site of tyrosinase ligates each Cu center with three His residues (Figure 58), and in the reduced active site the Cu

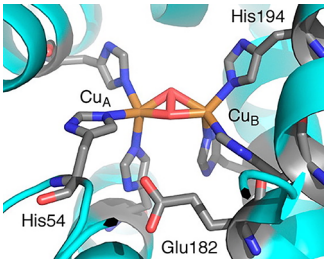

Figure 58. Active site of oxytyrosinase. Adapted from ref 18. Copyright 2014 American Chemical Society.

centers are separated by ca. 4 Å—similar to the Cu-zeolites.[135,213] Like Cu-ZSM-5, O_2 binds to the reduced active site in a bridging peroxo fashion, forming a side-on μ-η^2:η^2 peroxodicopper(II) species that is the reactive intermediate in aromatic hydroxylation.[213] Both the low temperature oxy-Cu-ZSM-5 and oxytyrosinase intermediates are associated with intense 29 000 cm^{-1} $O_2^{2-} \rightarrow$ Cu(II) CT transitions, and tuning a laser into these charge transfer bands enhances similar rR vibrations (Figure 59).[136,214] For oxytyrosinase, the O−O stretch of the peroxide core appears at 755 cm^{-1} ($\Delta^{16/18}O_2$ = 41 cm^{-1}), along with an isotope insensitive Cu−Cu stretch at 274 cm^{-1}.[214,215] For Cu-ZSM-5, analogous features appear at 736 cm^{-1} ($\Delta^{16/18}O_2$ = 41 cm^{-1}) and 269 cm^{-1}. The geometric and electronic structures of these sites are therefore highly similar. The activation of the Cu-ZSM-5 peroxo core for aromatic hydroxylation has not yet been explored, and it will be interesting to see how this compares to oxytyrosinase. However, in contrast to the enzyme, in the zeolite there are spectator Cu sites that can donate two electrons to the μ-η^2:η^2 peroxodicopper(II) intermediate to reductively cleave the O−O bond and generate a $[Cu_2O]^{2+}$ core.[136]

A second role fulfilled by binuclear active sites in Cu-zeolites, in addition to selective hydrocarbon oxidation, is reduction

DOI: 10.1021/acs.chemrev.7b00344
Chem. Rev. 2018, 118, 2718−2768

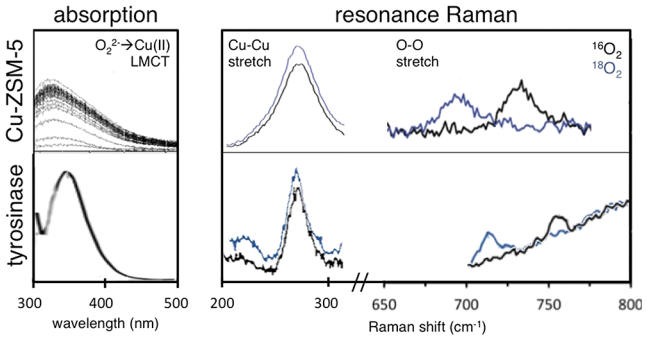

Figure 59. Comparison of absorption (left) and $^{16/18}$O-perturbed resonance Raman spectra (right, λ_{ex} = 364 nm) of the $[Cu_2(O_2)]^{2+}$ cores of oxy-Cu-ZSM-5 (top) and oxytyrosinase (bottom).

of N_2O.[37,135] While the reactivity of pMMO with N_2O has not been explored, direct comparisons can be made between Cu-zeolites and nitrous oxide reductase (N_2OR), a Cu-containing enzyme that catalyzes reduction of N_2O to N_2 and H_2O in the final step in bacterial denitrification.[216] The active site of N_2OR is a tetranuclear Cu_4S cluster (Cu_Z), which features a μ_4-sulfide and Cu ligation provided by histidine residues (Figure 60).[217,218]

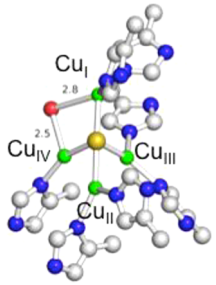

Figure 60. Resting structure of Cu_Z cluster from *P. denitrificans* N_2OR (purified aerobically).[217] Copper is colored in green, sulfide is in yellow, iodine is in purple, and oxygen is in red. Adapted from ref 18. Copyright 2014 American Chemical Society.

The reduced 4Cu(I) form of Cu_Z has a vacancy on the Cu_I–Cu_{IV} edge that is the site of N_2O activation.[218,219] As with Cu-ZSM-5, the ability of N_2O to bridge the adjacent Cu_I/Cu_{IV} centers is key to function, facilitating two-electron reduction during N–O cleavage (Figure 61).[135,151,219] The mechanisms of N_2OR and Cu-ZSM-5 are not comparable, however. In Cu-ZSM-5, N–O cleavage is calculated to proceed from a μ-1,1-O bridged intermediate, where sequential transfer of two electrons from different copper centers to cleave the N–O bond is driven by the formation of strong Cu(II)–oxo bonds.[135] In N_2OR, N_2O bridges in a μ-1,3-O,N fashion and a proton is transferred from a second-sphere residue to the O atom of N_2O during N–O cleavage (Figure 61, bottom), and the electrons are transferred sequentially through one Cu of the Cu_Z cluster to N_2O.[151] The driving force for O–H bond formation is therefore an important contribution to N–O cleavage in N_2OR. This highlights an important difference between enzyme and zeolite catalysis. Whereas proton-coupled electron transfer and sequential proton/electron transfer mechanisms are commonplace in biology, protons are not readily available in gas-phase metallozeolite chemistry and likely do not contribute to reactivity.

6.2. Fe-Zeolites and sMMO

Soluble methane monooxygenase (sMMO) is a diiron enzyme expressed across methanotrophs that oxidizes methane to form

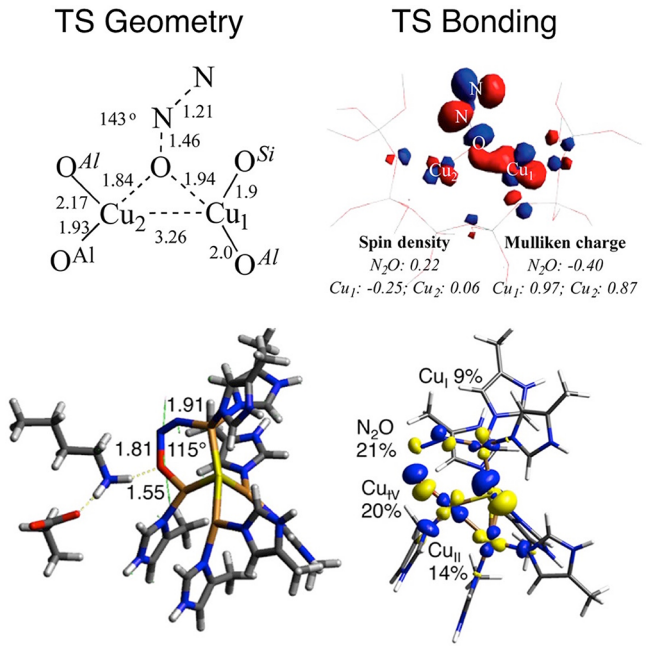

Figure 61. Comparison of transition state structures (left) and bonding (right) for N–O cleavage by reduced Cu-ZSM-5 (top) and reduced Cu_Z (bottom).

methanol using atmospheric O_2.[21] Based on reactivity, structural analogies have been proposed between sMMO and the active site of methane hydroxylation in Fe-zeolites.[33,94,202,207] Combined results from crystallography and spectroscopy have defined the geometric and electronic structure of key catalytic intermediates in sMMO. In contrast to the mononuclear active site of the Fe-zeolites, the sMMO active site is binuclear. The reduced 2Fe(II) state features two five-coordinate Fe centers with histidine and carboxylate ligation, along with two bridging carboxylates, one binding in a μ-1,3 fashion and the other binding μ-1,1 (Figure 62, left).[220] O_2 binds to the vacant coordination positions of the 2Fe(II) active site forming intermediate P, a *cis*-μ-1,2 peroxodiferric site (Figure 62, right).[221] This converts to the active species in methanol synthesis, the high-valent bis-μ-oxo diferryl intermediate Q, which features antiferromagnetically coupled high spin Fe(IV) centers.[222,223] Intermediate Q reacts rapidly with methane at room temperature (ΔH = 8.5 ± 0.3 kcal/mol) with a H/D KIE of 23 ± 1 indicating C–H cleavage (with tunneling) as the rate-limiting step.[224] This forms methanol, as well as the oxo-bridged diferric intermediate T.[221]

The ability to bind and reduce O_2 by four electrons is key to reactivity in sMMO. This is in contrast to Fe-zeolites, where the reduced α-Fe(II) active site does not bind O_2,[32] but does bind and reduce N_2O by two electrons to form α-O, a mononuclear S = 2 terminal Fe(IV)=O species.[35] The geometric and electronic structures of α-O and sMMO Q are distinct, and there are differences in the strategies used by each site to achieve high reactivity. Whereas α-O is a mononuclear site held in a reactive "entatic" geometry by the rigid zeolite lattice (see section 6.3.3 for details),[35] the reactivity of sMMO Q is related to the intrinsic activation of the $[Fe_2O_2]^{4+}$ diamond core motif having two antiferromagnetically coupled high spin Fe(IV) centers. Like α-O, it is likely that one of the bridging oxos in sMMO Q evolves oxyl character at the methane HAA transition state geometry.[225] However, the mechanism of FMO

DOI: 10.1021/acs.chemrev.7b00344
Chem. Rev. 2018, 118, 2718–2768

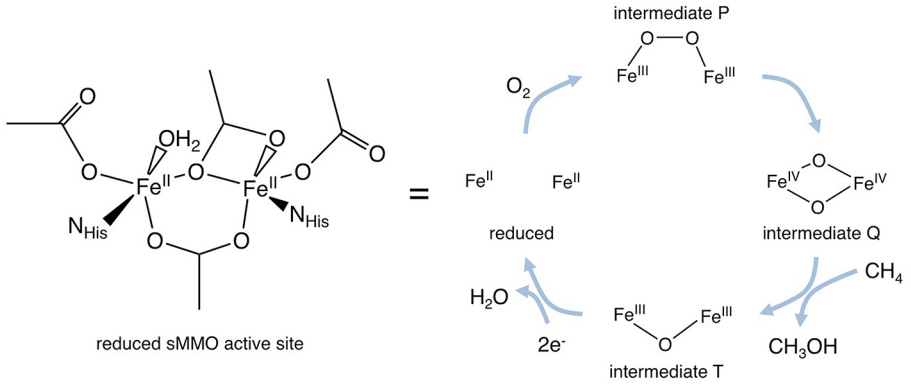

Figure 62. Structure of the reduced sMMO active site (left), along with key intermediates in catalysis (right).

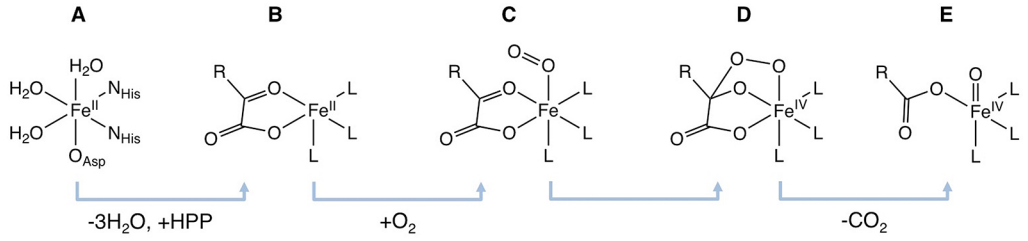

Figure 63. Analogous catalytic intermediates for HPPD and HmaS (R = 4-hydroxybenzyl).

polarization, the driving force for O−H bond formation, and how these relate to the coupling between the Fe centers has not yet been presented.

For α-O, a more direct comparison to biology can be made with the mononuclear S = 2 Fe(IV)═O active intermediates in the α-keto acid-dependent non-heme Fe enzymes 4-hydroxyphenylpyruvate dioxygenase (HPPD) and 4-hydroxymandelate synthase (HmaS).[226,227] HPPD and HmaS have comparable active site structures and act on the same substrate (4-hydroxyphenylpyruvate, HPP), but react differently: HPPD performs electrophilic aromatic hydroxylation, while HmaS performs aliphatic hydroxylation through H-atom abstraction. This difference in function is ascribed to differences in the orientation of the substrate by the HPPD/HmaS active site pockets, and not to differences in intrinsic reactivity of the Fe(IV)═O cores.[196] HPPD/HmaS can therefore be compared directly to α-O, which is also a mononuclear S = 2 Fe(IV)═O intermediate active in aliphatic and aromatic hydroxylation.[33,35]

For HPPD/HmaS, the reduced Fe(II) form of the active site is six-coordinate, with three protein-derived ligands (two His, one carboxylate) and three weakly coordinated waters (Figure 63A).[228,229] The HPP substrate binds in a bidentate fashion to the reduced active site, displacing two bound water molecules, and labilizing the third (Figure 63B). This results in a mixture of water-unbound (five-coordinate) and bound (six-coordinate) forms.[230] The coordinatively unsaturated five-coordinate site then reacts with O_2 (Figure 63C). It is believed that this forms a transient FeO_2 species that nucleophilically attacks the α carbon of the α-keto acid substrate, forming a peroxide bridge that subsequently decays through oxidative decarboxylation to generate an S = 2 Fe(IV)═O reactive intermediate with a monodentate-bound hydryoxyphenyl acetate (HPA; Figure 63D,E).[196]

For these Fe(IV)═O intermediates, two different reaction pathways are possible depending on the orientation of the benzyl group of the HPA substrate (R in Figure 63) imposed by the active site protein pocket.[196] For HPPD, the ipso carbon of the HPA aromatic ring is oriented along the d_{z^2}-derived α LUMO of the S = 2 Fe(IV)═O core, which has significant (28%) O(p_z) character (Figure 64, top left). This orbital pathway for reactivity defines the σ channel in HPPD, which is associated with a 16 kcal/mol predicted barrier for C−O bond formation (transition state shown in Figure 64, top right).[196] For HmaS, a benzylic hydrogen of HPA is oriented along a d_π-derived β LUMO, which has significant (32%) O(p_π) character (Figure 64, bottom left). This defines the π channel in HmaS, which is associated with a 14 kcal/mol predicted barrier for H-atom abstraction (transition state shown in Figure 64, bottom right). Thus, low barriers are accessible through both the σ and π channels, and in both cases an important contribution to reactivity is evolution of ferric−oxyl character with Fe═O elongation at the transition state.[196]

Compared to HPPD/HmaS, the S = 2 Fe(IV)═O core of α-O is significantly more reactive due to its constrained geometry.[35] The enzyme intermediates are predicted to have square pyramidal geometry with an equatorial oxo ligand,[196] and this is the most stable geometry for a five-coordinate S = 2 Fe(IV)═O site.[196,197] In contrast, the axial square pyramidal geometry of α-O is inherently unstable (Figure 51), and is enforced by rigid constraints from the zeolite lattice.[35] Differences in geometric structure lead to differences in electronic structure and thus reactivity. With respect to H-atom abstraction, placing the oxo in the axial position destabilizes the S = 2 Fe(IV)═O over the S = 5/2 Fe(III)−OH product, increasing the driving force for O−H bond formation.[35] As shown in Figure 65, this geometry also leads to higher Fe═O covalency, resulting in a more stable α-LUMO with higher O(p_z) content (50% for α-O versus 28% for HPPD).[35,196] The α-O electronic structure also evolves ferric−oxyl character at shorter Fe−O distances relative to HmaS, resulting in a significantly lower barrier for HAA from a much stronger C−H bond (14 kcal/mol barrier for a ∼ 90 kcal/mol benzylic C−H bond for HmaS versus a

DOI: 10.1021/acs.chemrev.7b00344
Chem. Rev. 2018, 118, 2718−2768

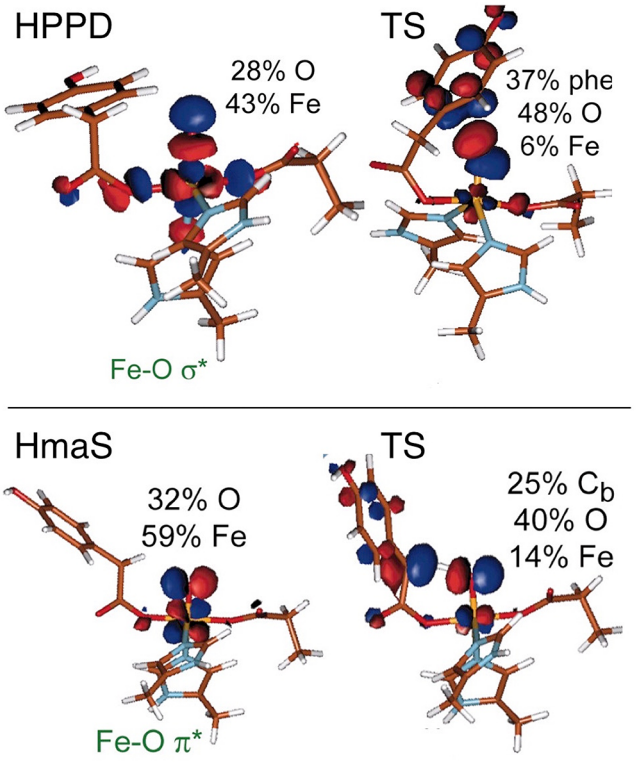

Figure 64. Active sites of HPPD (top) and HmaS (bottom) orient different atoms of the substrate toward different reactive molecular orbitals of the Fe(IV)=O core, resulting in different reactivity (electrophilic aromatic hydroxylation,top right; H-atom abstraction, bottom right). Adapted with permission from ref 196. Copyright 2006 National Academy of Sciences.

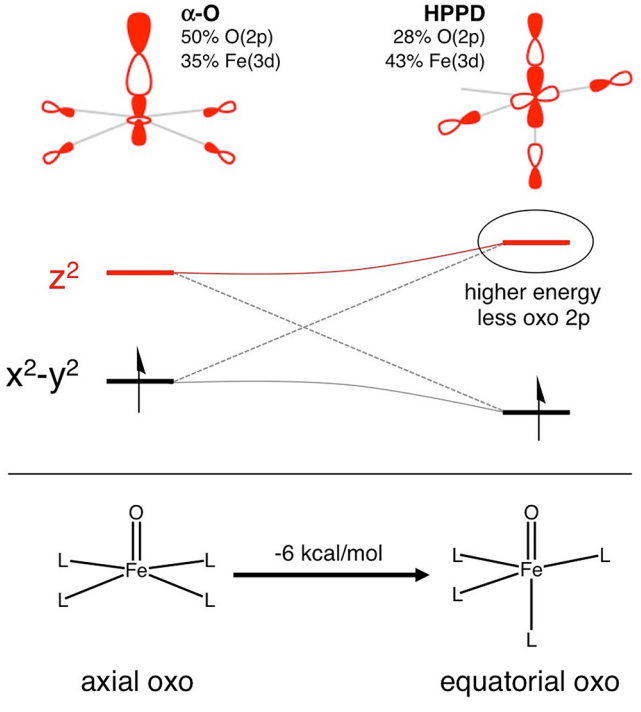

Figure 65. Variation of the reactive LUMO (red) of a square pyramidal $S = 2$ Fe(IV)=O site upon shifting the oxo ligand from the axial (left) to the equatorial position (right).

4 kcal/mol barrier for a 104 kcal/mol methane C−H bond for α-O).[35,196]

With respect to electrophilic aromatic hydroxylation, it is known that α-O is extremely reactive, converting benzene to phenol under mild reaction conditions.[33,94,181,182] The molecular-level details of the reaction mechanism for α-O have not yet been determined. Whereas the approach of methane along the π channel is sterically unencumbered, the σ channel may be important for the more sterically demanding benzene substrate. When experimental insight into the benzene reaction becomes available, it will be interesting to draw comparisons to electrophilic aromatic hydroxylation by HPPD—particularly with respect to σ versus π channel reactivity, which has not yet been evaluated experimentally or computationally for α-O.

6.3. From Bioinorganic to Zeolite Catalysis: Tuning the Reactivity of Metal Active Sites

While metallozeolite and metalloenzyme active sites are not structurally comparable (vide supra), there are important parallels regarding their activation for reactivity. These include high metal−oxygen covalency (section 6.3.1), tuning of reactivity by second-sphere atoms (section 6.3.2), and entatic effects (section 6.3.3). These parallels, emerging from recent spectroscopic insight into metallozeolite and metalloenzyme active sites, highlight potentially useful mechanisms to tune the reactivity of catalysts.

6.3.1. Metal−Oxygen Covalency. Reactive oxygen intermediates across metalloenzymes and metallozeolites exhibit spectroscopic features reflecting high metal−oxygen covalency (e.g., intense, low energy oxygen → metal charge transfer transitions in absorption spectroscopy).[18,19] Combined spectroscopic and computational studies have shown that this is an important contribution to the activation of these intermediates, increasing the oxygen 2p content of the unoccupied metal 3d-derived orbitals that participate in electrophilic reactivity. Nature has therefore evolved active site architectures that lead to highly covalent Cu and non-heme Fe reactive oxygen intermediates.

For Fe enzymes, these involve ligands that donate strongly enough to stabilize high-valent oxidation states (e.g., ferryl iron), but also weakly enough to stabilize high spin electronic structures. Zeolites can also perform this balancing act, stabilizing high-valent high spin Fe(IV)=O intermediate using a weak zeolite lattice ligand field (α-O).[35] For both the Fe enzymes and zeolites, high oxidation states are associated with electron-deficient metal centers, and exogenous oxygen ligands will donate strongly to compensate for this, resulting in high metal−oxygen covalency and low-lying unoccupied acceptor orbitals. For the mononuclear Fe(IV)=O intermediates, a high spin electronic structure makes it possible to achieve low barriers through covalency-activated π and σ channels.[35,131,196,199,200] (This is in contrast to $S = 1$ Fe(IV)=O intermediates, where only the π channel is accessible.[196]) For the binuclear $[Fe_2(O)_2]^{4+}$ intermediate Q in sMMO, it is not yet understood how the exchange coupled high spin state of the Fe(IV) centers relates to the activation of this site for H-atom abstraction from methane.

For both the Cu enzymes and Cu-zeolites, there is no evidence that high-valent Cu(III) contributes to catalysis. Instead, high reactivity is achieved with Cu(II) species.[18] For example, a direct comparison can be made between oxytyrosinase and oxy-Cu-ZSM-5, which contain highly similar μ-η^2:η^2 peroxodicopper(II) cores (vide supra). For these sites, high covalency is achieved through good orbital overlap and energy match

DOI: 10.1021/acs.chemrev.7b00344
Chem. Rev. 2018, 118, 2718−2768

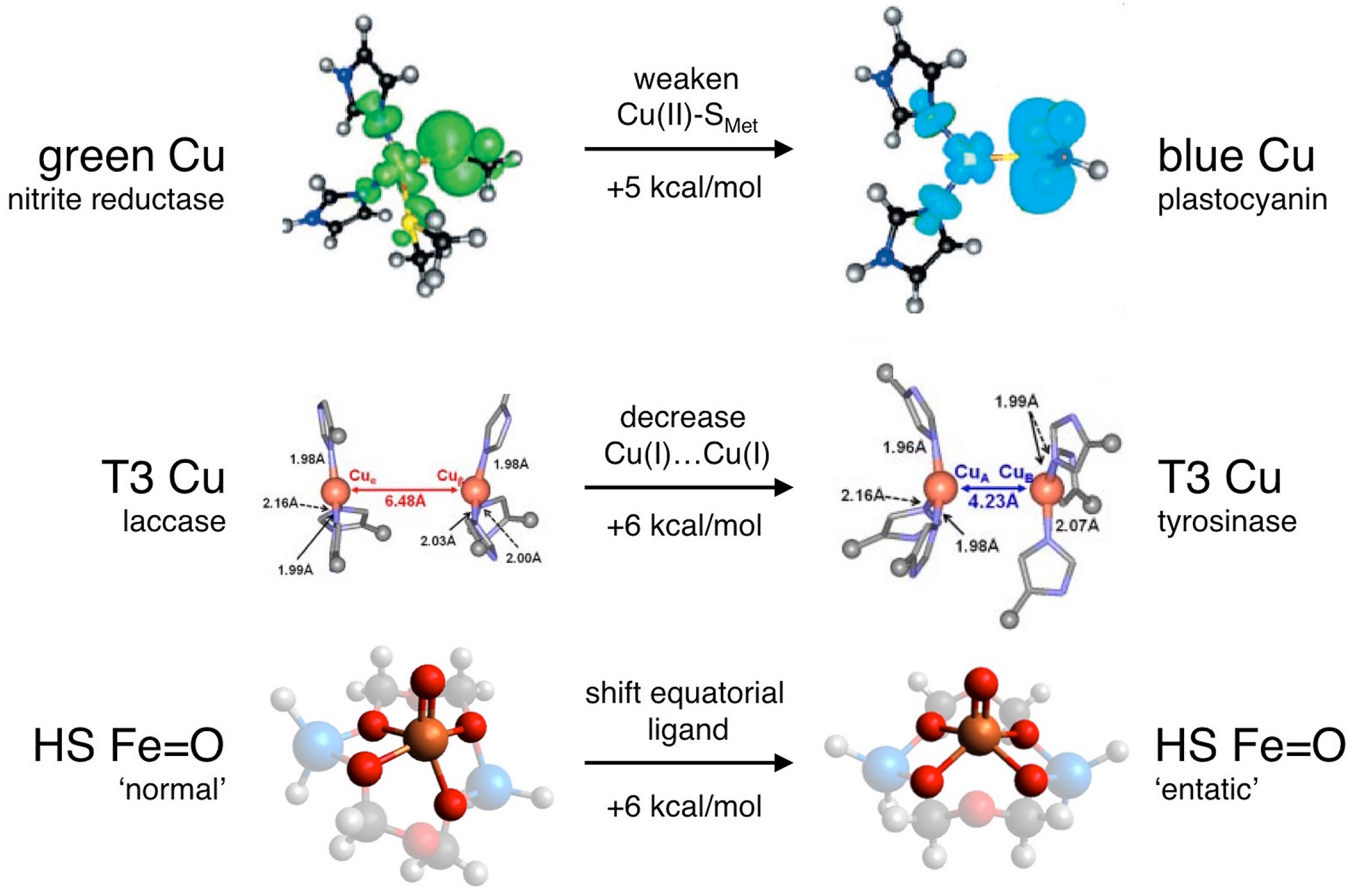

Figure 66. Comparison of "normal" (left) and "entatic" (right) metal active sites. Each "normal" site undergoes a 5−6 kcal distortion that primes the corresponding "entatic" site for function.

between the filled π^* orbitals of peroxide and the $3d_{x^2-y^2}$ holes of the Cu(II) centers. The role of the zeolite lattice in tuning the covalency of the mono-oxo $[Cu_2O]^{2+}$ site is different, however, and not comparable to the Cu enzymes. In this case, the O(2p) orbitals of the bridging oxo are stabilized relative to a bridging peroxide ligand. To counteract this, the zeolite lattice keeps the Cu(II) centers undercoordinated, and thus electron deficient. This brings the unfilled 3d orbitals of the Cu(II) centers closer in energy to the filled O(2p) orbitals, tuning up covalency. (This is in contrast to small molecule $[Cu_2O]^{2+}$ sites in the literature, which are coordinated by three or more strongly donating nitrogen ligands, and display significantly reduced reactivity.[231−235]) While the use of a low coordination number to achieve a high covalency is not significant in Cu/O biochemistry,[18] this is a key facet of the blue Cu electron transfer site (see section 6.3.3).[117,121]

6.3.2. Second-Sphere Effects. Atoms outside of the first coordination sphere can contribute significantly to reactivity in metalloenzyme active sites. This was seen in section 6.1, where N_2OR facilitates N−O cleavage using a proton transferred from a second-sphere lysine residue,[151] and also in section 6.2, where the steric environments of the active site pockets of HPPD/HmaS guide reactivity through substrate orientation effects.[196] The latter effect—second-sphere influences based on sterics—may have direct parallels in metallozeolite chemistry.[134] This builds on the concept of shape-selective catalysis,[236] where the zeolite lattice and protein fold play analogous roles in guiding entry of substrate and release of product. For zeolites, this has mostly focused on the role of the lattice in tuning product distributions, especially with respect to hydrocarbon isomerization and alkylation catalyzed by acid sites. Recent studies of Cu-MOR have extended this concept to include second-sphere influence on the reactivity of metal sites in zeolites.[134] In Cu-MOR (Si/Al = 5), two $[Cu_2O]^{2+}$ cores are present with highly similar absorption and resonance Raman spectral features, and thus highly similar geometric and electronic structures. The reactivity of these sites with CH_4 is distinct, however. One site has kinetic parameters similar to Cu-ZSM-5 ($\Delta H^{\ddagger}$ = 15 kcal/mol, $\Delta S^{\ddagger}$ = −36 cal/mol K), while the other has a lower barrier ($\Delta H^{\ddagger}$ = 11 kcal/mol) and larger entropy of activation ($\Delta S^{\ddagger}$ = −44 cal/mol K). Spectroscopy shows this difference in reactivity does not derive from differences in electronic structure. Instead, it was observed that the site with the smaller $\Delta H^{\ddagger}$ = 11 kcal/mol has a larger $\Delta S^{\ddagger}$ = −44 cal/mol K, and this entropic compensation is consistent with the confined reaction environment predicted for this site (buried in the side pockets or compressed 8MR channels of the MOR lattice). Here, there is a direct parallel to the coupled binuclear Cu enzymes hemocyanin, tyrosinase, and catechol oxidase.[18] These stabilize μ-η^2:η^2 peroxodicopper(II) cores with highly similar spectral features yet different reactivities based on how the active site pocket guides the approach of substrate. The nature of the second-sphere effect in Cu-MOR is not yet understood, however. This may be related to steric effects, or alternatively to direct participation of second-sphere atoms in tuning the HAA reaction coordinate.

6.3.3. The Entatic State. The entatic concept evolved from studies of metalloenzyme active sites, where protein constraints

DOI: 10.1021/acs.chemrev.7b00344
Chem. Rev. 2018, 118, 2718−2768

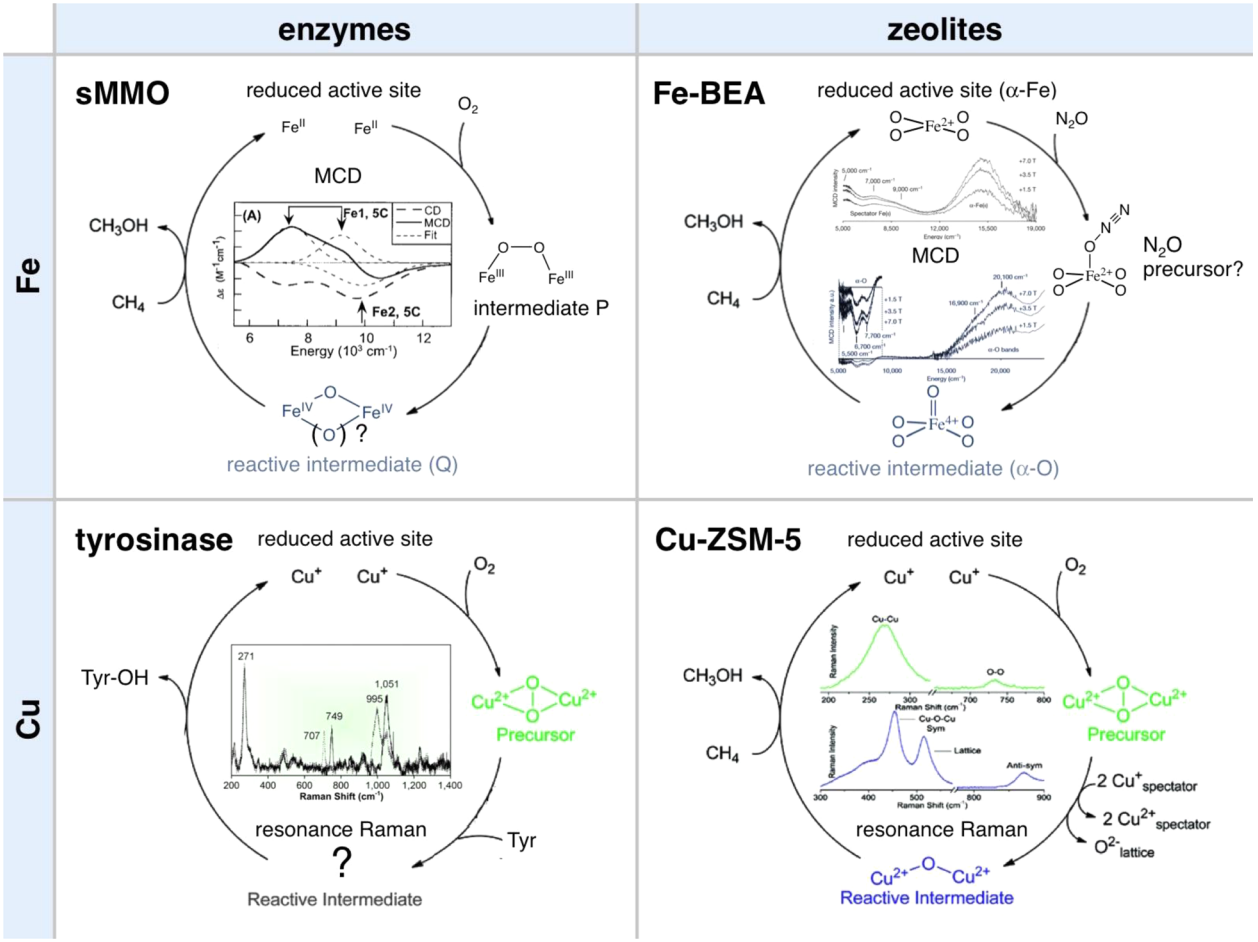

Figure 67. Comparison of Fe and Cu enzymes and zeolites that hydroxylate strong C−H bonds at low temperature, including their active site structures and catalytic intermediates defined from spectroscopy.

enforce an otherwise unstable geometry that is associated with high activity.[118] This was first defined for the type 1 "blue" Cu active site of biological electron transfer found in plastocyanin and the multicopper oxidases (MCOs), among others (see Figure 66, top right).[117] This is a mononuclear Cu center with trigonal pyramidal geometry, where the trigonal plane is defined by two histidine ligands and a cysteinate with a short (2.13 Å), covalent Cu−S bond.[117] At ∼2.9 Å, there is an axial methionine that tunes down the reduction potential of the site to match biological electron transfer partners. Comparison to the analogous green Cu site (Figure 66, top left), which has a less constrained Cu(II)−S_{Met} bond, showed constraints from the protein backbone keep the weak Cu(II)−S_{Met} bond in the blue Cu site intact by opposing the entropic contribution to the Gibbs free energy for Met dissociation.[121] Protein constraints play a similar role in enforcing the weak axial Fe−S_{Met} bond in cytochrome *c*, keeping the axial Met bound to the iron center under physiological conditions.[237] The entatic stabilization of the Fe−S_{Met} bond has been directly quantified at ∼4 kcal/mol, and this prevents ligation by a nearby His residue or water, which would lower the reduction potential of the active site. (Stabilization of the Fe−S_{Met} is important for function in electron transfer; however, the bond remains weak enough to be broken, which activates cytochrome *c* for its role in initiating apoptosis.[237]) Protein constraints also play an important role in tuning the O_2 binding affinity of the binuclear type 3 Cu active sites in hemocyanin and the multicopper oxidases (Figure 66, middle).[238] In hemocyanin (Figure 66, middle right), the active site enforces a short Cu(I)···Cu(I) separation of ∼4 Å and this allows for high-affinity O_2 binding. In the multicopper oxidases (Figure 66, middle left), the type 3 Cu site has a longer Cu(I)···Cu(I) separation of ∼6 Å, and this causes O_2 binding to be thermodynamically disfavored.[238] (The type 3 site of the MCOs is part of a trinuclear cluster that only reacts with O_2 with the participation of the third metal center.) Relative to the 2Cu(I) site in the MCOs, protein constraints in hemocyanin destabilize the 2Cu(I) site by ∼6 kcal/mol due to increased electrostatic repulsion, and this increases the driving force for O_2 binding.[238] Thus, entatic contributions of ∼5 kcal/mol play an important role in activating a range of metalloenzyme active sites for function.

Similar concepts emerge for the *α*-O site in Fe-zeolites and its activation for rapid H-atom transfer (see section 6.3).[35] *α*-O is a mononuclear, high spin Fe(IV)═O site with square pyramidal geometry, where the oxo ligand is bound in the axial position (as in Figure 66, bottom right). This geometry coupled to a high spin d^4 electronic structure activates *α*-O for rapid H-atom abstraction from strong C−H bonds (e.g., methane). The high spin state results in occupation of the $d_{x^2-y^2}$ orbital, which is strongly antibonding with respect to the equatorial ligands. The weak interaction with the equatorial ligands coupled to a vacant *trans* axial position is compensated by strong donation of the oxo, resulting in an unusually covalent Fe═O bond that efficiently polarizes toward a ferric−oxyl

DOI: 10.1021/acs.chemrev.7b00344
Chem. Rev. 2018, 118, 2718−2768

electronic structure with minimal Fe−O elongation. This results in high oxo 2p content in the reactive molecular orbitals, making α-O intrinsically activated for H-atom transfer. There is also an unusually strong O−H bond in the Fe(III)−OH first product (over 100 kcal/mol), and this results in a large driving force of H-atom transfer associated with axial square pyramidal geometry.

The geometric/electronic structure of α-O that leads to high reactivity is inherently unstable, as a high spin d^4 square pyramidal site with a strong axial ligand will experience a distorting force to shift an equatorial ligand to fill the vacant *trans* axial position (see Figure 51 and Figure 66, bottom left).[35,197] This distortion would result in stronger bonding to the zeolite lattice, stabilizing the site by 6 kcal/mol. Placing a ligand *trans* to the oxo would result in a weaker Fe=O bond, and thus a deactivated electronic structure, as well as a decreased driving force for O−H bond formation. The zeolite lattice therefore activates α-O by providing enough distortion energy to enforce a high spin square pyramidal site with an axial oxo—similar in magnitude to the entatic effects quantified for metalloenzyme active sites (vide supra).

7. CONCLUDING COMMENTS

In this review, we have discussed the current state of the art in selective hydrocarbon oxidation by metallozeolites. These catalysts carry out remarkable chemistry, activating O_2 (and N_2O) to form intermediates that selectively hydroxylate the highly inert C−H bonds of methane and benzene under mild conditions. Copper and iron active sites have taken a central role in this review, as these are associated with the highest activity in selective hydrocarbon oxidation. We note that Cu- and Fe-zeolites perform a number of other interesting reactions not discussed here, including selective catalytic reduction of NO_x pollutants.[239] Zeolites containing other metals are also known to activate methane, but at higher temperatures and with diminished selectivity for methanol. Studies discussed in this review demonstrate that molecular-level insight from site selective spectroscopy is vital for understanding the geometric and electronic structures, and therefore reactivities, of metal active sites in zeolites. While we have focused on coupling spectroscopic data to initial steps in H-atom abstraction and electrophilic aromatic hydroxylation, we anticipate spectroscopy will soon elucidate subsequent steps in these reaction coordinates (i.e., C−O bond formation in methanol and phenol synthesis). These relate directly to issues with catalyst performance, such as deactivation through product trapping.

Advances in spectroscopic methodology discussed in this review have elevated the insight available for heterogeneous active sites to the level achieved in bioinorganic chemistry. Cu- and Fe-zeolites (Cu-ZSM-5/MOR and Fe-BEA, in particular) are now among the most thoroughly characterized systems that activate methane and benzene. This has enabled direct comparison to biology, where iron and copper active sites are also used to activate methane and aromatic compounds (Figure 67). While there are significant differences between metallozeolites and metalloenzymes—in particular, that α-O is mononuclear while intermediate Q in sMMO is binuclear—we have also highlighted three parallels between heterogeneous and biological chemistry: (1) the tuning of metal−oxygen covalency to access highly reactive intermediates, (2) second-sphere effects on catalysis, and (3) entatic effects leading to active site geometric and electronic structures that are associated with high reactivity. It will be interesting to see how these features can be used to tune the reactivities of metallozeolite catalysts.

AUTHOR INFORMATION

Corresponding Authors

*E-mail: edward.solomon@stanford.edu.
*E-mail: bert.sels@biw.kuleuven.be.
*E-mail: robert.schoonheydt@biw.kuleuven.be.

ORCID

Bert F. Sels: 0000-0001-9657-1710
Edward I. Solomon: 0000-0003-0291-3199

Notes

The authors declare no competing financial interest.

Biographies

Benjamin E. R. Snyder received his B.S. in chemistry and B.A. in mathematics from the University of Rochester in 2012. He is now an NSF predoctoral fellow and Stanford Graduate Fellow pursuing his Ph.D. in physical inorganic chemistry at Stanford University under the supervision of Prof. Edward Solomon. His research focuses on spectroscopic and computational elucidation of Cu and Fe active sites in zeolites, their activation for selective hydrocarbon oxidation, and their correspondence to Cu and Fe active sites in biology.

Max L. Bols received his B.S. and M.S. in bioscience engineering at the KU Leuven in 2015, doing his master's thesis on the identification of the active site in iron zeolites for methane activation. Upon graduation, he started a Ph.D. with Prof. Bert Sels on the synthesis, kinetics, and spectroscopic characterization of transition metal active sites in zeolites, in the framework of an FWO research grant.

Robert A. Schoonheydt is emeritus professor of the KU Leuven, where he obtained his bioengineering degree in 1966 and his Ph.D. in 1970 under the guidance of Prof. Jan B. Uytterhoeven. He did a postdoc in the chemistry department of the Texas A&M University under the guidance of Jack H. Lunsford on adsorption of SO_2 on MgO. His research interests at the KU Leuven are the surface chemistry of clay minerals and zeolites with special emphasis on transition metal ions and spectroscopy. Presently he is a member of an international research collaboration of zeolite chemists, spectroscopists, and quantum chemists on active sites in Cu- and Fe-zeolites for selective oxidation, NO_x abatement, and electrophilic aromatic substitution reactions. He was dean of the Faculty of Bioscience Engineering from 1998 until 2004 and president of the International Association for the Study of Clays from 2001 until 2005.

Bert F. Sels (1972), currently full professor at KU Leuven (Belgium), obtained his Ph.D. in 2000 in the field of heterogeneous oxidation catalysis under the guidance of Prof. Pierre Jacobs. He was awarded the DSM Chemistry Award in 2000, the Incentive Award by the Belgian Chemical Society in 2005, and the international Green Chemistry Award in 2015. He is currently director of the Centre for Surface Chemistry and Catalysis (COK), and is active in designing heterogeneous catalysts for future challenges in industrial organic and environmental catalysis. His expertise includes heterogeneous catalysis in biorefineries, design of hierarchical zeolites and carbons, and the spectroscopic and kinetic study of active sites for small-molecule activation. He is cochair of the Catalysis Commission of the International Zeolite Association (IZA) and cofounder of the European Research Institute of Catalysis (ERIC). He is also a member of the European Academy of Sciences and Arts, member of the international advisory board of *ChemSusChem* (Wiley), and associate editor of *ACS Sustainable Chemistry & Engineering*.

Edward I. Solomon grew up in North Miami Beach, FL, received his Ph.D. at Princeton (with D. S. McClure), and was a postdoctoral fellow at The Ørsted Institute (with C. J. Ballhausen) and then at Caltech (with

DOI: 10.1021/acs.chemrev.7b00344
Chem. Rev. 2018, 118, 2718−2768

H. B. Gray). He was a professor at the Massachusetts Institute of Technology until 1982, when he joined the faculty at Stanford University, where he is now the Monroe E. Spaght Professor of Humanities and Sciences and Professor of Photon Science at the SLAC National Accelerator Lab. He has been an invited professor in Argentina, Australia, Brazil, China, France, India, and Japan. Prof. Solomon's research is in the fields of physical inorganic chemistry and bioinorganic chemistry with emphasis on the application of a wide range of spectroscopic methods combined with QM calculations to elucidate the electronic structure of transition metal sites and its contribution to physical properties and reactivity. He has received a wide range of medals and awards and is a member of the National Academy of Sciences and the American Academy of Arts and Sciences and a fellow in the American Association for the Advancement of Science and the American Chemical Society.

ACKNOWLEDGMENTS

B.E.R.S. acknowledges support from the National Science Foundation Graduate Research Fellowship Program under Grant DGE-11474, and from the Munger, Pollock, Reynolds, Robinson, Smith & Yoedicke Stanford Graduate Fellowship. Funding for this work was provided by the National Science Foundation (Grant CHE-1660611 to E.I.S.), and Research Foundation—Flanders (FWO Grant G0A2216N to B.F.S.).

ABBREVIATIONS

Abs	absorption spectroscopy
BAS	Brønsted acid sites
CASPT	complete active space perturbation theory
CD	circular dichroism
CEC	cation exchange capacity
CHA	chabazite
DFT	density functional theory
DR	diffuse reflectance
ENDOR	electron nuclear double resonance
EPR	electron paramagnetic resonance
ESEEM	electron spin echo envelope modulation
FAU	faujasite
FER	ferrierite
HAA	H-atom abstraction
HmaS	hydroxymandelate synthase
HPPD	hydroxyphenylpyruvate dioxygenase
KIE	kinetic isotope effect
LCP	left circularly polarized
LF	ligand field
LMCT	ligand to metal charge transfer
LTA	Linde type A zeolite
MCD	magnetic circular dichroism
MFI	mordenite framework, inverted
MOR	mordenite
MR	membered ring
NIH	National Institutes of Health
NIR	near infrared
NRVS	nuclear resonance vibrational spectroscopy
pMMO	particulate methane monooxygenase
RCP	right circularly polarized
rR	resonance Raman spectroscopy
SCR	selective catalytic reduction
sMMO	soluble methane monooxygenase
SOC	spin−orbit coupling
TEM	transmission electron microscopy
TMI	transition metal ion
UV	ultraviolet
vis	visible
VTVH	variable-temperature variable-field
XAS	X-ray absorption spectroscopy
XPS	X-ray photoelectron spectroscopy
XANES	X-ray absorption near edge spectroscopy
EXAFS	extended X-ray absorption fine structure
ZFS	zero-field splitting
ZSM-5	zeolite Socony Mobil-5

REFERENCES

(1) Berkowitz, J.; Greene, J. P.; Cho, H.; Ruščić, B. Photoionization Mass Spectrometric Studies of SiHn (n = 1−4). *J. Chem. Phys.* **1987**, *86*, 1235−1248.
(2) Brocławik, E. Density Functional Theory in Catalysis: Activation and Reactivity of a Hydrocarbon Molecule on a Metallic Active Site. *Adv. Quantum Chem.* **1998**, *33*, 349−367.
(3) Olivos-Suarez, A. I.; Szécsényi, À.; Hensen, E. J. M.; Ruiz-Martinez, J.; Pidko, E. A.; Gascon, J. Strategies for the Direct Catalytic Valorization of Methane Using Heterogeneous Catalysis: Challenges and Opportunities. *ACS Catal.* **2016**, *6*, 2965−2981.
(4) Periana, R. A.; Taube, D. J.; Evitt, E. R.; Löffler, D. G.; Wentrcek, P. R.; Voss, G.; Masuda, T. A Novel, High Yield System for the Oxidation of Methane to Methanol. *Stud. Surf. Sci. Catal.* **1994**, *81*, 533−544.
(5) Periana, R. A.; Bhalla, G.; Tenn, W. J.; Young, K. J. H.; Liu, X. Y.; Mironov, O.; Jones, C.; Ziatdinov, V. R. Perspectives on Some Challenges and Approaches for Developing the next Generation of Selective, Low Temperature, Oxidation Catalysts for Alkane Hydroxylation Based on the CH Activation Reaction. *J. Mol. Catal. A: Chem.* **2004**, *220*, 7−25.
(6) Shilov, A. E.; Shul'pin, G. B. Activation of C−H Bonds by Metal Complexes. *Chem. Rev.* **1997**, *97*, 2879−2932.
(7) *Alkane C-H Activation by Single-Site Metal Catalysis*; Pérez, P. J., Ed.; Catalysis by Metal Complexes 38; Springer Netherlands: Dordrecht, 2012.
(8) Periana, R. A. Platinum Catalysts for the High-Yield Oxidation of Methane to a Methanol Derivative. *Science* **1998**, *280*, 560−564.
(9) Stahl, S. S.; Labinger, J. A.; Bercaw, J. E. Homogeneous Oxidation of Alkanes by Electrophilic Late Transition Metals. *Angew. Chem., Int. Ed.* **1998**, *37*, 2180−2192.
(10) Hammond, C.; Conrad, S.; Hermans, I. Oxidative Methane Upgrading. *ChemSusChem* **2012**, *5*, 1668−1686.
(11) Olah, G. A.; Goeppert, A.; Prakash, G. K. S. *Beyond Oil and Gas: The Methanol Economy*; Wiley-VCH: 2009.
(12) Horn, R.; Schlögl, R. Methane Activation by Heterogeneous Catalysis. *Catal. Lett.* **2015**, *145*, 23−39.
(13) Khan, M. S.; Park, J. H.; Chaniago, Y. D.; Lee, M. Energy Efficient Process Structure Design of LNG/NGL Recovery for Offshore FLNG Plant. *Energy Procedia* **2014**, *61*, 599−602.
(14) Gao, J.; Zheng, Y.; Jehng, J.-M.; Tang, Y.; Wachs, I. E.; Podkolzin, S. G. Identification of Molybdenum Oxide Nanostructures on Zeolites for Natural Gas Conversion. *Science* **2015**, *348*, 686−690.
(15) Liptáková, B.; Báhidský, M.; Hronec, M. Preparation of Phenol from Benzene by One-Step Reaction. *Appl. Catal., A* **2004**, *263*, 33−38.
(16) Stahl, S. S.; Alsters, P. L. *Liquid Phase Aerobic Oxidation Catalysis: Industrial Applications and Academic Perspectives*; Wiley-VCH: 2016.
(17) Labinger, J. A.; Bercaw, J. E. Understanding and Exploiting C-H Bond Activation. *Nature* **2002**, *417*, 507−514.
(18) Solomon, E. I.; Heppner, D. E.; Johnston, E. M.; Ginsbach, J. W.; Cirera, J.; Qayyum, M.; Kieber-Emmons, M. T.; Kjaergaard, C. H.; Hadt, R. G.; Tian, L. Copper Active Sites in Biology. *Chem. Rev.* **2014**, *114*, 3659−3853.
(19) Solomon, E. I.; Brunold, T. C.; Davis, M. I.; Kemsley, J. N.; Lee, S.-K.; Lehnert, N.; Neese, F.; Skulan, A. J.; Yang, Y.-S.; Zhou, J. Geometric and Electronic Structure/function Correlations in Non-Heme Iron Enzymes. *Chem. Rev.* **2000**, *100*, 235−350.

DOI: 10.1021/acs.chemrev.7b00344
Chem. Rev. 2018, 118, 2718−2768

(20) Guroff, G.; Renson, J.; Udenfriend, S.; Daly, J. W.; Jerina, D. M.; Witkop, B. Hydroxylation-Induced Migration: The NIH Shift. *Science* **1967**, *157*, 1524−1530.
(21) Ross, M. O.; Rosenzweig, A. C. A Tale of Two Methane Monooxygenases. *JBIC, J. Biol. Inorg. Chem.* **2017**, *22*, 307−319.
(22) Hagen, J. *Industrial Catalysis: A Practical Approach*, 2nd ed.; Wiley-VCH Verlag GmbH & Co. KGaA: Weinheim, FRG, 2006.
(23) Soussan, L.; Pen, N.; Belleville, M. P.; Marcano, J. S.; Paolucci-Jeanjean, D. Alkane Biohydroxylation: Interests, Constraints and Future Developments. *J. Biotechnol.* **2016**, *222*, 117−142.
(24) Gunsalus, N. J.; Koppaka, A.; Park, S. H.; Bischof, S. M.; Hashiguchi, B. G.; Periana, R. A. Homogeneous Functionalization of Methane. *Chem. Rev.* **2017**, *117*, 8521−8573.
(25) Erb, T. J.; Jones, P. R.; Bar-Even, A. Synthetic Metabolism: Metabolic Engineering Meets Enzyme Design. *Curr. Opin. Chem. Biol.* **2017**, *37*, 56−62.
(26) Xiao, D. J.; Bloch, E. D.; Mason, J. A.; Queen, W. L.; Hudson, M. R.; Planas, N.; Borycz, J.; Dzubak, A. L.; Verma, P.; Lee, K.; et al. Oxidation of Ethane to Ethanol by N2O in a Metal−organic Framework with Coordinatively Unsaturated iron(II) Sites. *Nat. Chem.* **2014**, *6*, 590−595.
(27) Li, Z.; Peters, A. W.; Bernales, V.; Ortuño, M. A.; Schweitzer, N. M.; DeStefano, M. R.; Gallington, L. C.; Platero-Prats, A. E.; Chapman, K. W.; Cramer, C. J.; et al. Metal−Organic Framework Supported Cobalt Catalysts for the Oxidative Dehydrogenation of Propane at Low Temperature. *ACS Cent. Sci.* **2017**, *3*, 31−38.
(28) Herron, N. Zeolite Catalysts as Enzyme Mimics. Toward Silicon-Based Life? *Biocatal. Biomimetics* **1989**, *392*, 141−154.
(29) Xuereb, D. J.; Raja, R. Design Strategies for Engineering Selectivity in Bio-Inspired Heterogeneous Catalysts. *Catal. Sci. Technol.* **2011**, *1*, 517−534.
(30) Xuereb, D. J.; Dzierzak, J.; Raja, R. From Zeozymes to Bio-Inspired Heterogeneous Solids: Evolution of Design Strategies for Sustainable Catalysis. Catal. *Catal. Today* **2012**, *198*, 19−34.
(31) Srinivas, D.; Sivasanker, S. Ã. Biomimetic Oxidations Using Transition Metal Complexes Encapsulated in Zeolites. *Catal. Surv. Asia* **2003**, *7*, 121−132.
(32) Panov, G. I.; Sobolev, V. I.; Kharitonov, A. S. The Role of Iron in N2O Decomposition on ZSM-5 Zeolite and Reactivity of the Surface Oxygen Formed. *J. Mol. Catal.* **1990**, *61*, 85−97.
(33) Dubkov, K. A.; Sobolev, V. I.; Talsi, E. P.; Rodkin, M. A.; Watkins, N. H.; Shteinman, A. A.; Panov, G. I. Kinetic Isotope Effects and Mechanism of Biomimetic Oxidation of Methane and Benzene on FeZSM-5 Zeolite. *J. Mol. Catal. A: Chem.* **1997**, *123*, 155−161.
(34) Notté, P. P. The AlphOxTM Process or the One-step Hydroxylation of Benzene into Phenol by Nitrous Oxide. Understanding and Tuning the ZSM-5 Catalyst Activities. *Top. Catal.* **2000**, *13*, 387−394.
(35) Snyder, B. E. R.; Vanelderen, P.; Bols, M. L.; Hallaert, S. D.; Böttger, L. H.; Ungur, L.; Pierloot, K.; Schoonheydt, R. A.; Sels, B. F.; Solomon, E. I. The Active Site of Low-Temperature Methane Hydroxylation in Iron-Containing Zeolites. *Nature* **2016**, *536*, 317−321.
(36) Groothaert, M. H.; Smeets, P. J.; Sels, B. F.; Jacobs, P. A.; Schoonheydt, R. A. Selective Oxidation of Methane by the Bis(μ-Oxo)dicopper Core Stabilized on ZSM-5 and Mordenite Zeolites. *J. Am. Chem. Soc.* **2005**, *127*, 1394−1395.
(37) Woertink, J. S.; Smeets, P. J.; Groothaert, M. H.; Vance, M. A.; Sels, B. F.; Schoonheydt, R. A.; Solomon, E. I. A [Cu2O]2+ Core in Cu-ZSM-5, the Active Site in the Oxidation of Methane to Methanol. *Proc. Natl. Acad. Sci. U. S. A.* **2009**, *106*, 18908−18913.
(38) International Zeolite Association. *IZA Structure database*; http://europe.iza-structure.org/IZA-SC/ftc-table.php (accessed April 25, 2017).
(39) Gounaris, C. E.; First, E. L.; Wei, J.; Floudas, C. A.; Ranjan, R.; Tsapatsis, M. *ZEOMICS: Zeolites and Microporous Structures Characterization*; http://helios.princeton.edu/zeomics/ (accessed May 6, 2017).
(40) Dědeček, J.; Sobalík, Z.; Wichterlová, B. Siting and Distribution of Framework Aluminium Atoms in Silicon-Rich Zeolites and Impact on Catalysis. *Catal. Rev.: Sci. Eng.* **2012**, *54*, 135−223.
(41) Gábová, V.; Dědeček, J.; Čejka, J. Control of Al Distribution in ZSM-5 by Conditions of Zeolite Synthesis. *Chem. Commun.* **2003**, *10*, 1196−1197.
(42) Di Iorio, J. R.; Gounder, R. Controlling the Isolation and Pairing of Aluminum in Chabazite Zeolites Using Mixtures of Organic and Inorganic Structure-Directing Agents. *Chem. Mater.* **2016**, *28*, 2236−2247.
(43) Van Bokhoven, J. A.; Lee, T.-L.; Drakopoulos, M.; Lamberti, C.; Thieß, S.; Zegenhagen, J. Determining the Aluminium Occupancy on the Active T-Sites in Zeolites Using X-Ray Standing Waves. *Nat. Mater.* **2008**, *7*, 551−555.
(44) Mccusker, L. B.; Von Dreele, R. B.; Cox, D. E.; Louër, D.; Scardi, P. Rietveld Refnement Guidelines. *J. Appl. Crystallogr.* **1999**, *32*, 36−50.
(45) Rietveld, H. M. A. Profile Refinement Method for Nuclear and Magnetic Structures. *J. Appl. Crystallogr.* **1969**, *2*, 65−71.
(46) Papoular, R. J.; Cox, D. E. Model-Free Search for Extra-Framework Cations in Zeolites Using Powder Diffraction. *Europhys. Lett.* **1995**, *32*, 337−342.
(47) Dalconi, M. C.; Cruciani, G.; Alberti, A.; Ciambelli, P. Co- and Ni-Exchanged Ferrierite: The Contribution of Synchrotron X-Ray Diffraction Data to Siting of TMIs. Catal. *Catal. Today* **2005**, *110*, 345−350.
(48) Barrer, R. M. *Zeolites and Clay Minerals as Sorbents and Molecular Sieves*; Academic Press: London, 1978.
(49) Mortier, W.; Structure Commission of the International Zeolite Association. *Compilation of Extra Framework Sites in Zeolites*; Butterworth Scientific Ltd.: Leuven, 1982.
(50) Esemann, H.; Förster, H.; Geidel, E.; Krause, K. Exploring Cation Siting in Zeolite ZSM-5 by Infrared Spectroscopy, EXAFS and Computer Simulations. *Microporous Mater.* **1996**, *6*, 321−329.
(51) Dalconi, M. C.; Alberti, A.; Cruciani, G.; Ciambelli, P.; Fonda, E. Siting and Coordination of Cobalt in Ferrierite: XRD and EXAFS Studies at Different Co Loadings. *Microporous Mesoporous Mater.* **2003**, *62*, 191−200.
(52) Benco, L.; Bucko, T.; Hafner, J.; Toulhoat, H. Periodic DFT Calculations of the Stability of Al/Si Substitutions and Extraframework Zn^{2+} Cations in Mordenite and Reaction Pathway for the Dissociation of H2 and CH4. *J. Phys. Chem. B* **2005**, *109*, 20361−20369.
(53) Dědeček, J.; Kaucký, D.; Wichterlová, B. Co2+ Ion Siting in Pentasil-Containing Zeolites, Part 3.: Co2+ Ion Sites and Their Occupation in ZSM-5: A VIS Diffuse Reflectance Spectroscopy Study. *Microporous Mesoporous Mater.* **2000**, *35*−*36*, 483−494.
(54) Palagin, D.; Knorpp, A. J.; Pinar, A. B.; Ranocchiari, M.; van Bokhoven, J. A. Assessing the Relative Stability of Copper Oxide Clusters as Active Sites of a CuMOR Zeolite for Methane to Methanol Conversion: Size Matters? *Nanoscale* **2017**, *9*, 1144−1153.
(55) Grundner, S.; Markovits, M. A. C.; Li, G.; Tromp, M.; Pidko, E. A.; Hensen, E. J. M.; Jentys, A.; Sanchez-Sanchez, M.; Lercher, J. A. Single-Site Trinuclear Copper Oxygen Clusters in Mordenite for Selective Conversion of Methane to Methanol. *Nat. Commun.* **2015**, *6*, 7546.
(56) Battiston, A. A.; Bitter, J. H.; Koningsberger, D. C. Reactivity of Binuclear Fe Complexes in over-Exchanged Fe/ZSM5, Studied by in Situ XAFS Spectroscopy 2. Selective Catalytic Reduction of NO with Isobutane. *J. Catal.* **2003**, *218*, 163−177.
(57) Dubkov, K. A.; Ovanesyan, N. S.; Shteinman, A. A.; Starokon, E. V.; Panov, G. I. Evolution of Iron States and Formation of α-Sites upon Activation of FeZSM-5 Zeolites. *J. Catal.* **2002**, *207*, 341−352.
(58) Jíša, K.; Nováková, J.; Schwarze, M.; Vondrová, A.; Sklenák, S.; Sobalik, Z. Role of the Fe-Zeolite Structure and Iron State in the N2O Decomposition: Comparison of Fe-FER, Fe-BEA, and Fe-MFI Catalysts. *J. Catal.* **2009**, *262*, 27−34.
(59) Iwamoto, M.; Yahiro, H.; Tanda, K.; Mizuno, N.; Mine, Y.; Kagawa, S. Removal of Nitrogen Monoxide through a Novel Catalytic

DOI: 10.1021/acs.chemrev.7b00344
Chem. Rev. 2018, 118, 2718−2768

Process. 1. Decomposition on Excessively Copper-Ion-Exchanged ZSM-5 Zeolites. *J. Phys. Chem.* **1991**, *95*, 3727−3730.
(60) Occhiuzzi, M.; Fierro, G.; Ferraris, G.; Moretti, G. Unusual Complete Reduction of Cu2+ Species in Cu-ZSM-5 Zeolites under Vacuum Treatment at High Temperature. *Chem. Mater.* **2012**, *24*, 2022−2031.
(61) Larsen, S. C.; Aylor, A.; Bell, A. T.; Reimer, J. A. Electron Paramagnetic Resonance Studies of Copper Ion-Exchanged ZSM-5. *J. Phys. Chem.* **1994**, *98*, 11533−11540.
(62) Jacobs, P. A.; Beyer, H. K. Evidence for the Nature of True Lewis Sites in Faujasite-Type Zeolites. *J. Phys. Chem.* **1979**, *83*, 1174−1177.
(63) Vanelderen, P.; Vancauwenbergh, J.; Tsai, M.-L.; Hadt, R. G.; Solomon, E. I.; Schoonheydt, R. A.; Sels, B. F. Spectroscopy and Redox Chemistry of Copper in Mordenite. *ChemPhysChem* **2014**, *15*, 91−99.
(64) Moretti, G.; Ferraris, G.; Fierro, G.; Jacono, M. Lo; Morpurgo, S.; Faticanti, M. Dimeric Cu(I) Species in Cu-ZSM-5 Catalysts: The Active Sites for the NO Decomposition. *J. Catal.* **2005**, *232*, 476−487.
(65) Groothaert, M. H.; Lievens, K.; Leeman, H.; Weckhuysen, B. M.; Schoonheydt, R. A. An Operando Optical Fiber UV−vis Spectroscopic Study of the Catalytic Decomposition of NO and N2O over Cu-ZSM-5. *J. Catal.* **2003**, *220*, 500−512.
(66) Smeets, P. J.; Groothaert, M. H.; Schoonheydt, R. A. Cu Based Zeolites: A UV−vis Study of the Active Site in the Selective Methane Oxidation at Low Temperatures. *Catal. Today* **2005**, *110*, 303−309.
(67) Markovits, M. A. C.; Jentys, A.; Tromp, M.; Sanchez-Sanchez, M.; Lercher, J. A. Effect of Location and Distribution of Al Sites in ZSM-5 on the Formation of Cu-Oxo Clusters Active for Direct Conversion of Methane to Methanol. *Top. Catal.* **2016**, *59*, 1554−1563.
(68) Dědeček, J.; Kaucký, D.; Wichterlová, B.; Gonsiorová, O. Co(II) Ions as Probes of Al Distribution in the Framework of Zeolites. ZSM-5 Study. *Phys. Chem. Chem. Phys.* **2002**, *4*, 5406−5413.
(69) Sazama, P.; Dědeček, J.; Gábová, V.; Wichterlová, B.; Spoto, G.; Bordiga, S. Effect of Aluminium Distribution in the Framework of ZSM-5 on Hydrocarbon Transformation. Cracking of 1-Butene. *J. Catal.* **2008**, *254*, 180−189.
(70) Gao, F.; Walter, E. D.; Kollar, M.; Wang, Y.; Szanyi, J.; Peden, C. H. F. Understanding Ammonia Selective Catalytic Reduction Kinetics over Cu/SSZ-13 from Motion of the Cu Ions. *J. Catal.* **2014**, *319*, 1−14.
(71) Paolucci, C.; Parekh, A. A.; Khurana, I.; Di Iorio, J. R.; Li, H.; Albarracin Caballero, J. D.; Shih, A. J.; Anggara, T.; Delgass, W. N.; Miller, J. T.; et al. Catalysis in a Cage: Condition-Dependent Speciation and Dynamics of Exchanged Cu Cations in SSZ-13 Zeolites. *J. Am. Chem. Soc.* **2016**, *138*, 6028−6048.
(72) Borfecchia, E.; Lomachenko, K. A.; Giordanino, F.; Falsig, H.; Beato, P.; Soldatov, A. V.; Bordiga, S.; Lamberti, C. Revisiting the Nature of Cu Sites in the Activated Cu-SSZ-13 Catalyst for SCR Reaction. *Chem. Sci.* **2015**, *6*, 548−563.
(73) Zhao, Z.-J.; Kulkarni, A.; Vilella, L.; Nørskov, J. K.; Studt, F. Theoretical Insights into the Selective Oxidation of Methane to Methanol in Copper-Exchanged Mordenite. *ACS Catal.* **2016**, *6*, 3760−3766.
(74) Kulkarni, A. R.; Zhao, Z.-J.; Siahrostami, S.; Nørskov, J. K.; Studt, F. Monocopper Active Site for Partial Methane Oxidation in Cu-Exchanged 8MR Zeolites. *ACS Catal.* **2016**, *6*, 6531−6536.
(75) Kwak, J. H.; Varga, T.; Peden, C. H. F.; Gao, F.; Hanson, J. C.; Szanyi, J. Following the Movement of Cu Ions in a SSZ-13 Zeolite during Dehydration, Reduction and Adsorption: A Combined in Situ TP-XRD, XANES/DRIFTS Study. *J. Catal.* **2014**, *314*, 83−93.
(76) Giordanino, F.; Vennestrøm, P. N. R.; Lundegaard, L. F.; Stappen, F. N.; Mossin, S.; Beato, P.; Bordiga, S.; Lamberti, C. Characterization of Cu-Exchanged SSZ-13: A Comparative FTIR, UV-Vis, and EPR Study with Cu-ZSM-5 and Cu-β with Similar Si/Al and Cu/Al Ratios. *Dalt. Trans.* **2013**, *42*, 12741−12761.
(77) Grundner, S.; Luo, W.; Sanchez-Sanchez, M.; Lercher, J. Synthesis of Single-Site Copper Catalysts for Methane Partial Oxidation. *Chem. Commun.* **2016**, *52*, 2553−2556.
(78) Narsimhan, K.; Michaelis, V. K.; Mathies, G.; Gunther, W. R.; Griffin, R. G.; Román-Leshkov, Y. Methane to Acetic Acid over Cu-Exchanged Zeolites: Mechanistic Insights from a Site-Specific Carbonylation Reaction. *J. Am. Chem. Soc.* **2015**, *137*, 1825−1832.
(79) Li, G.; Vassilev, P.; Sanchez-Sanchez, M.; Lercher, J. A.; Hensen, E. J. M.; Pidko, E. A. Stability and Reactivity of Copper Oxo-Clusters in ZSM-5 Zeolite for Selective Methane Oxidation to Methanol. *J. Catal.* **2016**, *338*, 305−312.
(80) Veefkind, V. A.; Smidt, M. L.; Lercher, J. A. On the Role of Strength and Location of Brønsted Acid Sites for Ethylamine Synthesis on Mordenite Catalysts. *Appl. Catal., A* **2000**, *194−195*, 319−332.
(81) Mortier, W. J.; Schoonheydt, R. A. Surface and Solid State Chemistry of Zeolites. *Prog. Solid State Chem.* **1985**, *16*, 1−125.
(82) Baekelandt, B. G.; Mortier, W.; Schoonheydt, R. *Structural Chemistry of Zeolites : Solid State Electronegativity and Sensitivity Analysis*; Catlow, R. A., Ed.; Academic Press: London, 1992.
(83) De Tavernier, S. G.; Schoonheydt, R. A.; Mortier, W. J. *Zeolites for the Nineties: Recent Progress Reports on the 8th International Zeolite Conference*; Elsevier: Amsterdam, 1989.
(84) Wulfers, M. J.; Teketel, S.; Ipek, B.; Lobo, R. F. Conversion of Methane to Methanol on Copper-Containing Small-Pore Zeolites and Zeotypes. *Chem. Commun.* **2015**, *51*, 4447−4450.
(85) Zecchina, A.; Rivallan, M.; Berlier, G.; Lamberti, C.; Ricchiardi, G. Structure and Nuclearity of Active Sites in Fe-Zeolites: Comparison with Iron Sites in Enzymes and Homogeneous Catalysts. *Phys. Chem. Chem. Phys.* **2007**, *9*, 3483−3499.
(86) Mauvezin, M.; Delahay, G.; Coq, B.; Kieger, S.; Jumas, J. C.; Olivier-Fourcade, J. Identification of Iron Species in Fe-BEA: Influence of the Exchange Level. *J. Phys. Chem. B* **2001**, *105*, 928−935.
(87) Lobree, L. J.; Hwang, I.-C.; Reimer, J. A.; Bell, A. T. Investigations of the State of Fe in H−ZSM-5. *J. Catal.* **1999**, *186*, 242−253.
(88) Panov, G. I.; Uriarte, A. K.; Rodkin, M. A.; Sobolev, V. I. Generation of Active Oxygen Species on Solid Surfaces. Opportunity for Novel Oxidation Technologies over Zeolites. *Catal. Today* **1998**, *41*, 365−385.
(89) Marturano, P.; Drozdová, L.; Pirngruber, G. D.; Kogelbauer, A.; Prins, R. The Mechanism of Formation of the Fe Species in Fe/ZSM-5 Prepared by CVD. *Phys. Chem. Chem. Phys.* **2001**, *3*, 5585−5595.
(90) Chen, H.-Y.; Sachtler, W. M. Activity and Durability of Fe/ZSM-5 Catalysts for Lean Burn NOx Reduction in the Presence of Water Vapor. *Catal. Today* **1998**, *42*, 73−83.
(91) Voskoboinikov, T. V.; Chen, H.-Y.; Sachtler, W. M. On the Nature of Active Sites in Fe/ZSM-5 Catalysts for NOx Abatement. *Appl. Catal., B* **1998**, *19*, 279−287.
(92) Hammond, C.; Forde, M. M.; Ab Rahim, M. H.; Thetford, A.; He, Q.; Jenkins, R. L.; Dimitratos, N.; Lopez-Sanchez, J. A.; Dummer, N. F.; Murphy, D. M.; et al. Direct Catalytic Conversion of Methane to Methanol in an Aqueous Medium by Using Copper-Promoted Fe-ZSM-5. *Angew. Chem., Int. Ed.* **2012**, *51*, 5129−5133.
(93) Hammond, C.; Hermans, I.; Dimitratos, N. Biomimetic Oxidation with Fe-ZSM-5 and H2O2? Identification of an Active, Extra-Framework Binuclear Core and an Fe(III)OOH Intermediate with Resonance-Enhanced Raman Spectroscopy. *ChemCatChem* **2015**, *7*, 434−440.
(94) Xia, H.; Sun, K.; Sun, K.; Feng, Z.; Li, W. X.; Li, C. Direct Spectroscopic Observation of Fe(III)−Phenolate Complex Formed From the Reaction of Benzene With Peroxide Species on Fe/ZSM-5 At Room Temperature. *J. Phys. Chem. C* **2008**, *112*, 9001−9005.
(95) Gao, Z.-X.; Kim, H.-S.; Sun, Q.; Stair, P. C.; Sachtler, W. M. H. UV− Raman Characterization of Iron Peroxo Adsorbates on Fe/MFI Catalyst with High Activity for NO X Reduction. *J. Phys. Chem. B* **2001**, *105*, 6186−6190.
(96) Klier, K.; Hutta, P. J.; Kellerman, R. Electronic Structure and Stability of Transition Metal Ions in Zeolites. In *Molecular Sieves—II*; Webster: New York, 1977; pp 108−119.

DOI: 10.1021/acs.chemrev.7b00344
Chem. Rev. 2018, 118, 2718−2768

(97) Klier, K.; Kellerman, R.; Hutta, P. J. Spectra of Synthetic Zeolites Containing Transition Metal Ions. V.* Π Complexes of Olefins and Acetylene with Co(II)A Molecular Sieve. *J. Chem. Phys.* **1974**, *61*, 4224−4234.
(98) Schoonheydt, R. A. Transition Metal Ions in Zeolites: Siting and Energetics of Cu2+. *Catal. Rev.: Sci. Eng.* **1993**, *35*, 129−168.
(99) Delabie, A.; Pierloot, K.; Groothaert, M. H.; Weckhuysen, B. M.; Schoonheydt, R. A. The Siting of Cu(II) in Mordenite: A Theoretical Spectroscopic Study. *Phys. Chem. Chem. Phys.* **2002**, *4*, 134−145.
(100) Pierloot, K.; Delabie, A.; Groothaert, M. H.; Schoonheydt, R. A. A Reinterpretation of the EPR Spectra of Cu(II) in Zeolites A, Y and ZK4, Based on Ab Initio Cluster Model Calculations. *Phys. Chem. Chem. Phys.* **2001**, *3*, 2174−2183.
(101) Groothaert, M. H.; Pierloot, K.; Delabie, A.; Schoonheydt, R. A. Identification of Cu(ii) Coordination Structures in Cu-ZSM-5, Based on a DFT/ab Initio Assignment of the EPR Spectra. *Phys. Chem. Chem. Phys.* **2003**, *5*, 2135−2144.
(102) Delabie, A.; Pierloot, K.; Groothaert, M. H.; Schoonheydt, R. A.; Vanquickenborne, L. G. The Coordination of CuII in Zeolites − Structure and Spectroscopic Properties. *Eur. J. Inorg. Chem.* **2002**, *2002*, 515−530.
(103) Mignon, P.; Pidko, E. A.; Van Santen, R. A.; Geerlings, P.; Schoonheydt, R. A. Understanding the Reactivity and Basicity of Zeolites: A Periodic DFT Study of the Disproportionation of N2O4 on Alkali-Cation-Exchanged Zeolite Y. *Chem. - Eur. J.* **2008**, *14*, 5168−5177.
(104) Pidko, E. A.; Mignon, P.; Geerlings, P.; Schoonheydt, R. A.; van Santen, R. A. A Periodic DFT Study of N2O4 Disproportionation on Alkali-Exchanged Zeolites X. *J. Phys. Chem. C* **2008**, *112*, 5510−5519.
(105) Schoonheydt, R. A.; Geerlings, P.; Pidko, E. A.; van Santen, R. A. The Framework Basicity of Zeolites. *J. Mater. Chem.* **2012**, *22*, 18705.
(106) Hammond, C. Intensification Studies of Heterogeneous Catalysts: Probing and Overcoming Catalyst Deactivation during Liquid Phase Operation. *Green Chem.* **2017**, *19*, 2711−2728.
(107) Solomon, E. I.; Hodgson, K. O. *Spectroscopic Methods in Bioinorganic Chemistry*; American Chemical Society: Washington, DC, 1998.
(108) Weltner, W. *Magnetic Atoms and Molecules*; Courier Corp.: Mineola, NY, 1989.
(109) Kahn, O. *Molecular Magnetism*; VCH Publishers: New York, 1993.
(110) Abragam, A.; Bleaney, B. *Electron Paramagnetic Resonance of Transition Ions*; OUP Oxford: 2012.
(111) Ballhausen, C. J.; Weiner, M. A. Introduction to Ligand Field Theory. *J. Electrochem. Soc.* **1963**, *110*, 97C−97C.
(112) Hoffman, B. M. ENDOR of Metalloenzymes. *Acc. Chem. Res.* **2003**, *36*, 522−529.
(113) Campochiaro, C.; Pavel, E. G.; Solomon, E. I. Saturation Magnetization Magnetic Circular-Dichroism Spectroscopy of Systems with Positive Zero-Field Splittings-Application to Fesif6-Center-Dot-6H (2). *Inorg. Chem.* **1995**, *34*, 4669−4675.
(114) Levy, P. M. Antisymmetric Exchange. *Phys. Rev. Lett.* **1968**, *20*, 1366−1370.
(115) Bencini, A.; Gatteschi, D. *Electron Paramagnetic Resonance of Exchange Coupled Systems*; Springer Science & Business Media: Mineola, NY, 2012.
(116) Solomon, E. I.; Pavel, E. G.; Loeb, K. E.; Campochiaro, C. Magnetic Circular Dichroism Spectroscopy as a Probe of the Geometric and Electronic Structure of Non-Heme Ferrous Enzymes. *Coord. Chem. Rev.* **1995**, *144*, 369−460.
(117) Solomon, E. I. Spectroscopic Methods in Bioinorganic Chemistry: Blue to Green to Red Copper Sites. *Inorg. Chem.* **2006**, *45*, 8012−8025.
(118) Vallee, B. L.; Williams, R. J. Metalloenzymes: The Entatic Nature of Their Active Sites. *Proc. Natl. Acad. Sci. U. S. A.* **1968**, *59*, 498−505.
(119) Solomon, E. I.; Scott, R. A.; King, R. B.; Lever, A. B. P.; Leznoff, C. C.; Schmidbauer, H.; Lee, J. D.; Moorhouse, J.; Karlin, K. D.; Zhai, T. *Inorganic Electronic Structure and Spectroscopy, Vol. I: Methodology*; Wiley Interscience: Hoboken, NJ, 2006.
(120) Tang, J.; Albrecht, A. C. Developments in the Theories of Vibrational Raman Intensities. In *Raman Spectroscopy*; Springer: 1970; pp 33−68.
(121) Ghosh, S.; Xie, X.; Dey, A.; Sun, Y.; Scholes, C. P.; Solomon, E. I. Thermodynamic Equilibrium between Blue and Green Copper Sites and the Role of the Protein in Controlling Function. *Proc. Natl. Acad. Sci. U. S. A.* **2009**, *106*, 4969−4974.
(122) Neese, F.; Solomon, E. I. MCD C-Term Signs, Saturation Behavior, and Determination of Band Polarizations in Randomly Oriented Systems with Spin S≥ 1/2. Applications to S= 1/2 and S= 5/2. *Inorg. Chem.* **1999**, *38*, 1847−1865.
(123) Piepho, S. B.; Schatz, P. N. *Group Theory in Spectroscopy: With Applications to Magnetic Circular Dichroism*; Wiley-Interscience Monographs in Chemical Physics; Wiley: Hoboken, 1983.
(124) Schatz, P. N.; Mowery, R. L.; Krausz, E. R. MCD/MCPL Saturation Theory with Application to Molecules in D∞ H and Its Subgroups. *Mol. Phys.* **1978**, *35*, 1537−1557.
(125) Stephens, P. J. Magnetic Circular Dichroism. *Adv. Chem. Phys.* **1976**, *35*, 197−264.
(126) Whittaker, J. W.; Solomon, E. I. Spectroscopic Studies on Ferrous Non-Heme Iron Active Sites: Magnetic Circular Dichroism of Mononuclear Fe Sites in Superoxide Dismutase and Lipoxygenase. *J. Am. Chem. Soc.* **1988**, *110*, 5329−5339.
(127) Münck, E.; Ksurerus, K.; Hendrich, M. P. [17] Combining Mössbauer Spectroscopy with Integer Spin Electron Paramagnetic Resonance. *Methods Enzymol.* **1993**, *227*, 463−479.
(128) Hendrich, M. P.; Debrunner, P. G. Integer-Spin Electron Paramagnetic Resonance of Iron Proteins. *Biophys. J.* **1989**, *56*, 489−506.
(129) Sturhahn, W.; Toellner, T. S.; Alp, E. E.; Zhang, X.; Ando, M.; Yoda, Y.; Kikuta, S.; Seto, M.; Kimball, C. W.; Dabrowski, B. Phonon Density of States Measured by Inelastic Nuclear Resonant Scattering. *Phys. Rev. Lett.* **1995**, *74*, 3832−3835.
(130) Scheidt, W. R.; Durbin, S. M.; Sage, J. T. Nuclear Resonance Vibrational spectroscopy−NRVS. *J. Inorg. Biochem.* **2005**, *99*, 60−71.
(131) Wong, S. D.; Srnec, M.; Matthews, M. L.; Liu, L. V.; Kwak, Y.; Park, K.; Bell, C. B., III; Alp, E. E.; Zhao, J.; Yoda, Y.; et al. Elucidation of the Fe(IV)=O Intermediate in the Catalytic Cycle of the Halogenase SyrB2. *Nature* **2013**, *499*, 320−323.
(132) Wong, S. D.; Bell, C. B.; Liu, L. V.; Kwak, Y.; England, J.; Alp, E. E.; Zhao, J.; Que, L.; Solomon, E. I. Nuclear Resonance Vibrational Spectroscopy on the FeIV═O S= 2 Non-Heme Site in TMG3tren: Experimentally Calibrated Insights into Reactivity. *Angew. Chem., Int. Ed.* **2011**, *50*, 3215−3218.
(133) Bell, C. B.; Wong, S. D.; Xiao, Y.; Klinker, E. J.; Tenderholt, A. L.; Smith, M. C.; Rohde, J.; Que, L.; Cramer, S. P.; Solomon, E. I. A Combined NRVS and DFT Study of FeIV = O Model Complexes: A Diagnostic Method for the Elucidation of Non-Heme Iron Enzyme Intermediates. *Angew. Chem., Int. Ed.* **2008**, *47*, 9071−9074.
(134) Vanelderen, P.; Snyder, B. E. R.; Tsai, M.-L.; Hadt, R. G.; Vancauwenbergh, J.; Coussens, O.; Schoonheydt, R. A.; Sels, B. F.; Solomon, E. I. Spectroscopic Definition of the Copper Active Sites in Mordenite: Selective Methane Oxidation. *J. Am. Chem. Soc.* **2015**, *137*, 6383−6392.
(135) Tsai, M.-L.; Hadt, R. G.; Vanelderen, P.; Sels, B. F.; Schoonheydt, R. A.; Solomon, E. I. [Cu2O]2+ Active Site Formation in Cu−ZSM-5: Geometric and Electronic Structure Requirements for N2O Activation. *J. Am. Chem. Soc.* **2014**, *136*, 3522−3529.
(136) Smeets, P. J.; Hadt, R. G.; Woertink, J. S.; Vanelderen, P.; Schoonheydt, R. A.; Sels, B. F.; Solomon, E. I. Oxygen Precursor to the Reactive Intermediate in Methanol Synthesis by Cu-ZSM-5. *J. Am. Chem. Soc.* **2010**, *132*, 14736−14738.
(137) Henson, M. J.; Mukherjee, P.; Root, D. E.; Stack, T. D. P.; Solomon, E. I. Spectroscopic and Electronic Structural Studies of the

DOI: 10.1021/acs.chemrev.7b00344
Chem. Rev. 2018, 118, 2718−2768

Cu (III) 2 Bis-μ-Oxo Core and Its Relation to the Side-on Peroxo-Bridged Dimer. *J. Am. Chem. Soc.* **1999**, *121*, 10332−10345.
(138) Mahapatra, S.; Halfen, J. A.; Wilkinson, E. C.; Pan, G.; Cramer, C. J.; Que, L. J.; Tolman, W. B. A New Intermediate in Copper Dioxygen Chemistry: Breaking the OO Bond To Form a {Cu2 (. Mu.-O) 2} 2+ Core. *J. Am. Chem. Soc.* **1995**, *117*, 8865−8866.
(139) Maiti, D.; Fry, H. C.; Woertink, J. S.; Vance, M. A.; Solomon, E. I.; Karlin, K. D. A 1:1 Copper− Dioxygen Adduct Is an End-on Bound Superoxo Copper (II) Complex Which Undergoes Oxygenation Reactions with Phenols. *J. Am. Chem. Soc.* **2007**, *129*, 264−265.
(140) Chen, P.; Root, D. E.; Campochiaro, C.; Fujisawa, K.; Solomon, E. I. Spectroscopic and Electronic Structure Studies of the Diamagnetic Side-On CuII-Superoxo Complex Cu (O2)[HB (3-R-5-I Prpz) 3]: Antiferromagnetic Coupling versus Covalent Delocalization. *J. Am. Chem. Soc.* **2003**, *125*, 466−474.
(141) Chen, P.; Fujisawa, K.; Solomon, E. I. Spectroscopic and Theoretical Studies of Mononuclear Copper (II) Alkyl-and Hydroperoxo Complexes: Electronic Structure Contributions to Reactivity. *J. Am. Chem. Soc.* **2000**, *122*, 10177−10193.
(142) Czernuszewicz, R. S.; Sheats, J. E.; Spiro, T. G. Resonance Raman Spectra and Excitation Profile for Bis (Acetato) Bis (Hydrotripyrazolylborato) Oxodiiron, a Hemerythrin Analog. *Inorg. Chem.* **1987**, *26*, 2063−2067.
(143) Mentzen, B. F.; Bergeret, G. Crystallographic Determination of the Positions of the Copper Cations in Zeolite MFI. *J. Phys. Chem. C* **2007**, *111*, 12512−12516.
(144) Pieterse, J. A. Z.; Pirngruber, G. D.; van Bokhoven, J. A.; Booneveld, S. Hydrothermal Stability of Fe-ZSM-5 and Fe-BEA Prepared by Wet Ion-Exchange for N 2 O Decomposition. *Appl. Catal., B* **2007**, *71*, 16−22.
(145) Nováková, J.; Schwarze, M.; Sobalík, Z. Role of Zeolitic Oxygens During the Decomposition of 15 N. *Catal. Lett.* **2005**, *104*, 157−162.
(146) Fu, C. M.; Korchak, V. N.; Hall, W. K. Decomposition of Nitrous Oxide on FeY Zeolite. *J. Catal.* **1981**, *68*, 166−171.
(147) Corma, A.; García, H. Lewis Acids as Catalysts in Oxidation Reactions: From Homogeneous to Heterogeneous Systems. *Chem. Rev.* **2002**, *102*, 3837−3892.
(148) García, H.; Roth, H. D. Generation and Reactions of Organic Radical Cations in Zeolites. *Chem. Rev.* **2002**, *102*, 3947−4008.
(149) Yoon, K. B. Electron-and Charge-Transfer Reactions within Zeolites. *Chem. Rev.* **1993**, *93*, 321−339.
(150) Ipek, B.; Wulfers, M. J.; Kim, H.; Göltl, F.; Hermans, I.; Smith, J. P.; Booksh, K. S.; Brown, C. M.; Lobo, R. F. Formation of [Cu2O2]2+ and [Cu2O]2+ toward C-H Bond Activation in Cu-SSZ-13 and Cu-SSZ-39. *ACS Catal.* **2017**, *7*, 4291−4303.
(151) Johnston, E. M.; Carreira, C.; Dell'Acqua, S.; Dey, S. G.; Pauleta, S. R.; Moura, I.; Solomon, E. I. Spectroscopic Definition of the CuZ° Intermediate in Turnover of Nitrous Oxide Reductase and Molecular Insight into the Catalytic Mechanism. *J. Am. Chem. Soc.* **2017**, *139*, 4462−4476.
(152) Ipek, B.; Lobo, R. F. Catalytic Conversion of Methane to Methanol on Cu-SSZ-13 Using N2O as Oxidant. *Chem. Commun.* **2016**, *52*, 13401−13404.
(153) Sheppard, T.; Daly, H.; Goguet, A.; Thompson, J. M. Improved Efficiency for Partial Oxidation of Methane by Controlled Copper Deposition on Surface-Modified ZSM-5. *ChemCatChem* **2016**, *8*, 562−570.
(154) Narsimhan, K.; Iyoki, K.; Dinh, K.; Román-Leshkov, Y. Catalytic Oxidation of Methane into Methanol over Copper-Exchanged Zeolites with Oxygen at Low Temperature. *ACS Cent. Sci.* **2016**, *2*, 424−429.
(155) Tomkins, P.; Mansouri, A.; Bozbag, S. E.; Krumeich, F.; Park, M. B.; Alayon, E. M. C.; Ranocchiari, M.; van Bokhoven, J. A. Isothermal Cyclic Conversion of Methane into Methanol over Copper-Exchanged Zeolite at Low Temperature. *Angew. Chem., Int. Ed.* **2016**, *55*, 5467−5471.
(156) Sushkevich, V. L.; Palagin, D.; Ranocchiari, M.; van Bokhoven, J. A. Selective Anaerobic Oxidation of Methane Enables Direct Synthesis of Methanol. *Science* **2017**, *356*, 523−527.
(157) Tomkins, P.; Ranocchiari, M.; van Bokhoven, J. A. Direct Conversion of Methane to Methanol under Mild Conditions over Cu-Zeolites and beyond. *Acc. Chem. Res.* **2017**, *50*, 418−425.
(158) Anufrienko, V. F.; Bulgakov, N. N.; Vasenin, N. T.; Yashnik, S. A.; Tsikoza, L. T.; Vosel', S. V.; Ismagilov, Z. R. Detection of O− Radical Anions in Cu-ZSM-5 Zeolites after Heat Treatment. *Dokl. Chem.* **2002**, *386*, 273−276.
(159) Yashnik, S. A.; Ismagilov, Z. R.; Anufrienko, V. F. Catalytic Properties and Electronic Structure of Copper Ions in Cu-ZSM-5. *Catal. Today* **2005**, *110*, 310−322.
(160) Himes, R. A.; Barnese, K.; Karlin, K. D. One Is Lonely and Three Is a Crowd: Two Coppers Are for Methane Oxidation. *Angew. Chem., Int. Ed.* **2010**, *49*, 6714−6716.
(161) Lieberman, R. L.; Rosenzweig, A. C. Crystal Structure of a Membrane-Bound Metalloenzyme That Catalyses the Biological Oxidation of Methane. *Nature* **2005**, *434*, 177−182.
(162) Balasubramanian, R.; Smith, S. M.; Rawat, S.; Yatsunyk, L. A.; Stemmler, T. L.; Rosenzweig, A. C. Oxidation of Methane by a Biological Dicopper Centre. *Nature* **2010**, *465*, 115−119.
(163) Chan, S. I.; Chen, K. H. C.; Yu, S. S. F.; Chen, C. L.; Kuo, S. S. J. Toward Delineating the Structure and Function of the Particulate Methane Monooxygenase from Methanotrophic Bacteria. *Biochemistry* **2004**, *43*, 4421−4430.
(164) Ng, K.-Y.; Tu, L.-C.; Wang, Y.-S.; Chan, S. I.; Yu, S. S. F. Probing the Hydrophobic Pocket of the Active Site in the Particulate Methane Monooxygenase (pMMO) from Methylococcus Capsulatus (Bath) by Variable Stereoselective Alkane Hydroxylation and Olefin Epoxidation. *ChemBioChem* **2008**, *9*, 1116−1123.
(165) Chan, S. I.; Wang, V. C. C.; Lai, J. C. H.; Yu, S. S. F.; Chen, P. P. Y.; Chen, K. H. C.; Chen, C.-L.; Chan, M. K. Redox Potentiometry Studies of Particulate Methane Monooxygenase: Support for a Trinuclear Copper Cluster Active Site. *Angew. Chem., Int. Ed.* **2007**, *46*, 1992−1994.
(166) Chan, S. I.; Lu, Y.-J.; Nagababu, P.; Maji, S.; Hung, M.-C.; Lee, M. M.; Hsu, I.-J.; Minh, P. D.; Lai, J. C.-H.; Ng, K. Y.; et al. Efficient Oxidation of Methane to Methanol by Dioxygen Mediated by Tricopper Clusters. *Angew. Chem., Int. Ed.* **2013**, *52*, 3731−3735.
(167) Fierro, G.; Ferraris, G.; Moretti, G. CuO Nanoparticles Entrapped in MFI Framework: Investigation of Textural, Magnetic and Catalytic Properties of Cu-ZSM-5 and Cu-S-1 Catalysts. *Appl. Catal., B* **2009**, *91*, 499−506.
(168) Verma, A. A.; Bates, S. A.; Anggara, T.; Paolucci, C.; Parekh, A. A.; Kamasamudram, K.; Yezerets, A.; Miller, J. T.; Delgass, W. N.; Schneider, W. F.; et al. NO Oxidation: A Probe Reaction on Cu-SSZ-13. *J. Catal.* **2014**, *312*, 179−190.
(169) Roudesly, F.; Oble, J.; Poli, G. Metal-Catalyzed CH Activation/functionalization: The Fundamentals. *J. Mol. Catal. A: Chem.* **2017**, *426*, 275−296.
(170) Groves, J. T. Key Elements of the Chemistry of Cytochrome P-450: The Oxygen Rebound Mechanism. *J. Chem. Educ.* **1985**, *62*, 928.
(171) Mahyuddin, M. H.; Staykov, A.; Shiota, Y.; Miyanishi, M.; Yoshizawa, K. Roles of Zeolite Confinement and Cu−O−Cu Angle on the Direct Conversion of Methane to Methanol by [Cu2(μ-O)]2+ -Exchanged AEI, CHA, AFX, and MFI Zeolites. *ACS Catal.* **2017**, *7*, 3741−3751.
(172) Varghese, J. J.; Trinh, Q. T.; Mushrif, S. H. Insights into the Synergistic Role of Metal−lattice Oxygen Site Pairs in Four-Centered C−H Bond Activation of Methane: The Case of CuO. *Catal. Sci. Technol.* **2016**, *6*, 3984−3996.
(173) Alayon, E. M.; Nachtegaal, M.; Ranocchiari, M.; van Bokhoven, J. A. Catalytic Conversion of Methane to Methanol over Cu−mordenite. *Chem. Commun.* **2012**, *48*, 404−406.
(174) Donoghue, P. J.; Tehranchi, J.; Cramer, C. J.; Sarangi, R.; Solomon, E. I.; Tolman, W. B. Rapid C−H Bond Activation by a Monocopper(III)−Hydroxide Complex. *J. Am. Chem. Soc.* **2011**, *133*, 17602−17605.

DOI: 10.1021/acs.chemrev.7b00344
Chem. Rev. 2018, 118, 2718−2768

(175) Yin, G.; Danby, A. M.; Kitko, D.; Carter, J. D.; Scheper, W. M.; Busch, D. H. Understanding the Selectivity of a Moderate Oxidation Catalyst: Hydrogen Abstraction by a Fully Characterized, Activated Catalyst, the Robust Dihydroxo Manganese(IV) Complex of a Bridged Cyclam. *J. Am. Chem. Soc.* **2007**, *129*, 1512−1513.
(176) Yin, G.; Danby, A. M.; Kitko, D.; Carter, J. D.; Scheper, W. M.; Busch, D. H. Oxidative Reactivity Difference among the Metal Oxo and Metal Hydroxo Moieties: pH Dependent Hydrogen Abstraction by a Manganese(IV) Complex Having Two Hydroxide Ligands. *J. Am. Chem. Soc.* **2008**, *130*, 16245−16253.
(177) Rezabal, E.; Ruipérez, F.; Ugalde, J. M. Quantum Chemical Study of the Catalytic Activation of Methane by Copper Oxide and Copper Hydroxide Cations. *Phys. Chem. Chem. Phys.* **2013**, *15*, 1148−1153.
(178) Rosa, A.; Ricciardi, G.; Baerends, E. J. Is [FeO] 2+ the Active Center Also in Iron Containing Zeolites? A Density Functional Theory Study of Methane Hydroxylation Catalysis by Fe-ZSM-5 Zeolite. *Inorg. Chem.* **2010**, *49*, 3866−3880.
(179) Dubkov, K. A.; Sobolev, V. I.; Panov, G. I. Low-Temperature Oxidation of Methane to Methanol on FeZSM-5 Zeolite. *Kinet. Catal.* **1998**, *39*, 72−79.
(180) Ovanesyan, N. S.; Shteinman, A. A.; Dubkov, K. A.; Sobolev, V. I.; Panov, G. I. The State of Iron in the Fe-ZSM-5-N2O System for Selective Oxidation of Methane to Methanol from Data of Mössbauer Spectroscopy. *Kinet. Catal.* **1998**, *39*, 792−797.
(181) Panov, G. I. Advances in Oxidation Catalysis; Oxidation of Benzene to Phenol by Nutrous Oxide. *CATTECH* **2000**, *4*, 18−31.
(182) Centi, G.; Genovese, C.; Giordano, G.; Katovic, A.; Perathoner, S. Performance of Fe-BEA Catalysts for the Selective Hydroxylation of Benzene with N2O. *Catal. Today* **2004**, *91−92*, 17−26.
(183) Smeets, P. J.; Woertink, J. S.; Sels, B. F.; Solomon, E. I.; Schoonheydt, R. A. Transition-Metal Ions in Zeolites: Coordination and Activation of Oxygen. *Inorg. Chem.* **2010**, *49*, 3573−3583.
(184) Hammond, C.; Dimitratos, N.; Jenkins, R. L.; Lopez-sanchez, J. A.; Kondrat, S. A.; Hasbi ab Rahim, M.; Forde, M. M.; Thetford, A.; Taylor, S. H.; Hagen, H.; et al. Elucidation and Evolution of the Active Component within Cu/Fe/ZSM - 5 for Catalytic Methane Oxidation: From Synthesis to Catalysis. *ACS Catal.* **2013**, *3*, 689−699.
(185) Baerlocher, C.; McCusker, L. B.; Olson, D. H. *Atlas of Zeolite Framework Types*; Elsevier: Amsterdam, 2007.
(186) Newsam, J. M.; Treacy, M. M.; Koetsier, W. T.; De Gruyter, C. B. Structural Characterization of Zeolite Beta. *Proc. R. Soc. London, Ser. A* **1988**, *420*, 375−405.
(187) Vaughan, P. A. The Crystal Structure of the Zeolite Ferrierite. *Acta Crystallogr.* **1966**, *21*, 983−990.
(188) Kokotailo, G. T.; Lawton, S. L.; Olson, D. H.; Meier, W. M. Structure of Synthetic Zeolite ZSM-5. *Nature* **1978**, *272*, 437−438.
(189) Sklenak, S.; Andrikopoulos, P. C.; Boekfa, B.; Jansang, B.; Nováková, J.; Benco, L.; Bucko, T.; Hafner, J.; Dědeček, J.; Sobalík, Z. {N2O} Decomposition over Fe-Zeolites: Structure of the Active Sites and the Origin of the Distinct Reactivity of Fe-Ferrierite, Fe-ZSM-5, and Fe-Beta. A Combined Periodic {DFT} and Multispectral Study. *J. Catal.* **2010**, *272*, 262−274.
(190) Burns, R. G.; Clark, M. G.; Stone, A. J. Vibronic Polarization in the Electronic Spectra of Gillespite, a Mineral Containing Iron (II) in Square-Planar Coordination. *Inorg. Chem.* **1966**, *5*, 1268−1272.
(191) Cantalupo, S. A.; Fiedler, S. R.; Shores, M. P.; Rheingold, A. L.; Doerrer, L. H. High-Spin Square-Planar CoII and FeII Complexes and Reasons for Their Electronic Structure. *Angew. Chem., Int. Ed.* **2012**, *51*, 1000−1005.
(192) Pinkert, D.; Demeshko, S.; Schax, F.; Braun, B.; Meyer, F.; Limberg, C. A Dinuclear Molecular Iron (II) Silicate with Two High-Spin Square-Planar FeO4 Units. *Angew. Chem., Int. Ed.* **2013**, *52*, 5155−5158.
(193) Pascualini, M. E.; Di Russo, N. V.; Thuijs, A. E.; Ozarowski, A.; Stoian, S. A.; Abboud, K. A.; Christou, G.; Veige, A. S. A High-Spin Square-Planar Fe(II) Complex Stabilized by a Trianionic Pincer-Type Ligand and Conclusive Evidence for Retention of Geometry and Spin State in Solution. *Chem. Sci.* **2015**, *6*, 608−612.
(194) Clark, M. G.; Bancroft, G. M.; Stone, A. J. Mössbauer Spectrum of Fe2+ in a Square-Planar Environment. *J. Chem. Phys.* **1967**, *47*, 4250−4261.
(195) Wurzenberger, X.; Piotrowski, H.; Klüfers, P. A Stable Molecular Entity Derived from Rare Iron (II) Minerals: The Square-Planar High-Spin-d6 FeIIO4 Chromophore. *Angew. Chem., Int. Ed.* **2011**, *50*, 4974−4978.
(196) Neidig, M. L.; Decker, A.; Choroba, O. W.; Huang, F.; Kavana, M.; Moran, G. R.; Spencer, J. B.; Solomon, E. I. Spectroscopic and Electronic Structure Studies of Aromatic Electrophilic Attack and Hydrogen-Atom Abstraction by Non-Heme Iron Enzymes. *Proc. Natl. Acad. Sci. U. S. A.* **2006**, *103*, 12966−12973.
(197) Rossi, A. R.; Hoffmann, R. Transition Metal Pentacoordination. *Inorg. Chem.* **1975**, *14*, 365−374.
(198) Srnec, M.; Wong, S. D.; Matthews, M. L.; Krebs, C.; Bollinger, J. M.; Solomon, E. I. Electronic Structure of the Ferryl Intermediate in the α-Ketoglutarate Dependent Non-Heme Iron Halogenase SyrB2: Contributions to H Atom Abstraction Reactivity. *J. Am. Chem. Soc.* **2016**, *138*, 5110.
(199) Srnec, M.; Wong, S. D.; England, J.; Que, L.; Solomon, E. I. π-Frontier Molecular Orbitals in S= 2 Ferryl Species and Elucidation of Their Contributions to Reactivity. *Proc. Natl. Acad. Sci. U. S. A.* **2012**, *109*, 14326−14331.
(200) McDonald, A. R.; Que, L. High-Valent Nonheme Iron-Oxo Complexes: Synthesis, Structure, and Spectroscopy. *Coord. Chem. Rev.* **2013**, *257*, 414−428.
(201) Starokon, E. V.; Parfenov, M. V.; Arzumanov, S. S.; Pirutko, L. V.; Stepanov, A. G.; Panov, G. I. Oxidation of Methane to Methanol on the Surface of FeZSM-5 Zeolite. *J. Catal.* **2013**, *300*, 47−54.
(202) Panov, G. I.; Dubkov, K. A.; Paukshtis, Y. A. Identification of Active Oxygen Species over Fe Complexes in Zeolites. In *Catalysis by Unique Metal Ion Structures in Solid Matrices: From Science to Application*; Centi, G., Wichterlová, B., Bell, A. T., Eds.; Springer Netherlands: Dordrecht, 2001; pp 149−163.
(203) de Visser, S. P.; Oh, K.; Han, A.-R.; Nam, W. Combined Experimental and Theoretical Study on Aromatic Hydroxylation by Mononuclear Nonheme Iron (IV)− Oxo Complexes. *Inorg. Chem.* **2007**, *46*, 4632−4641.
(204) Hammond, C.; Jenkins, R. L.; Dimitratos, N.; Lopez-sanchez, J. A.; Forde, M. M.; Thetford, A.; Murphy, D. M.; Hagen, H.; Stangland, E. E.; Moulijn, J. M.; et al. Catalytic and Mechanistic Insights of the Low-Temperature Selective Oxidation of Methane over Cu-Promoted Fe-ZSM-5. *Chem. - Eur. J.* **2012**, *18*, 15735−15745.
(205) Hammond, C.; Dimitratos, N.; Lopez-Sanchez, J. A.; Jenkins, R. L.; Whiting, G.; Kondrat, S. A.; Hasbi ab Rahim, M.; Forde, M. M.; Thetford, A.; Hagen, H.; et al. Aqueous-Phase Methane Oxidation over Fe-MFI Zeolites; Promotion through Isomorphous Framework Substitution. *ACS Catal.* **2013**, *3*, 1835−1844.
(206) Vanelderen, P.; Hadt, R. G.; Smeets, P. J.; Solomon, E. I.; Schoonheydt, R. A.; Sels, B. F. Cu-ZSM-5: A Biomimetic Inorganic Model for Methane Oxidation. *J. Catal.* **2011**, *284*, 157−164.
(207) Panov, G. I.; Sobolev, V. I.; Dubkov, K. A.; Parmon, V. N.; Ovanesyan, N. S.; Shilov, A. E.; Shteinman, A. A. Iron Complexes in Zeolites as a New Model of Methane Monooxygenase. *React. Kinet. Catal. Lett.* **1997**, *61*, 251−258.
(208) Hanson, R. S.; Hanson, T. E. Methanotrophic Bacteria. *Microbiol. Rev.* **1996**, *60*, 439−471.
(209) Culpepper, M. A.; Cutsail, G. E., III; Gunderson, W. A.; Hoffman, B. M.; Rosenzweig, A. C. Identification of the Valence and Coordination Environment of the Particulate Methane Monooxygenase Copper Centers by Advanced EPR Characterization. *J. Am. Chem. Soc.* **2014**, *136*, 11767−11775.
(210) Lieberman, R. L.; Kondapalli, K. C.; Shrestha, D. B.; Hakemian, A. S.; Smith, S. M.; Telser, J.; Kuzelka, J.; Gupta, R.; Borovik, A. S.; Lippard, S. J.; et al. Characterization of the Particulate Methane Monooxygenase Metal Centers in Multiple Redox States by X-Ray Absorption Spectroscopy. *Inorg. Chem.* **2006**, *45*, 8372−8381.

DOI: 10.1021/acs.chemrev.7b00344
Chem. Rev. 2018, 118, 2718−2768

(211) Culpepper, M. A.; Cutsail, G. E.; Hoffman, B. M.; Rosenzweig, A. C. Evidence for Oxygen Binding at the Active Site of Particulate Methane Monooxygenase. *J. Am. Chem. Soc.* **2012**, *134*, 7640−7643.
(212) Solomon, E. I.; Ginsbach, J. W.; Heppner, D. E.; Kieber-Emmons, M. T.; Kjaergaard, C. H.; Smeets, P. J.; Tian, L.; Woertink, J. S. Copper Dioxygen (Bio)inorganic Chemistry. *Faraday Discuss.* **2011**, *148*, 11−39.
(213) Matoba, Y.; Kumagai, T.; Yamamoto, A.; Yoshitsu, H.; Sugiyama, M. Crystallographic Evidence That the Dinuclear Copper Center of Tyrosinase Is Flexible during Catalysis. *J. Biol. Chem.* **2006**, *281*, 8981−8990.
(214) Eickman, N. C.; Solomon, E. I.; Larrabee, J. A.; Spiro, T. G.; Lerch, K. Ultraviolet Resonance Raman Study of Oxytyrosinase. Comparison with Oxyhemocyanins. *J. Am. Chem. Soc.* **1978**, *100*, 6529−6531.
(215) Henson, M. J.; Mahadevan, V.; Stack, T. D. P.; Solomon, E. I. A New Cu (II) Side-on Peroxo Model Clarifies the Assignment of the Oxyhemocyanin Raman Spectrum. *Inorg. Chem.* **2001**, *40*, 5068−5069.
(216) Matsubara, T.; Frunzke, K.; Zumft, W. G. Modulation by Copper of the Products of Nitrite Respiration in Pseudomonas Perfectomarinus. *J. Bacteriol.* **1982**, *149*, 816−823.
(217) Brown, K.; Djinovic-Carugo, K.; Haltia, T.; Cabrito, I.; Saraste, M.; Moura, J. G.; Moura, I.; Tegoni, M.; Cambillau, C. Revisiting the Catalytic CuZ Cluster of Nitrous Oxide (N2O) Reductase Evidence of a Bridging Inorganic Sulfur. *J. Biol. Chem.* **2000**, *275*, 41133−41136.
(218) Brown, K.; Tegoni, M.; Prudêncio, M.; Pereira, A. S.; Besson, S.; Moura, J. J.; Moura, I.; Cambillau, C. A Novel Type of Catalytic Copper Cluster in Nitrous Oxide Reductase. *Nat. Struct. Biol.* **2000**, *7*, 191−195.
(219) Chen, P.; Cabrito, I.; Moura, J. J. G.; Moura, I.; Solomon, E. I. Spectroscopic and Electronic Structure Studies of the μ4-Sulfide Bridged Tetranuclear CuZ Cluster in N2O Reductase: Molecular Insight into the Catalytic Mechanism. *J. Am. Chem. Soc.* **2002**, *124*, 10497−10507.
(220) Rosenzweig, A. C.; Nordlund, P.; Takahara, P. M.; Frederick, C. A.; Lippard, S. J. Geometry of the Soluble Methane Monooxygenase Catalytic Diiron Center in Two Oxidation States. *Chem. Biol.* **1995**, *2*, 409−418.
(221) Lee, S.-K.; Lipscomb, J. D. Oxygen Activation Catalyzed by Methane Monooxygenase Hydroxylase Component: Proton Delivery during the O− O Bond Cleavage Steps. *Biochemistry* **1999**, *38*, 4423−4432.
(222) Shu, L.; Nesheim, J. C.; Kauffmann, K.; Münck, E.; Lipscomb, J. D.; Que, L. An Fe2IVO2 Diamond Core Structure for the Key Intermediate Q of Methane Monooxygenase. *Science* **1997**, *275*, 515−518.
(223) Banerjee, R.; Proshlyakov, Y.; Lipscomb, J. D.; Proshlyakov, D. A. Structure of the Key Species in the Enzymatic Oxidation of Methane to Methanol. *Nature* **2015**, *518*, 431−434.
(224) Ambundo, E. A.; Friesner, R. A.; Lippard, S. J. Reactions of Methane Monooxygenase Intermediate Q with Derivatized Methanes. *J. Am. Chem. Soc.* **2002**, *124*, 8770−8771.
(225) Baik, M.-H.; Gherman, B. F.; Friesner, R. A.; Lippard, S. J. Hydroxylation of Methane by Non-Heme Diiron Enzymes: Molecular Orbital Analysis of C− H Bond Activation by Reactive Intermediate Q. *J. Am. Chem. Soc.* **2002**, *124*, 14608−14615.
(226) Choroba, O. W.; Williams, D. H.; Spencer, J. B. Biosynthesis of the Vancomycin Group of Antibiotics: Involvement of an Unusual Dioxygenase in the Pathway to (S)-4-Hydroxyphenylglycine. *J. Am. Chem. Soc.* **2000**, *122*, 5389−5390.
(227) Johnson-Winters, K.; Purpero, V. M.; Kavana, M.; Nelson, T.; Moran, G. R. (4-Hydroxyphenyl) Pyruvate Dioxygenase from Streptomyces Avermitilis: The Basis for Ordered Substrate Addition. *Biochemistry* **2003**, *42*, 2072−2080.
(228) Fritze, I. M.; Linden, L.; Freigang, J.; Auerbach, G.; Huber, R.; Steinbacher, S. The Crystal Structures of Zea Mays and Arabidopsis 4-Hydroxyphenylpyruvate Dioxygenase. *Plant Physiol.* **2004**, *134*, 1388−1400.
(229) Koehntop, K. D.; Emerson, J. P.; Que, L. The 2-His-1-Carboxylate Facial Triad: A Versatile Platform for Dioxygen Activation by Mononuclear Non-Heme iron(II) Enzymes. *JBIC, J. Biol. Inorg. Chem.* **2005**, *10*, 87−93.
(230) Neidig, M. L.; Kavana, M.; Moran, G. R.; Solomon, E. I. CD and MCD Studies of the Non-Heme Ferrous Active Site in (4-Hydroxyphenyl) Pyruvate Dioxygenase: Correlation between Oxygen Activation in the Extradiol and α-KG-Dependent Dioxygenases. *J. Am. Chem. Soc.* **2004**, *126*, 4486−4487.
(231) Davies, G.; El-Sayed, M. A. Stoichiometry and Kinetics of the Oxidation of Halo (Pyridine) Copper (I) Complexes by Dioxygen in Aprotic Solvents. Effects of Copper (I) Reactant Molecularity on the Rate Law and Evidence for Ligand-Dependent Product Structures. *Inorg. Chem.* **1983**, *22*, 1257−1266.
(232) Lapinte, C.; Riviere, H.; Roselli, A.; Fabre, C. Role of a Copper Complex in an Oxygen-Atom Transfer Reaction from Dioxygen to Triphenylphosphine. *J. Chem. Soc., Chem. Commun.* **1981**, *21*, 1109−1110.
(233) Karlin, K. D.; Gultneh, Y.; Hayes, J. C.; Zubieta, J. Copper (I)-Dioxygen Reactivity. II: Reaction of a Three-Coordinate Copper (I) Complex with O2, with Evidence for a Binuclear Oxo-Copper (II) Species: Structural Characterization of a Parallel-Planar Dihydroxo-Bridged Dimer. *Inorg. Chem.* **1984**, *23*, 519−521.
(234) Kitajima, N.; Koda, T.; Hashimoto, S.; Kitagawa, T.; Morooka, Y. Synthesis and Characterization of the Dinuclear copper(II) Complexes [Cu(HB(3,5-Me2pz)3)]2X (X = O2-, (OH)22-, CO22-, O22-). *J. Am. Chem. Soc.* **1991**, *113*, 5664−5671.
(235) Haack, P.; Kärgel, A.; Greco, C.; Dokic, J.; Braun, B.; Pfaff, F. F.; Mebs, S.; Ray, K.; Limberg, C. Access to a CuII−O−CuII Motif: Spectroscopic Properties, Solution Structure, and Reactivity. *J. Am. Chem. Soc.* **2013**, *135*, 16148−16160.
(236) Csicsery, S. M. Shape-Selective Catalysis in Zeolites. *Zeolites* **1984**, *4*, 202−213.
(237) Kroll, T.; Hadt, R. G.; Wilson, S. A.; Lundberg, M.; Yan, J. J.; Weng, T.-C.; Sokaras, D.; Alonso-Mori, R.; Casa, D.; Upton, M. H.; et al. Resonant Inelastic X-Ray Scattering on Ferrous and Ferric Bis-Imidazole Porphyrin and Cytochrome c: Nature and Role of the Axial Methionine−Fe Bond. *J. Am. Chem. Soc.* **2014**, *136*, 18087−18099.
(238) Yoon, J.; Fujii, S.; Solomon, E. I. Geometric and Electronic Structure Differences between the Type 3 Copper Sites of the Multicopper Oxidases and Hemocyanin/tyrosinase. *Proc. Natl. Acad. Sci. U. S. A.* **2009**, *106*, 6585−6590.
(239) Traa, Y.; Burger, B.; Weitkamp, J. Zeolite-Based Materials for the Selective Catalytic Reduction of NOx with Hydrocarbons. *Microporous Mesoporous Mater.* **1999**, *30*, 3−41.
(240) Sutherlin, K. D.; Liu, L. V.; Lee, Y.-M.; Kwak, Y.; Yoda, Y.; Saito, M.; Kurokuzu, M.; Kobayashi, Y.; Seto, M.; Que, L.; et al. Nuclear Resonance Vibrational Spectroscopic Definition of Peroxy Intermediates in Nonheme Iron Sites. *J. Am. Chem. Soc.* **2016**, *138*, 14294−14302.

DOI: 10.1021/acs.chemrev.7b00344
Chem. Rev. 2018, 118, 2718−2768